FREE STANDING PHOTONIC CRYSTAL CAVITIES FOR DIAMOND COLOR CENTERS

A Dissertation

by

ABDULRAHMAN MOHAMMED S ALAJLAN

Submitted to the Office of Graduate and Professional Studies of
Texas A&M University
in partial fulfillment of the requirements for the degree of

DOCTOR OF PHILOSOPHY

Chair of Committee,	Alexey Akimov
Committee Members,	M. Suhail Zubairy
	Alexei Sokolov
	Philip Hemmer
Head of Department,	Grigory Rogachev

December 2019

Major Subject: Physics

Copyright 2019 Abdulrahman Alajlan

ABSTRACT

The sub-wavelength optical confinement of low optical loss photonics intensely increases the probability of light-matter interaction up to a single quantum level. The chip based photonics provide a scalable platform from which to study many effects that are crucial in many applications ranging from chemical sensing and nonlinear optics, to quantum information processing and cavity optomechanics.

This work addresses the use of photonic devices in quantum optics, including device design, fabrication and characterization, and optical coupling. We present a scalable "semicircular holes" design for 1D photonic crystal cavities that combines an ultrahigh Q/V value and high transmission. In high refractive index materials such as gallium phosphide (GaP), our design ideally possesses $Q/V > 10^7$ and transmission over 90%. We also address the fabrication of GaP-based photonic devices using different methods despite the challenges due to mainly the lack of the necessary tools and equipment. Besides the design and fabrication, we propose a new scheme for coupling photons strongly to a single photon emitter, namely germanium vacancy (GeV) center in diamond, based on cavity QED. Our analysis reveals a strong coupling regime can be achieved for the first time using a solid-state single photon emitter.

Next, we shift to silicon nitride (Si_3N_4) material that is cheap and easy to grow, fabricate, and measure. We again design silicon nitride nanobeam cavities based on the quadratic tapering method with and without semicircular holes. The designed devices feature large optical quality factors, in excess of 10^5. We also study cavity QED for a single GeV center that is strongly coupled to the cavity field. The fabrication of Si_3N_4 nanobeam cavities is discussed together with the optimization needed mostly for electron-beam lithography (EBL) process. We demonstrate engineered nanobeam cavities for Si_3N_4 grown by plasma-enhanced chemical vapor deposition (PECVD) films as well as low pressure chemical vapor deposition (LPCVD) films. The devices grown by the latter method possess relatively large optical quality factors, approaches 10^4, around the zero-phonon line (ZPL) of GeV center.

Lastly, we present a method for fiber-waveguide coupling that allows efficient power transfer from an optical fiber into a waveguide and vice versa. We study the design and fabrication method in details for both structures, and optimize the coupling using finite difference time domain (FDTD). Our method uses conical tapered optical fibers (with a tapering angle of $\sim 4^{\circ}$) that are coupled over ~ 11 μm to a Si_3N_4 waveguide taper (with a tapering angle of $\sim 1^{\circ}$). We demonstrate using a deterministic approach single-mode fiber-waveguide coupling efficiency as high as 96%.

ACKNOWLEDGMENTS

Over the course of my years at Texas A&M University, I have received enormous help and assistance from a number of people who made my journey to pursue my doctoral degree possible. I would like first to thank my PhD advisor, Prof. Alexey Akimov for the great time I spent in his group. Alexey's enthusiasm and patience has never ceased to be inspiring and encouraging. I feel really fortunate to have learned so much about all aspects of research from him. I would like also to thank and acknowledge the other members of my committee, Prof. M. Suhail Zubairy, Prof. Alexei Sokolov, and Prof. Philip Hemmer for their guidance, advice, and time throughout my graduate program.

I have spent a great time with the talented researchers in the Akimov's group, all of whom I consider friends and colleagues. Ivan Cojocaru was really helpful in sharing his great ideas and solving problems I have encountered in various aspects of my research. Xiaohan Liu has contributed greatly to my research, especially to the work related to fiber optics. My thanks extends to the new members of the group Mohit Khurana and Sina Kordmahale for their help and suggestions.

I was fortunate to collaborate with researchers from Hemmer's group. I have learned a lot from Fahad Alghannam who never ceased to advice and train me on basics of experimental optics. Also, I thank his colleague Masfer Alkahtani who was has helped me in various aspects. My gratitude extends to researchers in Zheltikov's group and Sokolov's group who collaborated with us and helped to build optical setups.

I would also like to thank staff and researchers in Aggiefab facility who helped me to handle tools and equipment in their facility. I also acknowledge Brazos Cluster for allowing us to run simulations in their computer cluster and installing the needed software. I would like to extend my gratitude to Denis Sukachev from Lukin's group at Harvard, who guided me through many issues and challenges I have encountered.

In addition to local institutions, I would like extend my deepest gratitude to King Abdulaziz city for science & technology (KACST) and The Saudi Arabian Cultural Mission (SACM) who

sponsored my higher education and was generous to me and my family with everything we needed. I am very appreciative of Mohammad Al-Amri and his initiative in establishing quantum optics group in KACST.

Finally, my school and life beyond have also been supported through the friendships of many wonderful people. I would especially like to thank my family for support and compassion. My mother has been a life-long role model to whom I have learned the wisdom and patience. Also, My father has a big impact on my life in all aspects and I am always motivated by his words characters. I would like to extend my thanks to my wife who has always been encouraging and supporting from the beginning of my academic life. I would like to express my gratitude to my siblings have shown the true brotherhood and provided various assistance to achieve this milestone.

CONTRIBUTORS AND FUNDING SOURCES

Contributors

This work was supervised by a dissertation committee consisting of Prof. Alexey Akimov (advisor), Prof. M. Suhail Zubairy and Prof. Alexei Sokolov of the Department of Physics & Astronomy, and Professor Philip Hemmer of Department of Electrical & Computer Engineering.

The experiment reported in Chapter 4 was conducted by the student in consultation with Denis Sukachev of the Department of Physics at Harvard University.

All other work for the dissertation was completed independently by the student.

Funding Sources

Graduate study was supported by a scholarship from King Abdulaziz City for Science and Technology and a dissertation research fellowship from National Science Foundation (NSF) (PHY-1820930).

NOMENCLATURE

QED	Quantum electrodynamics
FDTD	finite difference time domain
FCC	Face-centered cubic
NV	Nitrogen-vacancy
SiV	Silicon-vacancy
GeV	Germanium-vacancy
ZPL	Zero-phonon line
VCSEL	Vertical cavity surface emitting lasers
TIR	Total internal reflection
FDTD	Finite Difference Time Domain
TE	Transverse-electric
TM	Transverse-magnetic
HF	hydrofluoric acid
PL	Photoluminescence
GaP	Gallium Phosphide
DNC	Diamond nanocrystal
AFM	Atomic force microscope
EBL	Electron beam lithography
ICP-RIE	Inductively coupled plasma reactive ion etching
CMOS	Complementary metal oxide semiconductor
PECVD	Plasma-enhanced chemical vapor deposition
LPCVD	Low pressure chemical vapor deposition

TABLE OF CONTENTS

Page

ABSTRACT ii

ACKNOWLEDGMENTS iv

CONTRIBUTORS AND FUNDING SOURCES vi

NOMENCLATURE vii

TABLE OF CONTENTS viii

LIST OF FIGURES x

LIST OF TABLES xvii

1. INTRODUCTION 1

   1.1 Color centers in diamond 1
   1.2 Photonic crystal cavities 3

2. GALLIUM PHOSPHIDE NANOBEAM CAVITIES 9

   2.1 Introduction 9
   2.2 Cavity mirror strength 13
   2.3 Geometric optimizations 18
   2.4 Cavity QED analysis with GeV center 22
   2.5 Fabrication of GaP nanobeam cavities 26
   2.6 Conclusion 34

3. SILICON NITRIDE NANOBEAM CAVITIES 36

   3.1 Introduction 36
   3.2 Design of Si_3N_4 nanobeam cavities 38
   3.3 Cavity QED analysis 41
   3.4 Fabrication of Si_3N_4 nanobeam cavities 44
   3.5 Characterization and quality factor measurement 48
   3.6 Conclusion 53

4. EFFICIENT FIBER-WAVEGUIDE COUPLING 54

   4.1 Introduction 54
   4.2 Adiabatic mode transfer 57

4.3 Design and fabrication of waveguide tapers 60
4.4 Design and fabrication of optical fiber tips 62
4.5 Characterization and optimization........ 65
4.6 Conclusion........ 71

5. SUMMARY 72

REFERENCES 74

APPENDIX A. MEEP SOFTWARE FOR FDTD SIMULATIONS 82

A.1 Photonic band structure 82
A.2 Cavities resonant modes 87

APPENDIX B. OPTIMIZATION OF ELECTRON BEAM LITHOGRAPHY 97

APPENDIX C. REFLECTION OF THE FIBER RETROREFLECTOR 101

LIST OF FIGURES

FIGURE Page

1.1 (a) The diamond lattice consists of a pair of intersecting face-centered cubic lattices, with each separated by 1/4 of the width of the unit cell in each dimension. This picture is reprinted from ref. [1]. (b) Fluorescence from different structural defects in diamond reprinted from ref. [2]. 1

1.2 (a) Molecular structure of the GeV center. The Germanium atom is located between two empty lattice sites to make inversion symmetry. (b) PL spectrum of the GeV center reveals four optical transitions. (inset) Electronic structure and optical transitions. Figure (a) & (b) are reprinted from ref. [16]. 3

1.3 Band diagram of a free standing 1D photonic crystal slab reprinted from ref. [20]. (inset) photonic crystal slab has periodic holes along the dimension x and finite thickness (0.4 a) and width (1 a). The lateral axis represents the value of the reciprocal space, and the vertical axis represents normalized frequencies. The discrete frequencies below the light line were obtained by solving the dispersion equation numerically. 5

1.4 sketch of a nanobeam cavity created by removing one hole breaking the symmetry of the x-direction. The corresponding H_z field pattern of a localized cavity resonance taken at z = 0 plane. The localization of H_z field is slowly decaying to the waveguide representing in-plane loss. The out-of plane loss also exists as a result of coupling to the radiation modes discussed in the text. 6

2.1 Schematic of a typical nanobeam cavity. Q_w and Q_r refer to the decay mechanism of the cavity resonance due to coupling to the waveguide mode and radiation mode, respectively. 11

2.2 (a) Sketch of tapered nanobeam cavity with semicircular holes added to each side of the hole segment. (b) $E_y$field distribution of the fundamental TE mode in the middle (z = 0) plane of the nanobeam cavity. (c) E_y field distribution for the TE fundamental mode obtained from FDTD simulations (blue dots) and from an analytic formula (red line): $E_y = \cos\left((x - x_0)\frac{\pi}{a}\right)\exp\left(-\sigma^2(x - x_0)\right)$. Figures (a)-(c) are reprinted with permission from ref. [28]. 12

2.3 (a) Mirror strength of each hole segment for linear (red) and quadratic (blue) tapering profile. (b) Mirror strength of each hole segment for a nanobeam with only central holes (blue) and with additional semicircular holes (yellow). Both figures were obtained from the analytic expression Eq. (2.11) derived from the plane wave expansion method. 14

2.4 Mirror strength obtained from FDTD simulations. (a) Mirror strength as a function of nanobeam final width for three configurations: only central holes (green), central holes with in-phase semicircular holes (orange), central holes with out-of-phase semicircular holes (blue). (b) Mirror strength as a function of the hole segment number after quadratic tapering for only central holes (green) and out-of-phase semicircular holes (blue). The dashed line is a linear fit with $R^2 = 0.98$. (c) & (d) Mirror strength as a function of hole radius for two nanobeam designs with (blue) and without (orange) semicircular holes suggested by Qimin et al. [33] and Notomi et al. [34], respectively. Figures (a)-(d) are reprinted with permission from ref. [28]. 15

2.5 (a) & (b) TE band structure for nanobeam cavity with additional semicircular holes and with only central holes, respectively. The dashed line marks the cavity resonant frequency which is found to be 1% less than the dielectric band-edge of the first hole. The bandgap includes all modes between dielectric band-edge and extend to the air band-edge of the last hole (i.e., between the two red lines). All geometries are assumed to be GaP slab suspended in air (n =3.36) and the thickness is the same as the spacing between holes. Figure (a) & (b) are reprinted with permission from ref. [28]. 17

2.6 (a) & (b) transmission dependence on Q/V ratio for different nanobeam final widths in semicircular holes and central holes design, respectively. (c) & (d) number of holes dependence on Q/V ratio for different final widths in semicircular holes and central holes design, respectively. The initial width is consistent (W_i/a = 1.5) for the plots. Figure (a) & (c) are reprinted with permission from ref. [28]....... 19

2.7 (a) The dependence of Q/V value taken at 90% cavity transmission on the nanobeam initial width. The difference between the final and initial width is fixed, $\Delta W/a = 0.3$. (b) The number of holes dependence on Q/V calculated for $W_{\text{i}}/a = 1.5$ in both geometries. (inset) Reduction factor in number of holes as a function of Q/V value gained by adding semicircular holes. (c) & (d) The number of holes dependence on Q/V calculated for different nanobeam initial widths. Figure (a) & (b) are reprinted with permission from ref. [28]. 20

2.8 Cavity Q/V and transmission dependence on the nanobeam thickness. We consider the following nanobeam widths: $W_{\text{i}}/a = 1.5$ and $W_{\text{f}}/a = 1.8$, based on our width optimizations discussed previously. Figure (a) is reprinted with permission from ref. [28]. 21

2.9 (a) Sketch of DNC placed on top of a nanobeam cavity. (b) E_y cross sections of the TE fundamental mode. α^2 is the ratio of the energy density in the GaP nanobeam cavity to the maximum energy density at the DNC calculated for different nanobeam thicknesses. Figure (a) & (b) are reprinted with permission from ref. [28]. 23

2.10 (a) Relevant cavity QED rates as a function of number of holes. $\kappa/2\pi$ is the cavity decay rate, $\gamma_{sp}/2\pi$ is the atomic decay rate of the GeV center, and $g/2\pi$ is the single photon coupling rate. (b) Cooperativity (dots) and weak/strong coupling index (open circles) as a function of number of holes. Figure (a) & (b) are reprinted with permission from ref. [28]. 24

2.11 (a) Cooperativity (dots) and weak/strong coupling index (open circles) as a function of nanobeam thickness. We considered cavities with 14 number of holes ($Q/V \approx 10^6$) for all thicknesses to maintain the cavity transmission. (d) cooperativity as a function of number of holes for different DNC sizes. Figure (b) is reprinted with permission from ref. [28]. 25

2.12 (a) Schematic of the layers grown in the GaP substrate. (b) Atomic force microscope scan for 10×10 μm^2 area of the top GaP membrane. The corresponding root mean square is 2.3 nm. (c) Atomic force microscope scan for 10×10 μm^2 area between the rough points. The corresponding root mean square is 0.2 nm. 28

2.13 Fabrication steps of the GaP nanobeam cavity using HSQ negative resist. 29

2.14 (a) The corrosion of the intermediate layer $Al_{0.91}GaP_{0.09}$ after a Cl_2 based dry etch. (b) Suspended GaP membranes one week following the undercutting procedure. 31

2.15 Fabrication steps of the GaP nanobeam cavity using PMMA positive resist. 32

2.16 (a) SEM image of Si_3N_4 hard mask after CHF_4 dry etch. (b) SEM image of suspended GaP membranes following the undercutting procedure. 34

3.1 (a) Sketch of Si_3N_4 nanobeam cavity for the central holes design (top) and for semicircular holes (bottom). (b) & (c) The corresponding TE band structure calculated by FDTD simulations. The dashed line marks the resonant frequency. The thickness for the central holes design is d/a = 0.9, and for semicircular holes is d/a = 0.85. 38

3.2 (a) Transmission dependence on Q/V value for the central holes design and the semicircular holes design. The initial width is W_i/a = 1.5, and the final width is W_f/a = 2. (b) Number of holes dependence on Q/V value for both designs. (inset) Reduction factor in number of holes as a function of Q/V value gained by adding the semicircular holes. 39

3.3 (a) Mirror strength as a function of nanobeam final width for two configurations: only central holes (orange) and out-of-phase semicircular holes (blue). (b) E_{y} field distribution for the TE fundamental mode of the central hole design obtained from FDTD simulations (blue dots) and from an analytic formula (red line): $E_{\mathrm{y}} = \cos\left((x - x_0)\frac{\pi}{a}\right)\exp\left(-\sigma^2(x - x_0)\right)$. . . . 40

3.4 (a) Relevant cavity QED rates as a function of number of holes for Si_3N_4 nanobeam cavities. $\kappa/2\pi$ is the cavity decay rate, $\gamma_{\mathrm{sp}}/2\pi$ is the atomic decay rate of the GeV center, and $g/2\pi$ is the single photon coupling rate. (b) Cooperativity (dots) and weak/strong coupling index (open circles) as a function of number of holes. Results shown in (a) and (b) are related to the semicircular holes design. . . . 41

3.5 (a) & (b) Cooperativity as a function of number of holes and cavity Q/V value for different DNC sizes placed on top of Si_3N_4 nanobeam cavity, respectively. . . . 42

3.6 Fabrication steps of Si_3N_4 nanobeam cavities. . . . 43

3.7 (a) & (b) SEM image of two different designs explained in the text of Si_3N_4 nanobeam cavities after the dry etch. (c) & (d) SEM image of the same devices after the undercutting procedure of the underlying Si layer. (e) & (f) high resolution SEM images of the same devices taken at a 35° stage tilt. . . . 45

3.8 (a) & (b) High resolution SEM images of the device fabricated from CSAR 62 resist and 950 PMMA A4 resist, respectively. (c) & (d) Hole profiles extracted with a Gaussian filter to measure the hole roughness for CSAR 62 resist and 950 PMMA A4 resist, respectively. The corresponding standard deviation is σ = 22 nm and σ = 14 nm. The dark spots appear in (a) refer to CSAR 62 resist residues left after the dry etching process and cannot be removed by a resist remover or O_2 plasma ashing. . . . 47

3.9 (a) Schematic of the optical characterization of Si_3N_4 nanobeam cavities. DC and BS are the abbreviation of dichroic mirror (which is used as a band pass filter) and beam splitter, respectively. (b) SEM images of the typical device with a zoomed image of the nanobeam cavity with the central holes design. (c) Normalized reflection spectrum of the cavity TE modes centered at wavelength λ = 630 nm. The Lorentzian fit yields a total quality factor of $Q_{\mathrm{total}} \sim 9{,}300$. . . . 49

3.10 (a) SEM images of the typical device with a zoomed image of the nanobeam cavity with the semicircular holes design. The cavity includes 10 holes in the nanobeam taper, and 6 additional holes in the waveguide region. (b) Normalized reflection spectrum of the cavity TE modes centered at wavelength λ = 630 nm.v The Lorentzian fits yields a total quality factor of $Q_{\mathrm{total}} \sim 5{,}100$. . . . 51

3.11 (a) Cavity resonance taken at different input polarizations. The cavity was fabricated from a PECVD nitride film. (b) Comparison between the cavity quality factor obtained from the experimental measurement and numerical calculation as a function of number of holes. . . . 52

3.12 (a) AFM scan of the top PECVD Si_3N_4 membrane. The corresponding root mean square is 2 nm. (b) SEM image of the cavity fabricated from PECVD film. (c) Normalized reflection spectrum of the cavity TE modes centered at wavelength λ = 630 nm. The Lorentzian fits yields a total quality factor of $Q_{total} \sim$ 2,000. . . . 52

4.1 Typical dimension of optical single-mode fibre core and photonic waveguide for high-index material (GaP) and low-index material (Si_3N_4) operating at the visible regime. . . . 54

4.2 (a) Schematic representation of fiber-to-chip light coupling through grating couplers reprinted from ref. [83]. (b) Schematic representation of edge coupling the fiber to Si waveguide using lensed fibers reprinted from ref. [92]. (c) SEM image of conical tapered fiber tip coupled to Si_3N_4 waveguide taper reprinted from ref. [91]. 56

4.3 (a) Schematic diagram of a tapered slab semiconductor waveguide. Adiabatic mode transformation can be achieved only for a small taper angle, as explained in the text. (b) Harmonic mode frequencies of Si_3N_4 slab from Fig.4.1 for TE polarization. Blue lines correspond to modes that are localized in the slab. The red line is the light line $\omega = ck$. The black line marks the frequency we are interested in or the cavity resonance. . . . 58

4.4 (a) Schematic of fiber-waveguide taper adiabatic coupling. The waveguide has a rectangular hole designed to decrease the effective index of the supermode slowly to ensure the adiabatic mode transformation. (b) Effective index n_{eff} of the waveguide mode (blue), fiber mode (orange), and supermode of the combined structure (green). The opening angle of the fiber (waveguide) is of 3.5° (2.2°). (c) - (e) Cross sections of $|E|^2$ obtained from the FDTD simulation at different normal planes of the combined structure. . . . 59

4.5 (a) SEM images of the Si_3N_4 nanophotonic device which combines a nanobeam cavity and a feeding waveguide tapered at one end, offering efficient coupling to the optical fiber. (b) & (c) SEM image of the waveguide taper supported by the horizontal rods. . . . 61

4.6 (a) Schematic of illustration of the chemical wet etching approach for fabricating tapered fiber tips reprinted from ref. [97]. (b) Schematic of illustration of the heating and pulling approach for fabricating tapered nanofibers reprinted from ref. [98]. . . . 62

4.7 (a) Schematic of fabrication of conical fiber tapers. (b), (d) and (C) SEM images of the final tapered fiber for different speeds resulting in different angles: 2°, 3°, and 4°, respectively. 64

4.8 SEM images of optical fiber tips fabricated with non-optimized parameters. (a) A small portion of silica remaining at the end of the fiber tip attributed to insufficient acid etching. (b) Asymmetrical conical fiber tip as a result of inaccurate adjustment of the fiber direction. The fiber should be oriented perpendicular to the surface during the etching process. (c) & (d) Far-field mode profile of a rough and smooth fiber tip, respectively. 66

4.9 (a) Schematic of the coupling efficiency characterization setup. Fibers are connected by splicing two optical fibers end-to-end using fusion splicer tool (FITEL S179). We routinely achieve less than 0.2dB loss. (b) Normalized reflection spectrum of the cavity TE modes centered at wavelength λ = 630 nm. (c) Optical micrograph of a waveguide coupled to an optical fiber obtained from CCD camera. . 67

4.10 (a) Optical micrograph of an optical fiber coupled to a waveguide taper that is not appropriately rotated to the same angle of the optical fiber. (b) Optical micrograph of an optical fiber coupled to the chip behind the waveguide taper indicated by the huge scattering at the end of the taper. 69

4.11 (a) & (b) The coupling efficiency of TE-polarized waveguide mode to the optical-fiber HE11 mode as a function of fiber-waveguide overlap and waveguide width, respectively, obtained from FDTD simulations. 70

A.1 Left: Band diagram of a uniform one-dimensional medium. Right: Band diagram of a multilayer film that is periodic in one direction (inset). The gap arises at the edge of the Brillouin zone due to the difference in field energy location between the first and second band. Both figures are reprinted from [20]. 83

B.1 SEM images of a nanobeam cavities fabricated via EBL process with various optimization parameters. (a) & (b) Structures fabricated on different rotational angles. These devices were initially fabricated with notches for free space-waveguide coupling instead of the waveguide taper. (c) Imperfect circular holes and rough sidewalls are observed as a result of combining big and small features. (d) Relatively big structures are marked around the device to keep the size of the exposed areas relatively close. These structures will be eradicated during the undercutting procedure. 98

B.2 (a) & (b) SEM images of a nanobeam cavity fabricated on tungsten hard mask before transferred to Si_3N_4 layer. (c) & (d) SEM images of a nanobeam cavity fabricated on Si_3N_4 layer without a tungsten hard mask. Left images are taken after the dry etching process, and right images are taken after the undercutting process. 100

C.1 (a) Schematic of the setup used to measure the reflection of the fiber retroreflector. (b) Schematic of the setup used to measure the power transmission between the point PM1 to the point PM2. 101

LIST OF TABLES

TABLE Page

2.1 HSQ thickness for different spin coating speeds. 27

2.2 Dry etching recipe for GaP. 30

2.3 Dry etching recipe for Si_3N_4 hard mask. 34

3.1 Optical constants of Si_3N_4 and alternative materials. For more details, see ref. [59]. . 37

B.1 Dry etching recipe of tungsten hard mask. 99

1. INTRODUCTION

Quantum information processing is a thriving field in quantum optics that requires manipulating light at a single photon level. One of the most powerful approaches to achieve such light control is by coupling spin qubits to solid-state cavity QED systems. During the past few years, we have studied properties of color centers in diamond together with photonic crystal cavities to build a reliable quantum network. Now, we give a brief introduction about the each element.

1.1 Color centers in diamond

Diamond consists of allotrope of carbon constructed by sp^3 hybridized covalent bonds in the form of a tetrahedral geometry. It has two face-centered cubic (fcc) lattice structures, as plotted Fig. 1.1 (a). These covalent bonds make diamond one of the strongest and robust materials. Although diamond is a well known thermal conductor, it is also a great electronic insulator with a band gap of 5.5eV which gives rise to its optical transparency in the visible regime.

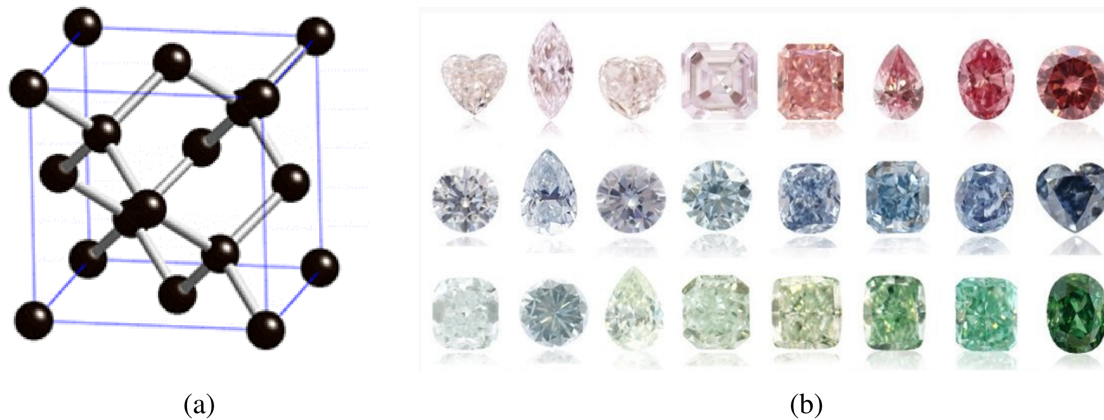

(a) (b)

Figure 1.1: (a) The diamond lattice consists of a pair of intersecting face-centered cubic lattices, with each separated by 1/4 of the width of the unit cell in each dimension. This picture is reprinted from ref. [1]. (b) Fluorescence from different structural defects in diamond reprinted from ref. [2].

Color centers in diamond occur when a defect occurs in the unit cell in which a carbon atom is

replaced by a different element and vacancies. These defects give rise to different visible colors, many of which are also fluorescent, see Fig. 1.1b. Though color centers can occur naturally in diamond, ion implantation and subsequent annealing is the standard method to produce diamond color centers[3]. Stability in room-temperature is one key property of these systems as it leads to fast research and development cycles used to enhance the material. The most widely studied defect in diamond is the negatively charged nitrogen-vacancy NV. A wide range of applications have been achieved using NV center, including quantum information [4–6], magnetic field sensing [7, 8], and thermometry [9]. However, the optical properties of the NV centre are not ideal for quantum information processing since only a small fraction of the emitted photons can be used as qubits due to its strong phonon sideband. Moreover, NV centre is very sensitive to surface defects and damages created by the fabrication process.

On the other hand, silicon-vacancy SiV centers have been emerging during the last decade as alternative color centers which exhibit a very narrow emission bandwidth at room temperature (>70% in the ZPL) due to a weak electron-phonon coupling [10]. Moreover, SiV center has an inversion symmetry of D_{3d} class, making it more stable and resistant to the fluctuations in the local environment[11]. These properties make the SiV center a promising single-photon source for applications such as quantum communications and quantum information processing[12, 13], bioimaging of living organisms [14]. However, the photon emission rate is very low compared to NV centre as a result of the low quantum efficiency (> 10% in bulk diamonds [15]).

On the other hand, negatively charged germanium-vacancy (GeV) centers have recently drawn a considerable attention. The germanium atom in the GeV center is not located on the carbon lattice site but between two vacancies along the <111> lattice direction resulting in an inversion symmetry of D_{3d} class similar to SiV centers, as shown in Fig. 1.2 (a).

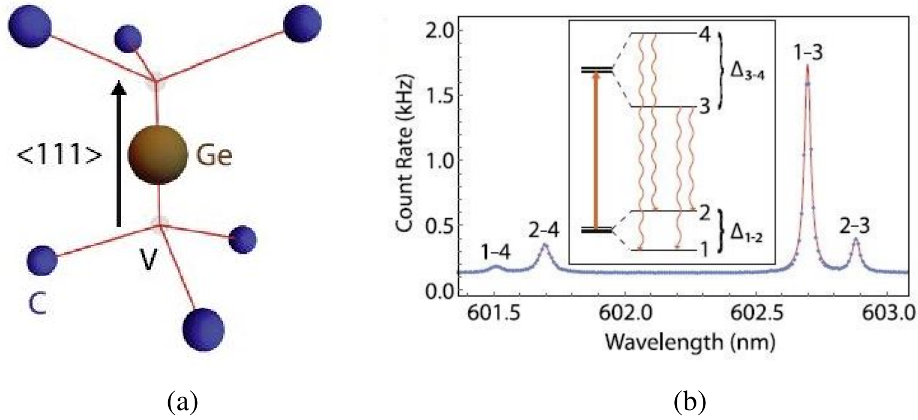

(a) (b)

Figure 1.2: (a) Molecular structure of the GeV center. The Germanium atom is located between two empty lattice sites to make inversion symmetry. (b) PL spectrum of the GeV center reveals four optical transitions. (inset) Electronic structure and optical transitions. Figure (a) & (b) are reprinted from ref. [16].

The symmetry and optical properties of GeV center has been found similar to SiV center with a nearly unitary quantum efficiency, making it a promising single-photon source for quantum applications. In Chapter 2 and Chapter 3, we develop a scheme where a single GeV center is incorporated in nanodiamonds and placed on top of photonic crystal cavities to enhance the light-matter interaction.

1.2 Photonic crystal cavities

Photonic crystals are one of the most promising platform for optical communications due to their compactness which enables scientists and engineers to integrate many components into one chip device. In solid-state physics, semiconductors have periodic electronic potentials which give rise to what is known as the electronic bandgap, a region in which no electron states can exist. The optical analogue is the photonic crystals, in which the atoms are replaced by low-loss dielectric media and the periodic potential is replaced by a periodic refractive index. The periodicity of the refractive index gives rise to a photonic bandgap, preventing photons from propagating in certain energy bands (i.e., a certain range of wavelengths).

Different classes of photonic crystals can be defined based on the dimensionality of such pe-

riodicity. For example, one-dimensional photonic crystals, known as distributed Bragg reflectors (DBR), have been used extensively as mirrors in a vertical cavity surface emitting lasers (VCSELs) [17]. 3D-periodic structures have been suggested simultaneously by Yablonovitch [18] and John [19] in 1987, exactly one century after Rayleigh discovered 1D band gaps. Even though 3D photonic crystals can result in a complete photonic bandgap and can precisely control the light propagation in all directions, the actual fabrication of such structure remain challenging, especially for visible wavelength.

Photonic crystal slabs have received a significant attention recently due to their compactness and feasibility. The slab consists of a thin semiconductor layer that has periodic symmetry along the horizontal dimensions and continuous symmetry along the vertical dimensions, See Fig. 1.3. In photonic crystal slabs, total internal reflection (TIR) controls the light confinement in the vertical direction as a result of the high index contrast between the slab and the surrounding medium, and the confinement of the horizontal direction is controlled by the associated photonic bandgap. This feasibility comes at a price of incomplete band gap that appears in the dispersion relation which we shall explain.

The dispersion diagrams ω(k) contain the most of the optical properties of photonic crystals slabs by giving the frequencies of the Bloch modes as a function of the conserved wavevector along the slab, which is k_x in Fig. 1.3. The modes in dispersion relation are simply the eigenvalues of so-called master equation:

$$\nabla \times \left(\frac{1}{\epsilon(\boldsymbol{r})} \nabla \times \boldsymbol{H}(\boldsymbol{r}) \right) = \left(\frac{\omega}{c} \right)^2 \boldsymbol{H}(\boldsymbol{r}) \tag{1.1}$$

where $\boldsymbol{H}(\boldsymbol{r})$ is the macroscopic magnetic field and $\epsilon(\boldsymbol{r})$ is the relative permittivity. Considering a plain wave (i.e., $\boldsymbol{H}(\boldsymbol{r}) = \boldsymbol{A}e^{i\boldsymbol{k}\cdot\boldsymbol{r}}$) in Eq. (1.1), one can find the eigenvalues of the master equation which represent the dispersion relation:

$$\omega = c\frac{|\boldsymbol{k}|}{\sqrt{\epsilon}} \tag{1.2}$$

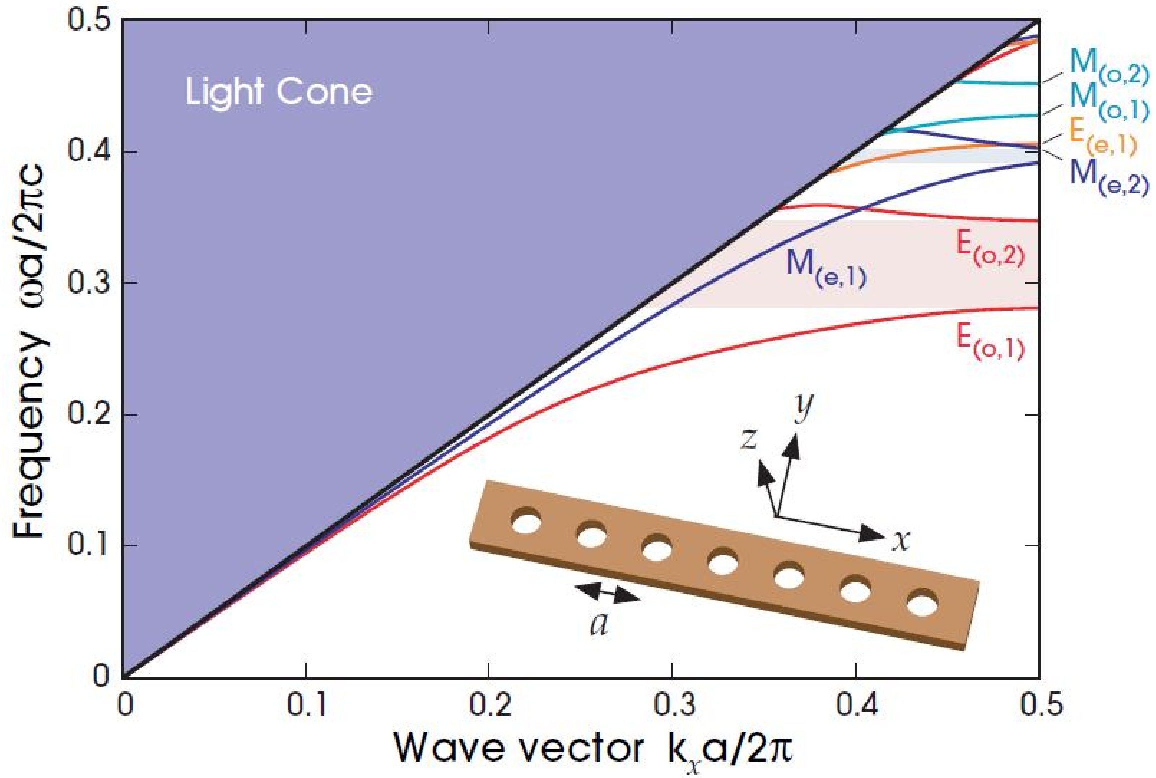

Figure 1.3: Band diagram of a free standing 1D photonic crystal slab reprinted from ref. [20]. (inset) photonic crystal slab has periodic holes along the dimension x and finite thickness (0.4 a) and width (1 a). The lateral axis represents the value of the reciprocal space, and the vertical axis represents normalized frequencies. The discrete frequencies below the light line were obtained by solving the dispersion equation numerically.

Figure 1.3 shows the dispersion diagram for even and odd modes, with respect to mirror symmetry plane $z = 0$, of 1D photonic crystal slabs using 3D Finite Difference Time Domain (FDTD) method. The even modes are referred as transverse-electric (TE) modes which have the dominant E_x, E_y, and H_z components. In contrast, the odd modes are referred as transverse-magnetic (TM) modes which have dominant H_x, H_y, and E_z components. In Fig. 1.3, it is clear that photonic crystal slabs are favorable for TE-like modes as the size of the TE bandgap size is much larger than size of TM bandgap, as apposed to photonic crystal rods which favor TM-like modes [21].

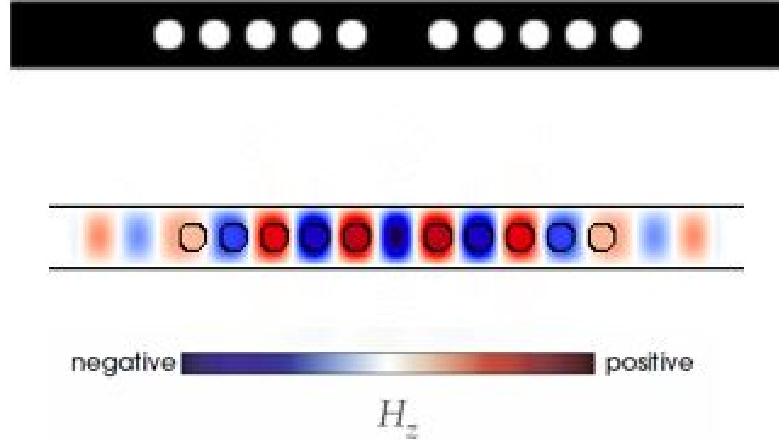

Figure 1.4: sketch of a nanobeam cavity created by removing one hole breaking the symmetry of the x-direction. The corresponding H_z field pattern of a localized cavity resonance taken at z = 0 plane. The localization of H_z field is slowly decaying to the waveguide representing in-plane loss. The out-of plane loss also exists as a result of coupling to the radiation modes discussed in the text.

In the slab shown in Fig. 1.3, the slab is neither infinite nor periodic in the z-direction, and so incident light to the interface between the semiconductor slab and air can escape and couple to continuum radiation modes if angles smaller than the critical angle. That lead to what is called intrinsic radiative loss; the main disadvantage of incomplete bandgaps exist in 1D photonic crystal slabs. The complete bandgaps can be obtain only in 3D photonic crystals [22]. We use the concept of the light line, indicated by the solid black line in Fig. 1.3, to consider these losses in the analysis of slabs. The region above the light line (called light-cone) corresponds to the continuum radiation modes which are not confined by TIR. The modes below the light line can be guided in the slab and are called index guided modes. The photonic bandgap, highlight in Fig. 1.3, is the region between the the first and second band. The first two bands are called dielectric and air band, respectively, by analogy with valance and conduction band in solid-state physics.

A very interesting application of photonic crystal slabs is to realize optical nanobeam cavities which can trap the light in a very small volume (V_{mode}) for a long period of time (proportional to the cavity quality factor). Photonic crystal nanobeam cavities can be formed by introducing a defect

to one of these parameters: holes size, dimension of the slab, refractive index, and the spacing between holes. The simplest case of such defect is shown in Fig. 1.4 where one hole at the cavity center is removed. Such changes will pull a mode from the dielectric band or air band into the bandgap and cavity resonance starts to appear. Because the transnational symmetry is broken, the wave vector is no longer conserved and the cavity resonance leaks to light-cone modes, therefore, called leaky mode. We note that this type of point defect has a huge radiative loss and not really desirable for achieving high Q/V value.

In chapter 2, we develop a new design for nanobeam cavities to mitigate the radiative loss. Simulation results show that the figure of merit Q/V value could reach up to 10^8 and transmission to the waveguide mode exceeds 70%. The proposed design is based on a new scalable approach developed to reduce the footprint of nanobeam cavities by more than 50% without lowering the cavity Q/V value or its transmission. This design can be used as a platform for quantum networks which require high interaction between the photons and atoms. In chapter 2, we discuss cavity QED figure of merits for a system consists of a single diamond nano crystal that contains a GeV color center placed on top of the design nanobeam cavity. We show that the strong coupling regime can be reached with very compact and simple nanobeam cavity. Besides the numerical simulations, we explain the fabrication process for nanobeam cavities based on GaP material and how to overcome challenges encountered during the fabrication procedure.

In chapter 3, we extend the new design and implement it for nanobeam cavities based on silicon nitride material films. Despite the low index of refraction associated with the Si_3N_4 films, the simulated Q/V value could reach up to 10^5. This design is used for cavity QED analysis for a system that consists of a GeV color center and Si_3N_4 nanobeam cavity. We show that the strong coupling regime can be achieved using Si_3N_4 nanobeam cavities despite the low cooperativity compared to the GaP case. In addition, we fabricate and characterize nanobeam cavities based on Si_3N_4 films grown by PECVD and LPCVD techniques. We experimentally demonstrate quality factor of $Q \sim 10^4$ for resonances around ZPL of GeV center ($600nm$ wavelength).

In chapter 4, we address the coupling between optical fiber and Si_3N_4 waveguides. We develop

a reliable scheme to achieve efficient fiber-waveguide coupling by means of adiabatic mode transfer using finely tapered fiber and waveguide. We explain the fabrication process of tapered fiber tips and related characterizations. We experimentally demonstrate an efficient coupling of 96% with a high degree of both accuracy and precision.

2. GALLIUM PHOSPHIDE NANOBEAM CAVITIES*

2.1 Introduction

Nanobeam cavities have recently gained more attention due to their high quality factor, comparable to 2-D photonic crystal cavities, and sub-wavelength footprint. The strong light localization in nanobeam cavities characterized by mode volume (V_{mod}), the effective volume in which light is stored in the resonator. The mode volume can be expressed in terms of peak energy density as:

$$V_{\text{mod}} = \frac{\int n^2(r)E^2(r)dr}{|n^2(r)E^2(r)|_{\text{max}}} \tag{2.1}$$

where E and n are the electric field magnitude and refractive index of the profile mode, respectively. Here, we note that this definition is only accurate if the the cavity finesse is finite, which is the case in photonics cavities. A new generalized definition of the mode volume was proposed, which is well-behaved for both high and low finesse resonators [23].

Another figure of merit is the temporal confinement of light in the resonator characterized by quality factor (Q), which can be interpreted in different ways. First, the Q is dimensionless life time describing the number of optical cycles before the stored energy decays to $\exp^{-2\pi}$. Second, 1/Q is a dimensionless decay rate describing the ratio of the energy dissipated per cycle to the energy stored in the resonator. Third, Q is the ratio of the frequency to the bandwidth of the resonator mode [20]:

$$Q = \frac{\lambda_{\text{resonance}}}{\delta\lambda} \tag{2.2}$$

As we are particularly interested in the nanobeam cavities, we will examine the decay mechanisms of the cavity resonance related to nanobeam cavities. Theses mechanisms are shown in Fig. 2.1 (a). The first decay goes through the uniform dielectric strip (which works as a waveguide)

*Part of the result reported in this chapter is reprinted with permission from "Compact design of a gallium phosphide nanobeam cavity for coupling to diamond germanium-vacancy centers" by Alajlan, A. and Cojocaru, V. and Akimov, A. V., Opt. Mater. Express 9, 1678-1688 (2019), Copyright (2019) by The Optical Society.

on either side of the cavity structure, denoted as $1/Q_w$. The other decay scatters the light in the surrounding medium (air if the cavity is suspended), denoted as $1/Q_r$. Therefore, the total quality factor can be written as the sum of the two decay rates:

$$\frac{1}{Q_{\text{total}}} = \frac{1}{Q_{\text{w}}} + \frac{1}{Q_{\text{r}}} \tag{2.3}$$

Intuitively, the first component $1/Q_{\text{w}}$ can be significantly suppressed by elongating the cavity footprint or increasing the number of holes in both sides of the nanobeam cavity, whereas $1/Q_r$ is totally independent from the number of holes. In practice, the nanobeam cavity needs to be efficiently coupled to the waveguide in order to attain high transmission when probing the cavity. The transmission of the cavity resonant mode can be expressed as:

$$T = \frac{Q_{\text{total}}}{Q_{\text{w}}} \tag{2.4}$$

In order to achieve near unity transmission, the cavity quality factor should be limited by Q_r (i.e., $T \rightarrow 1$ requires that $1/Q_{\text{r}} << 1/Q_{\text{w}}$).

In general, ultrahigh quality factor nanobeam cavities can be obtained by two techniques. The first one is to adjust the holes shape and spacing while keeping the nanobeam width uniform [24–26]. The second technique is to modify the nanobeam width while keeping the holes shape uniform [27, 28]. while both methods require expanding the cavity footprint, and therefore adding more holes in order to obtain ultrahigh Q/V regardless of the chip material. One drawback of such long cavities is that the fundamental mode will be perplexed by a excessive amount of high order modes. In addition, the real transmission of the cavity mode would be greatly ruined by the increasing number of holes.

In this chapter, we describe a new promising design for nanobeam cavities that can support a mode with ultrahigh Q/V value and high transmission. The geometry of the designed device is illustrated in Fig.2.2 (a). The clear distinction between our design and previous designs is the extra semicircular holes added on each side of hole segment. While this technique is scalable and

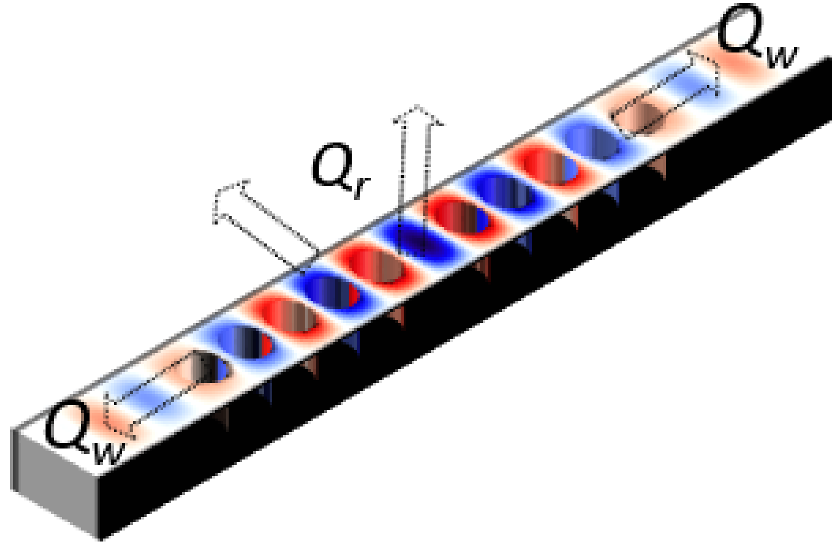

(a)

Figure 2.1: Schematic of a typical nanobeam cavity. Q_w and Q_r refer to the decay mechanism of the cavity resonance due to coupling to the waveguide mode and radiation mode, respectively.

can be essentially implemented in any nanobeam cavity design with circular holes, we employ the quadratic tapering method of the nanobeam width [27] for the following reasons. First, tapering nanobeam width is easy to adjust and control during the fabrication as well as in simulations. Moreover, this method has more tolerance as it tapers relatively large features (nanobeam width) rather than small features (nanobeam radius).

In this chapter, We will first discuss the concept of the mirror strength which is the underlying principle for compacting the cavity footprint. A comparison between our design and other designs in literature will be provided to manifest the advantages of our design. After that, the details of our design will be explained along with optimizations for some geometric parameters such nanobeam width and thickness based on FDTD simulations. Then, we discuss cavity QED with GeV embedded in diamond nanocrystal that is placed on top of the cavity we propose. We consider a range of sizes for diamond nanocrystals as synthesis technologies are yet to produce small sizes with the same properties as in bulk diamond, specifically for GeV centers. Finally, we explain the fabrication procedure for Gallium Phosphide (GaP) nanobeam cavities suspended in air. Here, we

introduce a new fabrication method that uses a silicon nitride hard mask instead of the resist.

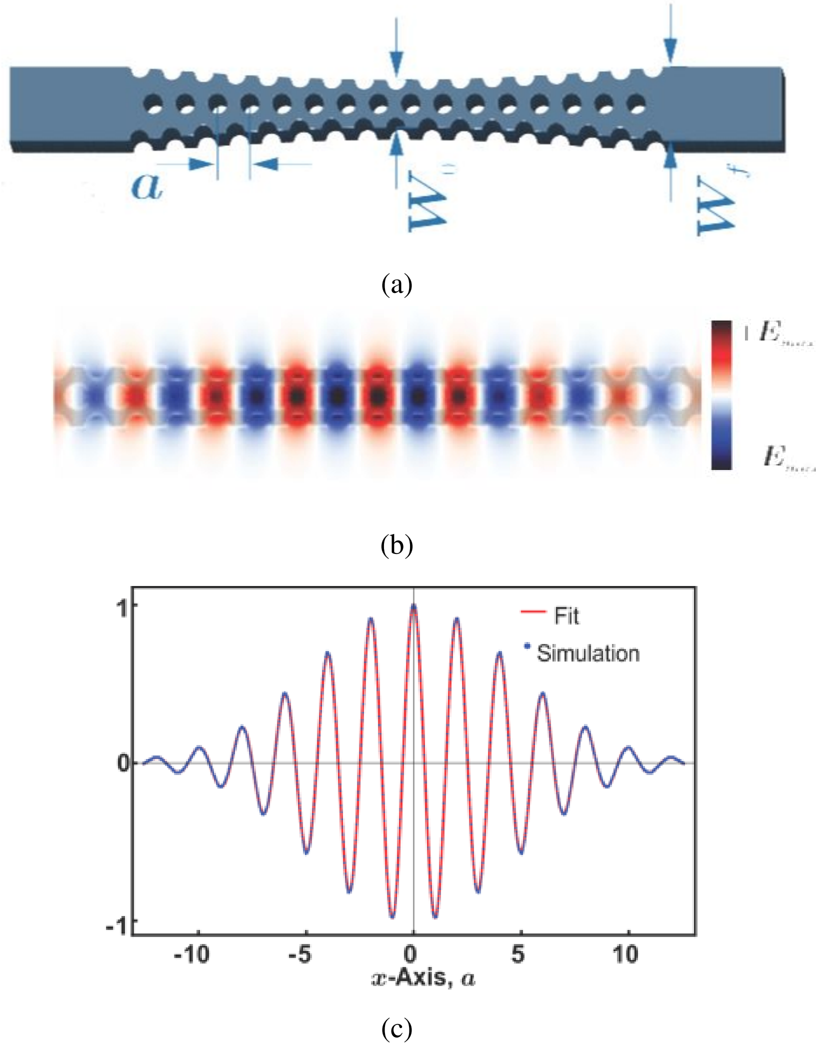

Figure 2.2: (a) Sketch of tapered nanobeam cavity with semicircular holes added to each side of the hole segment. (b) $E_y$field distribution of the fundamental TE mode in the middle (z = 0) plane of the nanobeam cavity. (c) E_y field distribution for the TE fundamental mode obtained from FDTD simulations (blue dots) and from an analytic formula (red line): $E_y = \cos\left((x - x_0)\frac{\pi}{a}\right)\exp\left(-\sigma^2(x - x_0)\right)$. Figures (a)-(c) are reprinted with permission from ref. [28].

2.2 Cavity mirror strength

In the case of DBM, the spacial component of evanescent field inside the mirror can be expressed as a product of a sinusoidal wave with a wavevector k, and an envelope function that represents the field attenuation. The scattering loss can be suppressed in the mirror strength when the wave has a delta function in the Fourier transform spectrum with peaks at k = π/a [29]. The envelope function modifies field attenuation in Fourier transform spectrum that is determined by the mirror structure. Since we are studying a nanobeam cavity that is periodic in one dimension, each side of the cavity is considered as DBM. We first calculate the attenuation constant analytically using the plane wave expansion method. Since the dielectric function in photonic crystals is periodic (i.e., $\epsilon(x+a)=\epsilon(x)$), one can expand $\epsilon^{-1}(x)$ in the master equation (1.1) in Fourier series:

$$\epsilon^{-1}(x) = \sum_{m=-\infty}^{\infty} A_{\mathrm{m}} e^{iLmx} \tag{2.5}$$

where $L = 2\pi/a$. For simplicity, we assume that only components with m = 0 and ± 1 are dominant in the expansion (2.5):

$$\frac{1}{\epsilon(x)} \approx A_0 + A_1 e^{iLx} + A_{\text{-}1} e^{-iLx} \tag{2.6}$$

The first two Fourier components can be expressed as [30]:

$$A_0 = \frac{f}{\epsilon_1} + \frac{1-f}{\epsilon_2} \tag{2.7}$$

$$A_1 = 2f\left(\frac{1}{\epsilon_1} - \frac{1}{\epsilon_2}\right)\frac{J_1(LR)}{LR} \tag{2.8}$$

where f is the ratio of the area of the hole to the area of the unit cell, ϵ_2 and ϵ_1 are the dielectric function of the photonic crystal material and the surrounding, respectively. Now on, we consider one-dimensional Gallium Phosphide (GaP) nanobeam cavity suspended in air and the cavity resonance is adjusted at $\lambda = 600$ nm close to the zero-phonon line of the GeV center. Therefore,

dielectric constants whould be $\epsilon_1 = 1$ and $\epsilon_2 = 3.36$.

Modes localized within a photonic bandgap have a complex wavevector $k + i\gamma$. The imaginary component denotes the attenuation of the field due to the mirror reflection which is called the mirror strength. Since the bandgap locates between the first two bands (dielectric and air band) at the edge of Brillouin zone (BZ), we can consider only solutions for $k = \pi/a$. The frequency and wavevector can be written as:

$$\omega = (1 - \Delta)\sqrt{A_0}\frac{c\pi}{a} \tag{2.9}$$

$$k = (1 + i\gamma)\frac{\pi}{a} \tag{2.10}$$

where Δ is the detuning from the mid-gap frequency. Substituting Eq. (2.9) and Eq. (2.10) into the master equation (1.1) we obtain:

$$\gamma^2 \approx \frac{{A_1}^2}{4{A_0}^2} - \Delta^2 \tag{2.11}$$

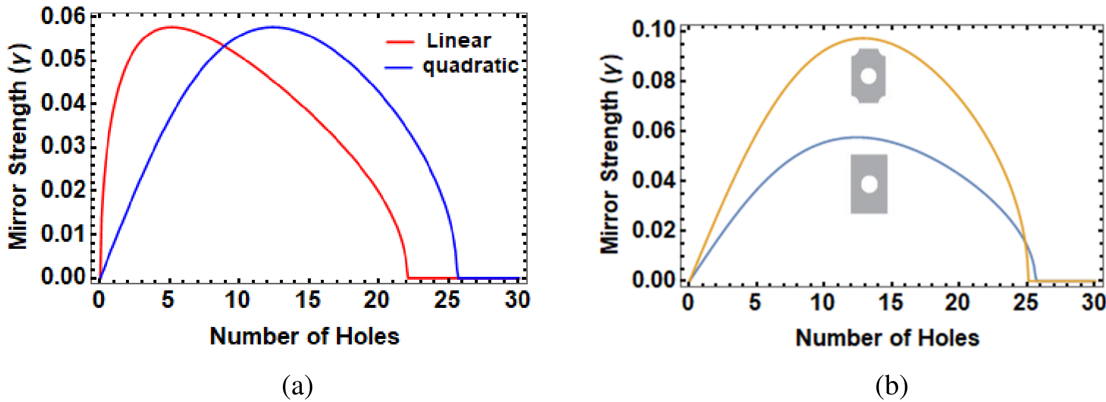

(a)

(b)

Figure 2.3: (a) Mirror strength of each hole segment for linear (red) and quadratic (blue) tapering profile. (b) Mirror strength of each hole segment for a nanobeam with only central holes (blue) and with additional semicircular holes (yellow). Both figures were obtained from the analytic expression Eq. (2.11) derived from the plane wave expansion method.

The radiation loss characterized by $1/Q_r$ depends heavily on the filed profile in the cavity.

Studies have shown that this field profile should be Gaussian-like in order to achieve high quality factors [31]. A Linear increase of the mirror strength as a function of the hole position along the cavity has been shown to form such Gaussian-like field profile, suppressing greatly scattering loss estimated by Fourier space analysis [32]. Figure 2.3 (a) shows the mirror strength γ for different tapering profiles calculated from the analytic expression Eq. (2.11). It can be seen that the mirror strength increases linearly for the quadratic tapering profile, whereas the linear tapering leads to an exponential rise of the mirror strength. Similar results have been reported for other designs based on tapering holes radii instead of the nanobeam width [33].

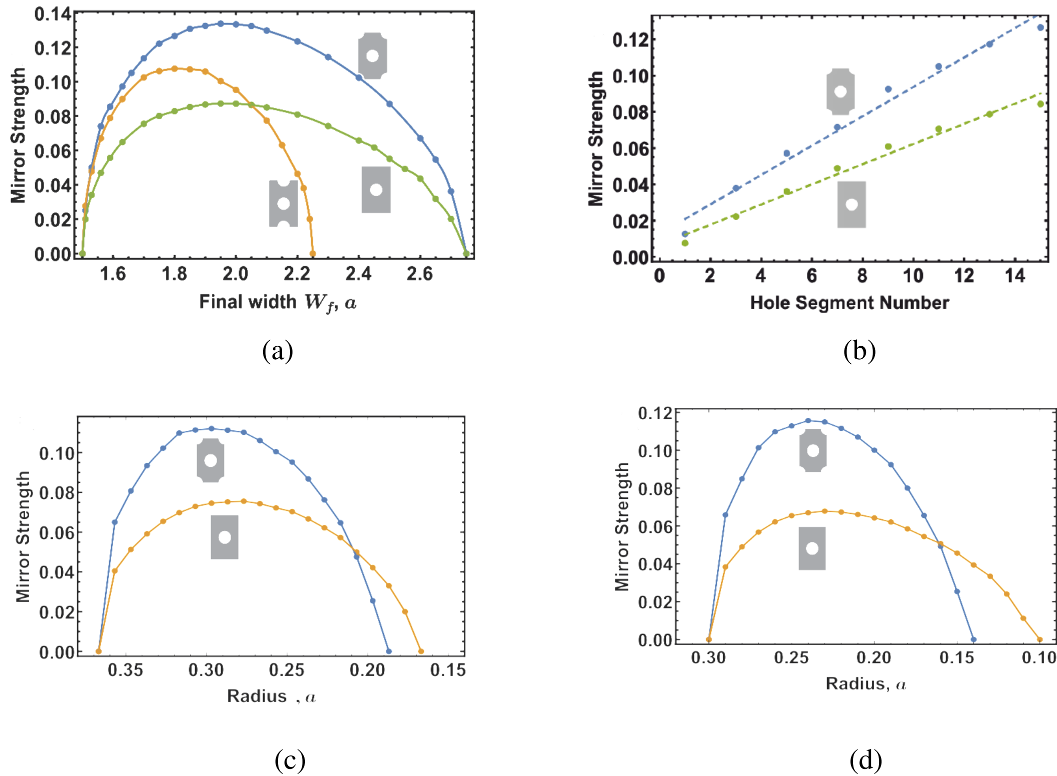

Figure 2.4: Mirror strength obtained from FDTD simulations. (a) Mirror strength as a function of nanobeam final width for three configurations: only central holes (green), central holes with in-phase semicircular holes (orange), central holes with out-of-phase semicircular holes (blue). (b) Mirror strength as a function of the hole segment number after quadratic tapering for only central holes (green) and out-of-phase semicircular holes (blue). The dashed line is a linear fit with $R^2 = 0.98$. (c) & (d) Mirror strength as a function of hole radius for two nanobeam designs with (blue) and without (orange) semicircular holes suggested by Qimin et al. [33] and Notomi et al. [34], respectively. Figures (a)-(d) are reprinted with permission from ref. [28].

Despite the gain in the quality factor, the quadratic tapering method has the disadvantage of a large cavity footprint and therefore the large mode volume, as clearly shown in Fig. 2.3 (a). More importantly, large footprint cavities suffer from the high order modes beside the fundamental mode, downgrading the cavity performance. To address this issue, we propose a new design that differs from the other designs by the extra semicircular holes added to each hole segment, as depicted in Fig. 2.2 (a). The field profile of the cavity Fundamental mode inside the cavity has been analyzed numerically. Figure 2.2 (c) shows the field distribution along the cavity axis, which is fitted by an analytic formula to confirm the Gaussian-like profile.

Figure 2.3 (b) shows that extra semicircular holes result in a significant increase of the mirror strength. The reason is that the Fourier series coefficient in Eq. 2.8 increases proportionally to the filling fraction of low index material. Even though the area of the individual holes does not change, the filling fraction can be increased by adding semicircular holes per unit cell. On the other hand, increasing the size of individual holes would not results to an equivalent gain in mirror strength since the periodicity of hole limits the maximum of hole radius only to half spacing between holes, i.e., $r < 1/2a$. Furthermore, large radii would result in very low transmission as the scattering loss increases proportional to the hole radius.

Although we have calculated the mirror strength using the analytic expression Eq. (2.11), the results shown in Fig. 2.3 do not take into account important parameters, e.g. thickness of the slab and the actual position of the semicircular holes. An accurate analysis was proposed previously to calculate the mirror strength by inserting the frequency of each band into the following formula [32]:

$$\gamma = \sqrt{\frac{(\omega_1 - \omega_2)^2}{(\omega_1 + \omega_2)^2} - \frac{(\omega_{\text{res}} - \omega_0)^2}{{\omega_0}^2}} \tag{2.12}$$

where ω_1, ω_2, ω_0, and ω_{res} are the air band edge, dielectric band edge, middle frequency and resonant frequency, respectively. The results for the mirror strength based on Eq. 2.12 are shown in Fig. 2.4. The contrast between the mirror strength corresponding to each design is similar to what is shown previously in Fig. 2.3. Interestingly, the maximum mirror strength is achieved

when semicircular holes are adjusted such that they are shifted horizontally from the central holes by $1/2a$, where a is the lattice constant. In addition, numerical simulations show that in-phase semicircular holes leads to a huge scattering loss and bad transmission. Therefore, we do not consider this design in the following optimizations. On the other hand, the linear increase of the mirror strength can be obtained by slowly tapering the corresponding nanobeam widths, as shown in Fig 2.4 (b). We note that the final width should be chosen before the point where the mirror strength start to saturate in order to make it linear. In the next section, we study Q/V dependence on some width parameters in more details.

Even though semicircular holes have been applied for a specific design, the idea is scalable and can be implemented to other nanobeam designs. To verify that, Figure 2.4 (c) and (d) show mirror strength when semicircular holes are applied to different designs [33, 34]. The resulting mirror strength in both designs has enhanced considerably, in agreement with our claim. We note that the difference of the enhancement between the two designs is due to the difference in width parameters chosen for each nanobeam design.

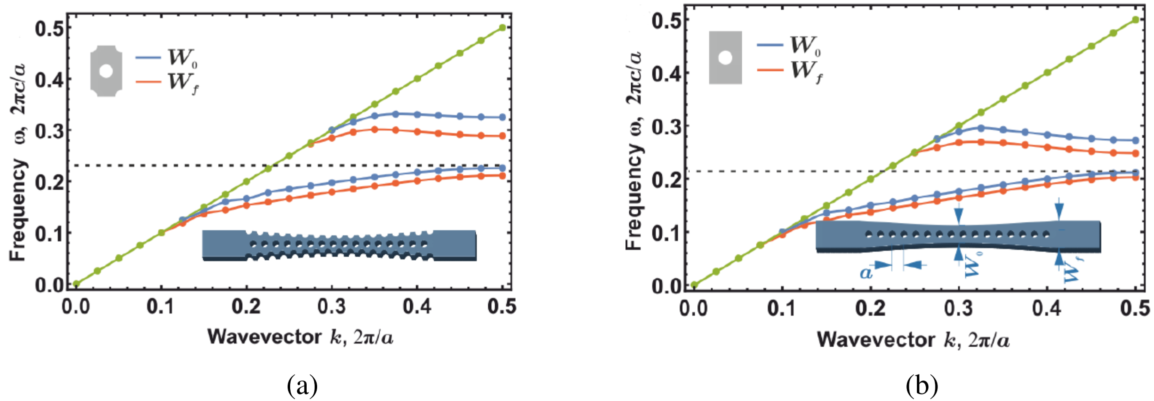

Figure 2.5: (a) & (b) TE band structure for nanobeam cavity with additional semicircular holes and with only central holes, respectively. The dashed line marks the cavity resonant frequency which is found to be 1% less than the dielectric band-edge of the first hole. The bandgap includes all modes between dielectric band-edge and extend to the air band-edge of the last hole (i.e., between the two red lines). All geometries are assumed to be GaP slab suspended in air (n =3.36) and the thickness is the same as the spacing between holes. Figure (a) & (b) are reprinted with permission from ref. [28].

2.3 Geometric optimizations

Using 3D-FDTD numerical simulations free software (MEEP), we optimize the nanobeam width and thickness based on Q/V value and number of holes needed in each side of the cavity. The first step is to determine the initial width $W_{\rm i}$ (the width a the cavity center). In principle, a small initial width shifts the dielectric band towards the light line, and thus causes scattering losses, whereas a large width pulls high order modes into the bandgap and decreases its size. Examining the band structure for different initial widths, we found that $W_{\rm i}/a = 1.5$ is a good compromise. Then, we select the final width $W_{\rm f}$ at the corner of the cavity such that the corresponding mirror strength is high enough but not saturated. For the first approximation, $W_{\rm f}/a = 1.8$ satisfies the previous condition. The corresponding band structure for TE modes is shown Fig. 2.5 (a) and (b). The size of the bandgap for our design has slightly broadened compared to the original geometry (without semicircular holes) which indicates lower scattering losses.

Although we have selected the initial and final cavity width based on the band diagram, a further calculations based on Q/V ratio is more accurate. Since our design considers tapering the nanobeam width, our optimizations have been done for the initial width ($W_{\rm i}$) and final width ($W_{\rm f}$). In Fig. 2.6 (a), we examine Q/V ratio and transmission dependence for out-of-phase holes geometry on three final widths: $W_{\rm f}/a = 1.7$, $W_{\rm f}/a = 1.8$, and $W_{\rm f}/a = 1.9$. Our results reveal that small final widths are favorable for ultrahigh Q/V value as the cavity transmission drops fast for large nanobeam widths as a result of non-adiabatic tapering profile. In addition, small final widths are also recommended to make the associated mirror strength linear which would results in Gaussian-like field profile, as mentioned in the previous section. Similar examination has been done for the central holes design, see Fig. 2.6 (b). For this case, the difference between the three final widths becomes not as inconsequential as the semicircular holes design. That indicates that the tolerance of this geometry is more profound than the first structure, which is one drawback of the semicircular holes.

Despite the fact that small final nanobeam widths have better Q/V and transmission dependence, that does not necessarily indicate that the small final widths are preferable. In fact, the

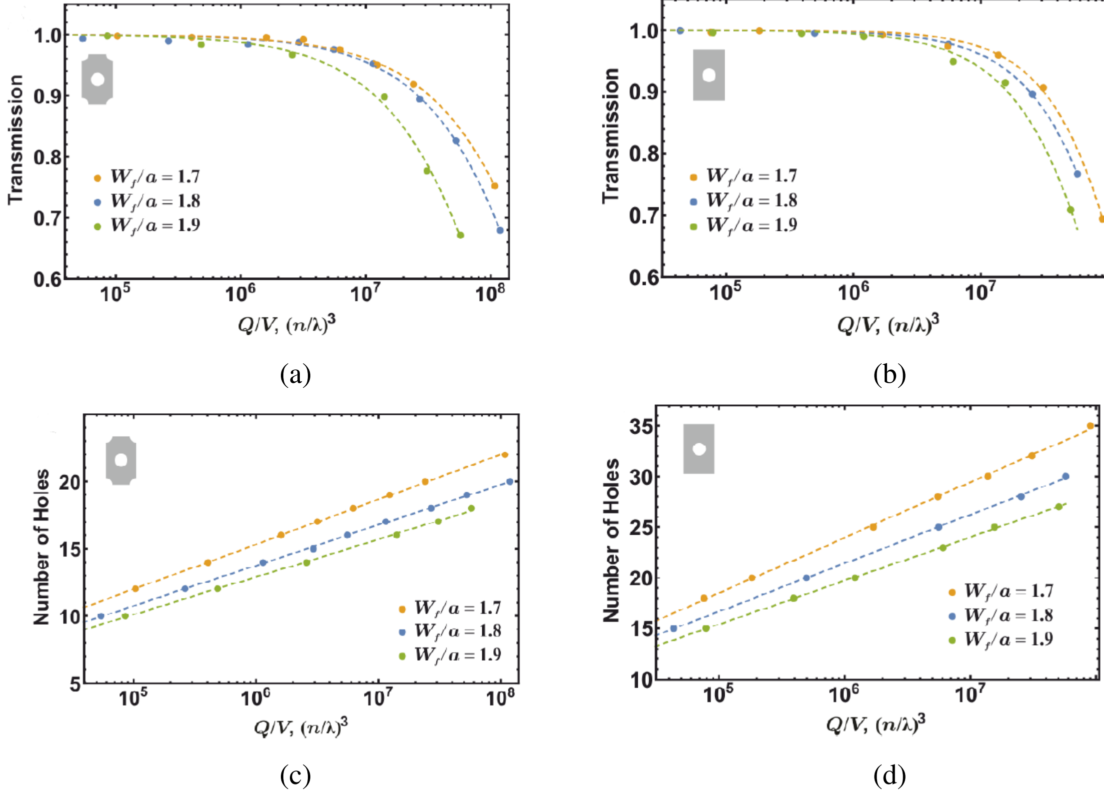

Figure 2.6: (a) & (b) transmission dependence on Q/V ratio for different nanobeam final widths in semicircular holes and central holes design, respectively. (c) & (d) number of holes dependence on Q/V ratio for different final widths in semicircular holes and central holes design, respectively. The initial width is consistent (W_i/a = 1.5) for the plots. Figure (a) & (c) are reprinted with permission from ref. [28].

enhancement of Q/V values may not be as significant as the nanobeam footprint. The Q/V value and cavity footprint dependence is plotted in Fig. 2.6 (c). It is obvious that the cavity footprint, which is characterized by the number of holes, increases as the final width shrinks close to the initial width and one has to consider both parameters before fabricating any nanobeam device. Based on our optimizations, it seems that $W_{\mathrm{f}}/a = 1.8$ is a good trade-off between the number of holes and the Q/V value. The Q/V value for our design could reach up to 10^8 with transmission higher than 70% after optimizing the nanobeam final width.

On the other hand, the nanobeam initial width is also an important parameter that plays a crucial role in the Q/V value and nanobeam footprint. In figure 2.7 (a), we examine the Q/V value for

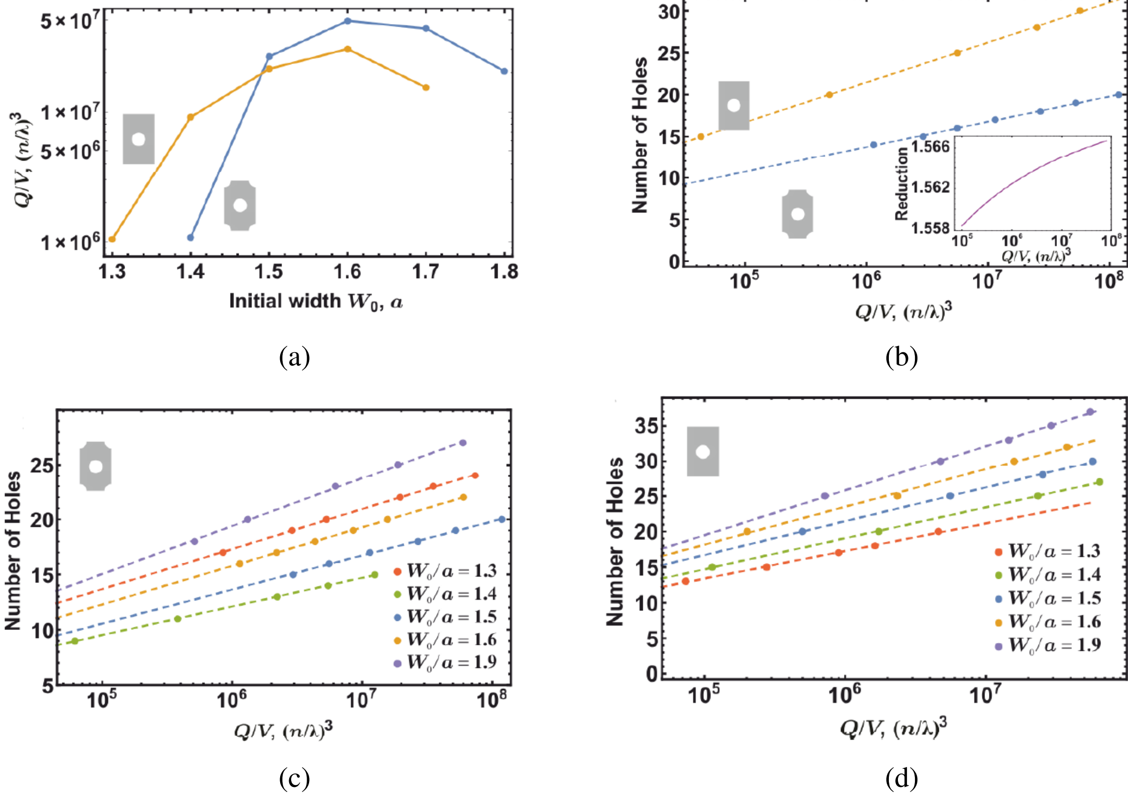

Figure 2.7: (a) The dependence of Q/V value taken at 90% cavity transmission on the nanobeam initial width. The difference between the final and initial width is fixed, $\Delta W/a = 0.3$. (b) The number of holes dependence on Q/V calculated for $W_{\mathrm{i}}/a = 1.5$ in both geometries. (inset) Reduction factor in number of holes as a function of Q/V value gained by adding semicircular holes. (c) & (d) The number of holes dependence on Q/V calculated for different nanobeam initial widths. Figure (a) & (b) are reprinted with permission from ref. [28].

different nanobeam initial nanobeam widths. In general, Q/V value increases gradually as the nanobeam width broadens to a critical width before it declines again at large widths. Interestingly, Q/V value plunges one order of magnitude for small nanobeam widths, as can be seen in $W_{\mathrm{i}}/a = 1.4$ for the cavity with semicircular holes, and at $W_{\mathrm{i}}/a = 1.3$ for the cavity with only central holes. The reason is that the cavity resonance for such small initial widths generally shifts distinctly towards the light line, causing the light to radiate in air.

Besides Q/V and transmission dependence, we have analyzed the cavity footprint or number of holes for different initial widths. The dependence of initial width on the cavity footprint is shown in Fig. 2.7 (c). Unlike the trend for final nanobeam width, the nanobeam footprint increases

proportionally with the initial width, as a results of the change in the cavity resonance. Similar behaviour can be seen for nanobeam cavities with only central holes, see Fig. 2.7 (d). By comparing both the Q/V value and the number of holes, the initial width $W_{\rm i}/a = 1.5$ may be the optimal initial width.

The reduction of the nanobeam footprint due to the semicircular holes is so significant. Figure 2.7 (b) shows that semicircular holes can reduce the cavity footprint by 50% while maintaining the cavity Q/V and transmission. This reduction in the cavity footprint is in line with the enhancement of the mirror strength calculated in the previous section. We noted that the reduction factor depends to some extent on the nanobeam initial width. To achieve a great reduction factor, a relatively small initial width is recommended, see Fig. 2.4 (d).

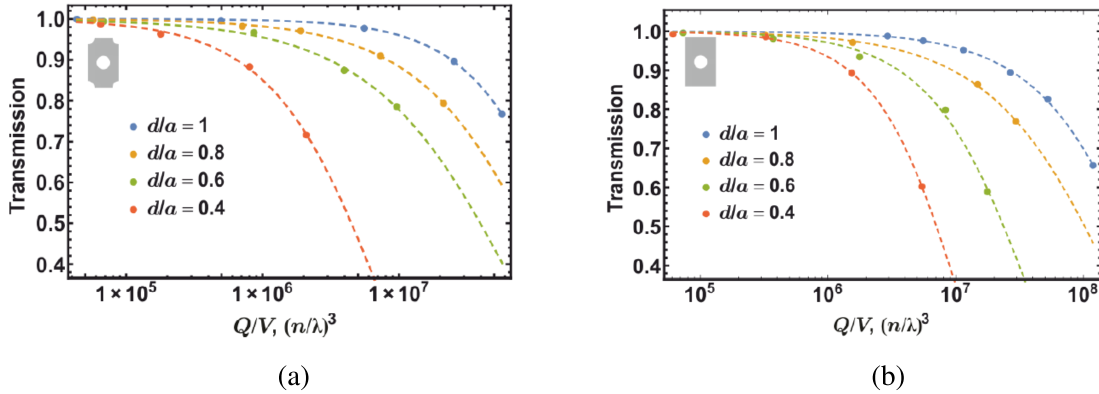

(a) (b)

Figure 2.8: Cavity Q/V and transmission dependence on the nanobeam thickness. We consider the following nanobeam widths: $W_{\rm i}/a = 1.5$ and $W_{\rm f}/a = 1.8$, based on our width optimizations discussed previously. Figure (a) is reprinted with permission from ref. [28].

The nanobeam thickness is rarely considered and optimized since it is predetermined by the choice of chip wafer. Nevertheless, it is very important to optimize the nanobeam thickness carefully before growing the wafer or buying a commercial standard thickness as the cavity Q/V depends on the nanobeam thickness. In Fig. 2.8, transmission dependence on Q/V values is plotted for different nanobeam thicknesses. It can be seen that Q/V value increases proportional to the thickness as a result of the increase in the corresponding bandgap size. However, Q/V value

tends to drop again after reaching a critical thickness. The reason of such drop is that high order modes start to show up into the bandgap at large thicknesses [20]. Notably, we found that Q/V value and number of holes dependence is insensitive to the changes in nanobeam cavity thickness for both designs discussed above. In the next section, we will discuss the thickness role in the case of a quantum emitter placed on top of a nanobeam cavity.

2.4 Cavity QED analysis with GeV center

In this section, we consider a model system that consists of a single two-state atom (GeV center) placed at the center of the top nanobeam surface of the nanobeam cavity, as illustrated in Fig. 2.9 (a). The interaction of the single GeV center with the cavity resonant is determined by the Jaynes-Cummings-Hamiltonian [35]:

$$H_{\mathrm{JC}} = \frac{\hbar\omega_{\mathrm{a}}}{2}\sigma_{\mathrm{z}} + \hbar\omega_{\mathrm{c}}a^{\dagger}a + i\hbar[ga^{\dagger}\sigma^{-} - g^{*}a\sigma^{+}] \tag{2.13}$$

The first and second component in Jaynes-Cummings-Hamiltonian represent the energy of the atomic excitation and the electromagnetic field inside the cavity, respectively, whereas the third term represents the energy due to the interaction of the atom with a electromagnetic field. As we are particularly interested in studying the interaction between the single photon field in the nanobeam cavity and the GeV center, it is necessary to calculate parameters governing the dynamics of cavity QED systems. The key parameters are: atom-photon interaction rate g (vacuum Rabi frequency), atomic decay rate γ_{sp} (spontaneous emission rate), and cavity field decay rate κ. The Rabi frequency is defined as :

$$g = \frac{\boldsymbol{d} \cdot \boldsymbol{E}}{h} \tag{2.14}$$

where d and E are the dipole moment of the GeV center and the single photon electric field amplitude, respectively.

The single photon electric field amplitude for a given cavity mode can be written as:

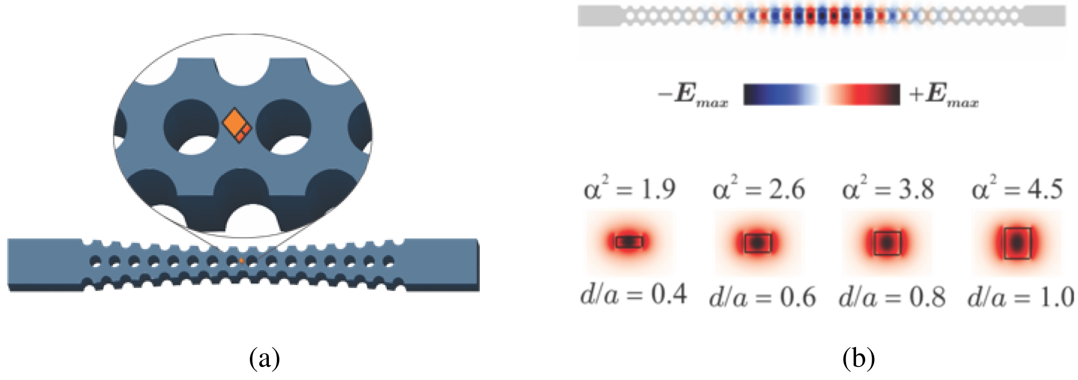

Figure 2.9: (a) Sketch of DNC placed on top of a nanobeam cavity. (b) E_y cross sections of the TE fundamental mode. α^2 is the ratio of the energy density in the GaP nanobeam cavity to the maximum energy density at the DNC calculated for different nanobeam thicknesses. Figure (a) & (b) are reprinted with permission from ref. [28].

$$E = \sqrt{\frac{\pi \hbar c}{\epsilon_0 \lambda {n_{\mathrm{G}}}^2 V_{\mathrm{mod}}}} \tag{2.15}$$

where $n_{\mathrm{G}} = 3.36$ is the refractive index of GaP, λ is the the cavity resonance, and V_{mod} is the mode volume of the cavity resonance. Throughout our calculations, we will assume that cavity mode is tuned to the ZPL optical transition of GeV center (i.e., $\lambda = 602$ nm).

The dipole moment of the GeV can be derived from its spontaneous emission lifetime (τ) which can be express as [36]:

$$\frac{1}{\tau} = \frac{2\pi}{\hbar^2} |Ed|^2 \frac{\omega^2 {n_{\mathrm{dnc}}}^3 V}{3\pi^2 c^3} \tag{2.16}$$

Substituting Eq. 2.15 gives:

$$d = \frac{1}{2} \sqrt{\frac{3\gamma_{\mathrm{sp}} \epsilon_0 \lambda^3 \hbar}{2\pi^2 n_{\mathrm{dnc}}}} \tag{2.17}$$

Then, the Rabi frequency can be evaluated to give:

$$g = \frac{\eta}{2\alpha} \sqrt{\frac{3c\lambda^2}{\tau n_{\mathrm{dnc}} {n_0}^2 V_{\mathrm{mod}}}} \tag{2.18}$$

Since the ZPL optical transition of GeV center contributes about 60% of the total emission (the rest is associated with a non-radiative emission) [37], the dipole moment must be scaled by $\eta = \sqrt{0.6}$. In contrast, the quantum efficiency of SiV center is less than 10% [38].

In principle, the DNC cannot be embedded inside the cavity except if it is placed in the middle of chip growing process [39], which has not been demonstrated experimentally so far. For simplicity, the DNC is assumed to be on top of the nanobeam cavity. Therefore, the mode volume must be scaled by $\alpha^2 = |n_{\mathrm{G}}{}^2 E_{\mathrm{G}}{}^2|/|n_0{}^2 E_0{}^2|$, the ratio of the maximum energy density in the GaP nanobeam cavity to the maximum energy density at the DNC position. FDTD calculations show that the ratio changes depending on the slab thickness (Fig. 2.9 (b)). On the other hand, we found that the position of DNC is somewhat flexible in the lateral direction. The difference in the maximum energy ratio between the case where the DNC is placed at either cavity lateral edge and the case where it is placed at the center is $\Delta\alpha^2 = 0.3$.

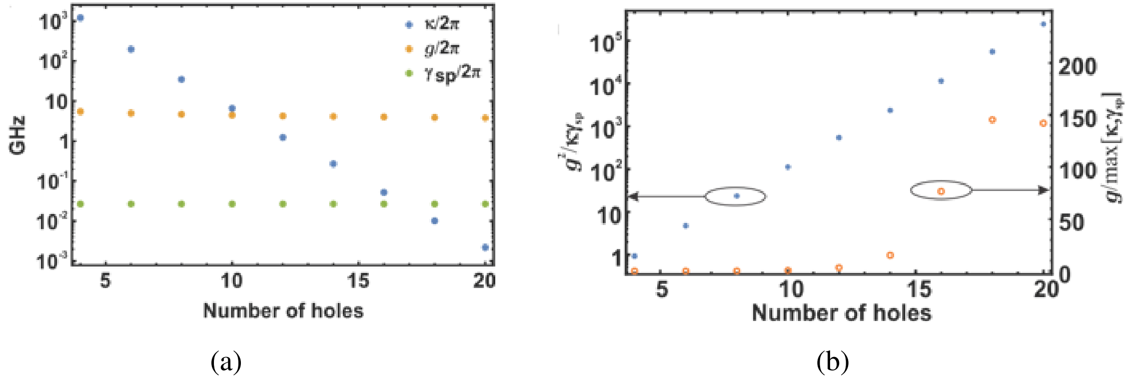

Figure 2.10: (a) Relevant cavity QED rates as a function of number of holes. $\kappa/2\pi$ is the cavity decay rate, $\gamma_{\mathrm{sp}}/2\pi$ is the atomic decay rate of the GeV center, and $g/2\pi$ is the single photon coupling rate. (b) Cooperativity (dots) and weak/strong coupling index (open circles) as a function of number of holes. Figure (a) & (b) are reprinted with permission from ref. [28].

The relevant cavity QED figures of merit is plotted in Fig. 2.10 (a). It can be seen that the cavity field decay rate κ is the only parameter that depends heavily on the number of holes although the Rabi frequency g has a weak dependence due to the changes in the cavity mode volume. The

two regions of particular interest in cavity QED systems are the strong-coupling regime and the weak-coupling regime. The strong-coupling criterion is satisfied when the atom-photon coupling rate exceeds the decay rate of the system, $g > [\kappa, \gamma_{\text{sp}}]_{\text{max}}$. This condition is satisfied for nanobeam cavities with at least 12 holes in each side which corresponds to Q/V of 2.6×10^5. In this regime, atomic energy can be coherently exchanged with the cavity resonant mode at the vacuum Rabi frequency, as described by Jaynes-Cummings Hamiltonian Eq. (2.13). This dynamic of such system is reversible as long as the system is being isolated. As mentioned before, all optical cavities have a finite quality factor that limits (or prevents sometimes) the atom-field interaction by allowing the cavity mode to leak irreversibly into the surrounding.

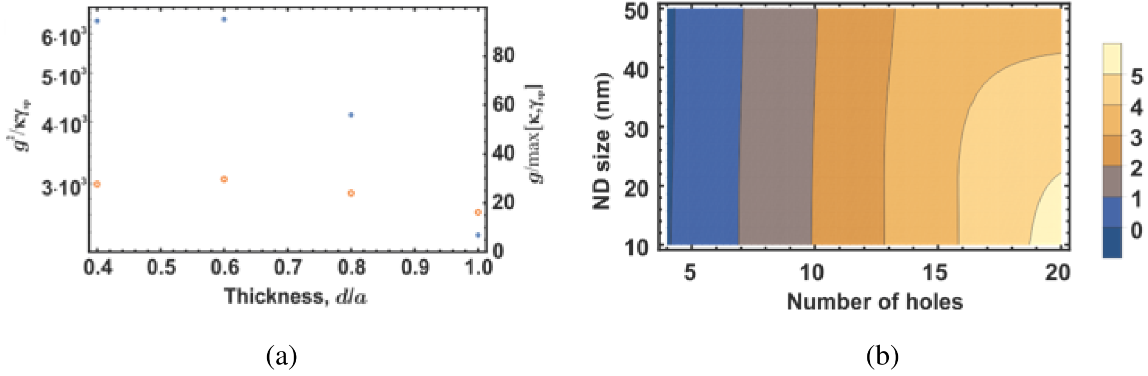

(a) (b)

Figure 2.11: (a) Cooperativity (dots) and weak/strong coupling index (open circles) as a function of nanobeam thickness. We considered cavities with 14 number of holes ($Q/V \approx 10^6$) for all thicknesses to maintain the cavity transmission. (d) cooperativity as a function of number of holes for different DNC sizes. Figure (b) is reprinted with permission from ref. [28].

In the weak-coupling regime, the cavity decay rate exceeds the light-matter interaction rate but the atomic radiative decay rate into the cavity resonant mode exceeds the free space atomic decoherence rate, $\kappa > [g^2/\kappa] > \gamma_{\text{sp}}$. In such scenario, the spontaneous emission rate of the atom will be strongly enhanced by the Purcell factor [40]:

$$F = \frac{3}{4\alpha^2\pi^2}\left(\frac{\lambda}{n}\right)^3 \frac{Q}{V} \tag{2.19}$$

In both coupling regimes, the atom decays predominantly into the cavity mode, permitting efficient photon collection. The cooperativity, defined as $C = g^2/\kappa\gamma_{\text{sp}}$, in the strong-coupling regime in our system varies from 10^2 up to 10^5 depending on the cavity number of holes. Furthermore, the cooperativity also depends on the nanobeam thickness. In Fig 2.11 (a), we consider a nanobeam cavity with 14 holes, for example, to maintain the cavity transmission at different thicknesses and push away cavity high order modes. It is clear that the cooperativity can enhance one order of magnitude for thinner nanobeam cavities mainly due to the gain in α^2 value. Our results represent nearly two orders of magnitude improvement compared to the previous analysis using a similar scheme [41].

Although techniques have been developed recently to yield sub-10-nm DNCs at low cost [42, 43], some newly invented color centers may not attainable in such tiny sizes. Therefore, it is important to quantify the effect of the DNC size on our system. We performed simulations of a GaP nanobeam cavity and a cube NDC on the top surface with a refractive index of 2.4 and different sizes ranging from 10 nm to 50 nm. The results are shown in Fig. 2.11 (b). Interestingly, DNC with 10 nm size has no impact on the cavity Q/V value, therefore, the interaction between the color center and the cavity does not depend on the size of the DNC nor on its shape. For DNC with sizes larger than 10 nm, the impact on low Q/V cavities is very minor, whereas the ultrahigh Q/V cavities would suffer from an exponential decrease in their Q/V value as the DNC size increases. Nevertheless, the condition for strong coupling is still satisfied and the cooperativity value will be limited within a small range as quality factor reaches a saturation limit after a certain number of holes.

2.5 Fabrication of GaP nanobeam cavities

Gallium phosphide (GaP) is a typical IIIâĂŞV compound semiconductor that has an indirect band gap of 2.26 eV. It has been used mainly as an efficient low-cost wafers for visible LEDs

[44]. Nevertheless, GaP can be used for a wide range of applications such as solar cells [45], gravitational waves [46] and nonlinear optics [47]. Despite the progress in the growth of bulk GaP, single crystalline GaP nanolayers are very hard to grow especially on metallic substrates. Our GaP chip has been grown by gas-source molecular beam epitaxy at Humboldt University. The schematic chip structure is shown in Fig. 2.12 (a). It consists of a 120 nm GaP membrane on top of 1 μm-thick sacrificial layer ($Al_{0.91}GaP_{0.09}$) and 250 nm overgrowth GaP membrane on top of bulk GaP wafer (001) which ensures the lattice matching between theses layers. The surface profile of the top GaP membrane was measured by an atomic force microscope (AFM). The surface profile for a large and small area is shown in Fig. 2.12 (b) & (c), respectively.

Speed (rpm)	Thickness (nm)
1500	55
2000	40
3000	35

Table 2.1: HSQ thickness for different spin coating speeds.

In order to demonstrate the proposed devices, we have developed the fabrication procedure for suspended gallium phosphide photonic devices. We carried out the fabrication for GaP membranes using two approaches: negative resist and positive resist with Si_3N_4 hard mask. The fabrication process flow for the negative resist is depicted in Fig. 2.13. The resist used here is hydrogen silsesquioxane (HSQ, XR-1541-002 from Dow Corning Inc.) negative resist that can be directly spin coated on GaP substrates without an adhesion promoter such as HexaMethylDiSilazane (HMDS) and surpass 3000. The thickness of the resist is determined by the coating speeds, see Table 2.1. After the spin coating, a typical prebaking was performed at 250°C for two minutes. We note that the temperature and time are flexible for most of the EBL resists.

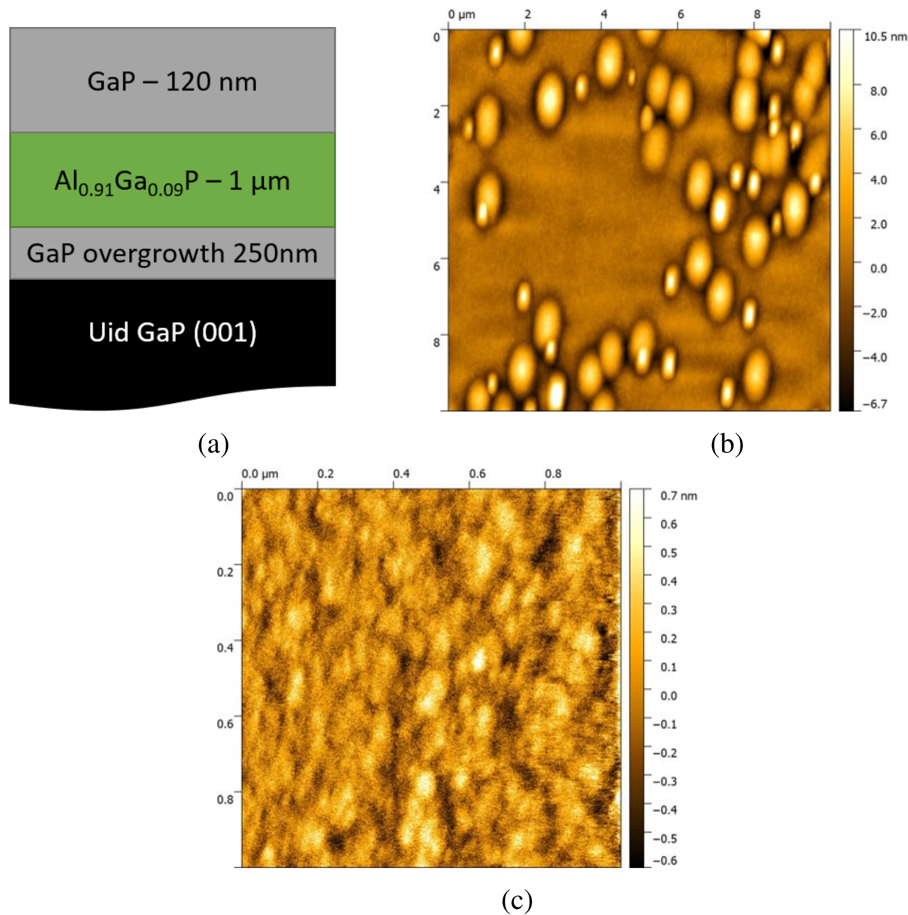

(a) (b) (c)

Figure 2.12: (a) Schematic of the layers grown in the GaP substrate. (b) Atomic force microscope scan for $10 \times 10\ \mu m^2$ area of the top GaP membrane. The corresponding root mean square is 2.3 nm. (c) Atomic force microscope scan for $10 \times 10\ \mu m^2$ area between the rough points. The corresponding root mean square is 0.2 nm.

Next, the resist is scanned by a focused beam of electrons via EBL equipment (30kV, TESCAN MIRA3) operting at 30 kV. The details of EBL process are explained in Appendix (B). Unexposed resist was removed in MF-319 developer (70 seconds at room temperature). For a high contrast, it is recommended to use 25 % tetramethyl ammonium hydroxide (TMAH) developer for only 15 seconds [48]. After the development step, the pattern is formed in the silica surface which works as a mask in the consequent etching step.

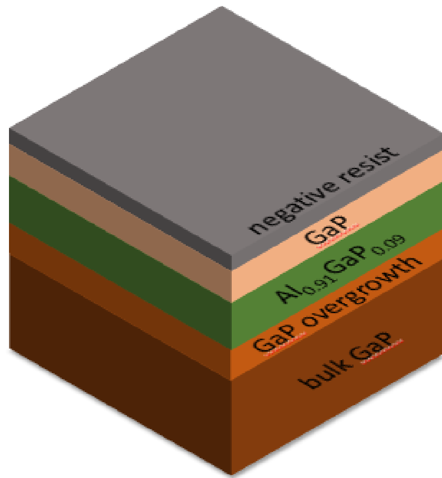

(a) Spin coating HSQ

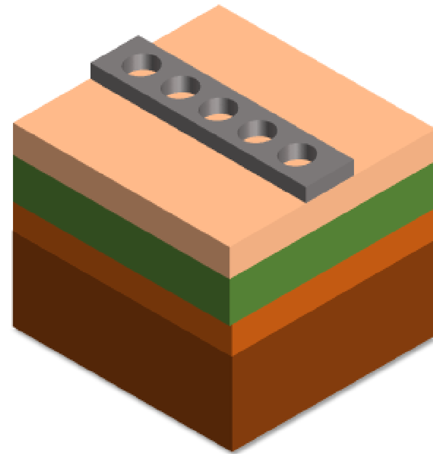

(b) Writing and developing the pattern

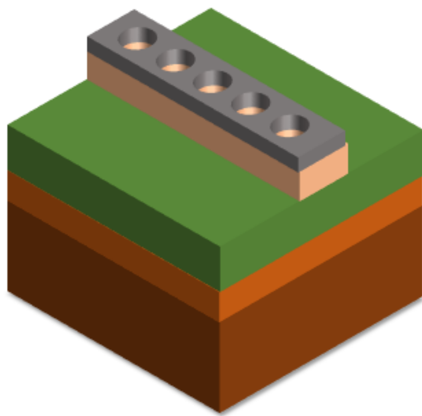

(c) Dry etch of the GaP substrate

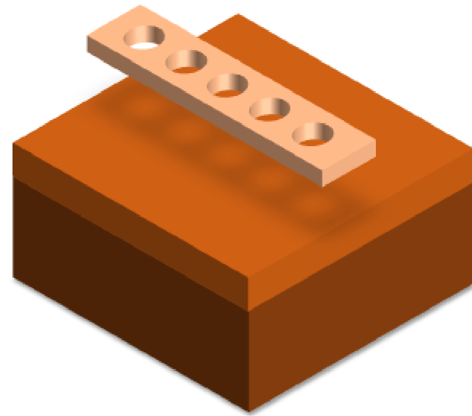

(d) Removal of $Al_{0.91}GaP_{0.09}$ sacrificial layer

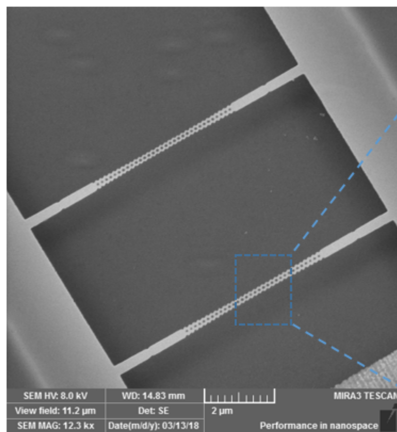

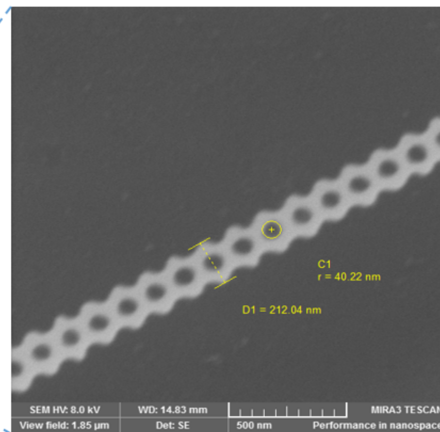

(e) SEM image of the suspended GaP nanobeam cavity taken at a stage tilt of 70º

Figure 2.13: Fabrication steps of the GaP nanobeam cavity using HSQ negative resist.

The exposed silica mask pattern is transferred into the GaP via Cl-based inductively coupled plasma reactive ion etching (ICP-RIE, Oxford Instruments) [49]. The etching process was done at microelectronics research center (MRC) at the University of Texas since the Cl_2 gas is not provided locally at TAMU for safety reasons. The details of this process are shown in table 2.2. This recipe is mostly based on the previous work for the bulk GaP [49]. We note that the etch rate reported here are not constant due to fluctuations in DC self-bias voltage which controls the ion energy. Following the etching, the sacrificial layer ($Al_{0.91}GaP_{0.09}$) is removed by a hydrofluoric (HF) acid wet etch. The concentration of HF is reduced to 1% to slow down the undercutting procedure. The etch rate of the sacrificial layer is 0.1 micron/second. It is recommended to lower the HF concentration for high Al content to control the undercutting procedure. Lastly, The undercut device is immersed in water for 1 minute to clean some metallic residues.

H_2 flow	14.5 sccm
CH_4 flow	5 sccm
Cl_2 flow	10 sccm
BCl_3 flow	10 sccm
RF power	120 W
DC bias	70 V
ICP power	200 W
Chamber pressure	5 mTorr
Temperature	20°C
Etch rate	1.75 nm/s
selectivity (GaP:HSQ)	5:1

Table 2.2: Dry etching recipe for GaP.

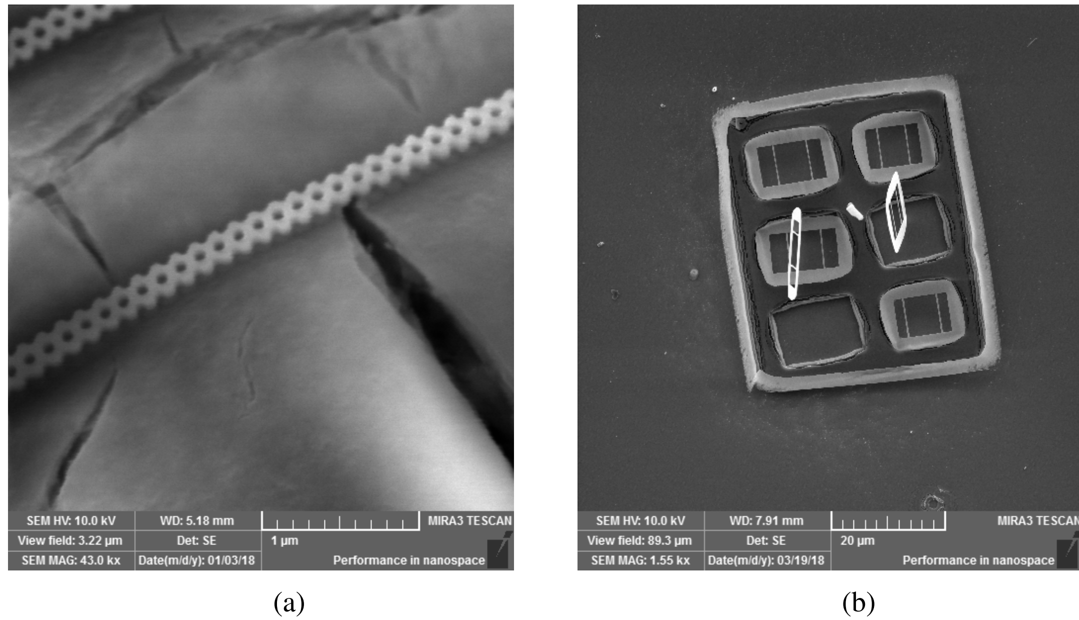

(a) (b)

Figure 2.14: (a) The corrosion of the intermediate layer $Al_{0.91}GaP_{0.09}$ after a Cl_2 based dry etch. (b) Suspended GaP membranes one week following the undercutting procedure.

The main challenge here is the removal of the sacrificial layer $Al_{0.91}GaP_{0.09}$. We often observe some cracks and fractures after the etching process, see Fig. 2.14 (a). This may not be evident immediately after doing the dry etch, as it takes sometimes one or two days to appear. Because of that, the undercutting procedure should be done soon after the etching process and before the the sacrificial layer starts to corrode.

Following the undercutting step, we observe that the stability of the suspended membranes degrades over time. A few days after the undercutting procedure, most of the membrane found already detached from the surface, see Fig. 2.14 (b). The collaborator in nanoFab, University of Alberta, suggested that might due to the corrosion of the aluminum element in the sacrificial layer. In particular, The interaction between Cl_2 and Al yields $AlCl_3$ as a volatile product causing the sacrificial layer to corrode. To mitigate such issue, the $AlCl_3$ can be removed by running an additional dry etching recipe that contains a mixture of O_2 and CHF_4 immediately after the undercutting procedure.

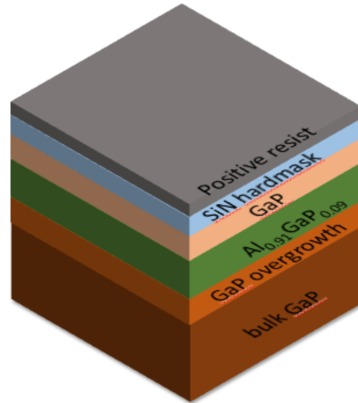

(a) Spin coating PMMA

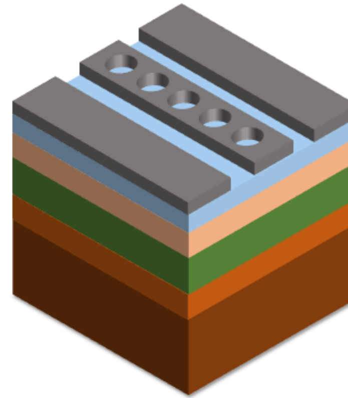

(b) Writing and developing the pattern

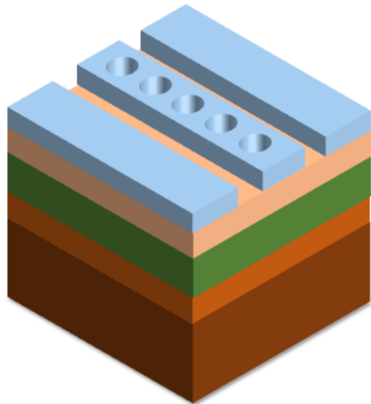

(c) Rry etch of the Si_3N_4 hard mask

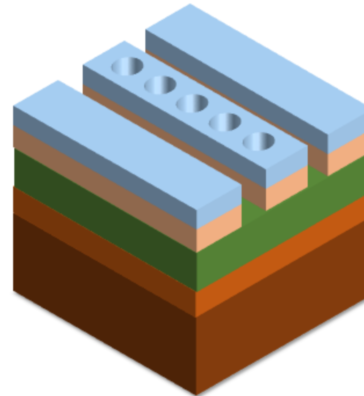

(d) Dry etch of GaP

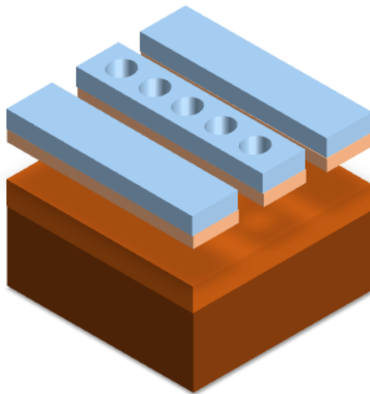

(e) Removal of $Al_{0.91}GaP_{0.09}$ sacrificial layer

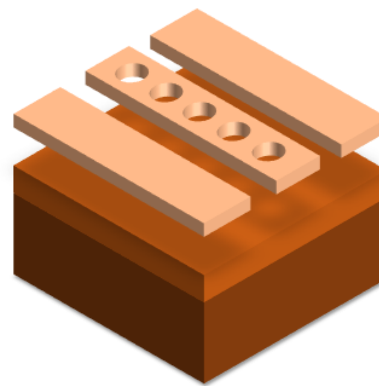

(f) Removal of Si_3N_4 hard mask

Figure 2.15: Fabrication steps of the GaP nanobeam cavity using PMMA positive resist.

The environmental stability of HSQ resist is another challenge, which adds more complexity and restrictions on the lithography process [50, 51]. In addition to the resist stability, the shelf life is too short compared to conventional positive resists such as polymethyl methacrylate (PMMA) and ZEP520. More importantly, the GaP chip cannot be used again after the dry etch since the negative resist covers only the area in which the structures are written. Therefore, it is necessary to find another fabrication method that is more convenient and less time consuming.

Now, we will discuss another method that uses polymethyl methacrylate (PMMA) positive resist together with Si_3N_4 hard mask instead of HSQ. PMMA is most common resist used for EBL process, which is very well-known for its stability and low cost. The fabrication steps are depicted in Fig. 2.15. In general, thin resists are recommended for writing small features that require high resolution. Therefore, we chose 950 PMMA A2 in Anisole instead of other thicker resists. Since PMMA has a poor resistance to the dry etch, a thin layer of Si_3N_4 (thickness ~ 50 nm) was grown on top of the GaP surface as a hard mask. First, the resist is spin coated on top of the hard mask at 3000 rpm for 40 seconds, which yields a thickness of around 90 nm. Then, prebaking was performed on a hotplate at 180°C for 90 seconds. After writing the pattern via the same EBL equipment mentioned above, the unexposed resist remains and the exposed resist is removed in Methyl isobutyl ketone (MIBK) developer mixed with Isopropyl solution 1:3. Following the EBL process, the pattern is transferred to the Si_3N_4 hard mask via ICP-RIE, Oxford Instruments. The recipe details are explained in table 2.3. Then, the pattern is transferred to the GaP substrate in the same way as described above for the HSQ negative resist. Interestingly, the selectivity of GaP with respect to Si_3N_4 hard mask is found similar to the HSQ resist ($\sim$ 5:1). Finally, the hard mask should be removed after running the last subsequent etching process. We note that this work explains for the first time a robust and convenient method to fabricate suspended GaP photonics devices based on PMMA resist. The common resist for GaP devices is ZEP520A which has strong resistance in the dry etching process [52]. However, the cost of the ZEP520A resist is far expensive compared to the cost of PMMA resist. .

CHF$_4$ flow	50 sccm
RF power	200 W
DC bias	330 V
ICP power	0 W
Chamber pressure	20 mTorr
Temperature	18°C
Etch rate	0.55 nm/s
selectivity (Si_3N_4:PMMA)	4:5

Table 2.3: Dry etching recipe for Si_3N_4 hard mask.

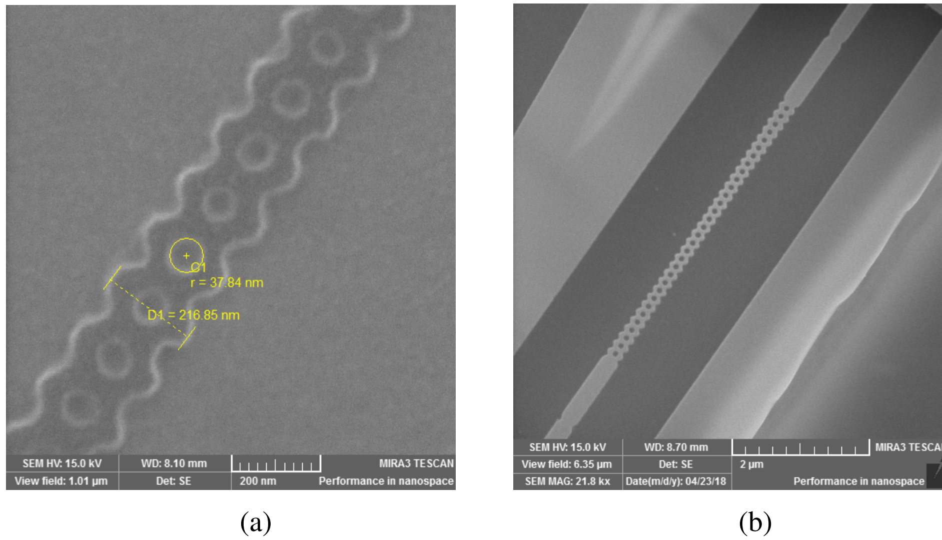

(a) (b)

Figure 2.16: (a) SEM image of Si_3N_4 hard mask after CHF$_4$ dry etch. (b) SEM image of suspended GaP membranes following the undercutting procedure.

2.6 Conclusion

In this chapter, we have illustrated a compact design for nanobeam cavities with an ultrahigh Q/V value for the purpose of strong coupling between the cavity mode and a single GeV center. Our design is based on the quadratic tapering method to obtain the Gaussian-like field profile for the cavity resonance. The cavity footprint is reduced thanks to the idea of semicircular holes, which we have introduced to enhance the mirror strength of the cavity. Therefore, the cavity footprint of the original structure was reduced by nearly 50%. On the other hand, the fabrication procedure of

suspended GaP nanobeam cavities was also investigated and explained in this work. In general, the challenges and problems related to the GaP fabrication have been addressed. We have made a new fabrication method is based on using Si_3N_4 hard mask, which saves money and time compared to other conventional methods explained in this chapter. However, we were not able to characterize and measure the fabricated GaP nanobeam devices due to instability issues and the lack of tools and equipment. On the other hand, we have also provided detailed analysis of the cavity QED for different DNC sizes embedding single GeV center. Our results reveal a high cooperativity that reaches up to five orders of magnitude, for the first time, in the strong-coupling regime. This work will facilitate the design of ultrahigh Q/V photonic devices, and thus support integrated photonic structures used in a broad range of quantum networks.

3. SILICON NITRIDE NANOBEAM CAVITIES

3.1 Introduction

The recent progress in quantum optics has increased the demands for an ideal material that posses excellent optical properties and high quality at a low cost. The properties of the most common materials for integrated photonic crystal nanobeam cavities are shown in Table 3.1. Among these, GaP offers several advantages over the other materials mainly due to its high refractive index (n $\sim$ 3.3) and good quality. The wide optical transparency window allows GaP to be applicable in quantum information systems involving diamond color centers [41]. As mentioned in Chapter 2, the fabrication processes of integrated photonic devices on GaP chip are still challenging and the material growth requires advanced tools and equipment.

Alternatively, diamond has been recently emerging as a potential platform for quantum information application[53]. The growth of noncrystalline diamond suffers from substantial propagation losses due to its high scattering and absorption losses. This limits the ability to fabricate diamond photonic devices on noncrystalline diamond thin films. However, several groups have already designed and fabricated diamond photonic devices on bulk diamond single-crystal substrates via focused ion beam (FIB) [54] or EBL followed by an angled dry etch [55]. Nonetheless, the design and fabrication based on these methods are still challenging and not compatible with standard fabrication technology.

Silicon nitride has received increasing attention thanks to the compatibility of the manufacturing process with standard CMOS fabrication. Furthermore, Si_3N_4 photonic circuits are fully bio-compatible, opening new possibilities for of bio-photonic applications. The optical properties of Si_3N_4 feature a large band gap and wide optical transparency window spanning from the ultraviolet to near-infrared spectral region. Microdesks resonator fabricated in Si_3N_4 chips have ultrahigh quality factor, up to 17×10^6 [56], and have been extensively used in non-linear optics [57] and cavity optomechanics [58].

Material	Optical window (μm)	Refractive index (n)	Bandgap energy (eV)
Si_3N_4	0.3 - 5.5	2	5
Si	1.1 - 6.1	3.4	1.1
SiO_2	0.38 - 2.2	1.5	9
SiC	0.2 - 5	2.6	2.4
Diamond	0.22 - 20	2.4	5.5
GaP	0.54 - 10	3.3	2.2
GaN	0.36 - 7	2.4	3.4
GaAs	0.9 - 17.3	3.7	1.42
TiO_2	0.42 - 4	2.5	3.5

Table 3.1: Optical constants of Si_3N_4 and alternative materials. For more details, see ref. [59].

Photonic crystal slabs have many advantages over microdesk resonators due to their low mode volume and large separation between high order modes. Because of the relatively low refractive index, the 2D-photonic bandgap of Si_3N_4 photonic crystal slabs is narrow. This makes the design of high Q/V cavities in 2D-photonic crystals unattainable. The cavity quality factors demonstrated so far for 2D-photonic crystals cavities were quite modest ($10^3 - 5 \times 10^3$) [60, 61].

With inspirations from the GaP nanobeam design, we have extended the design with semicircular holes to nanobeam cavities based on Si_3N_4 material. Since the design have been thoroughly investigated and explained in Chapter 1, we focus mostly on fabrications and characterizations throughout this chapter. We note that there are many designs of Si_3N_4 nanobeam cavities, some of which have been used in various fields including cavity optomechanics [26, 62], quantum networks [39, 63, 64].

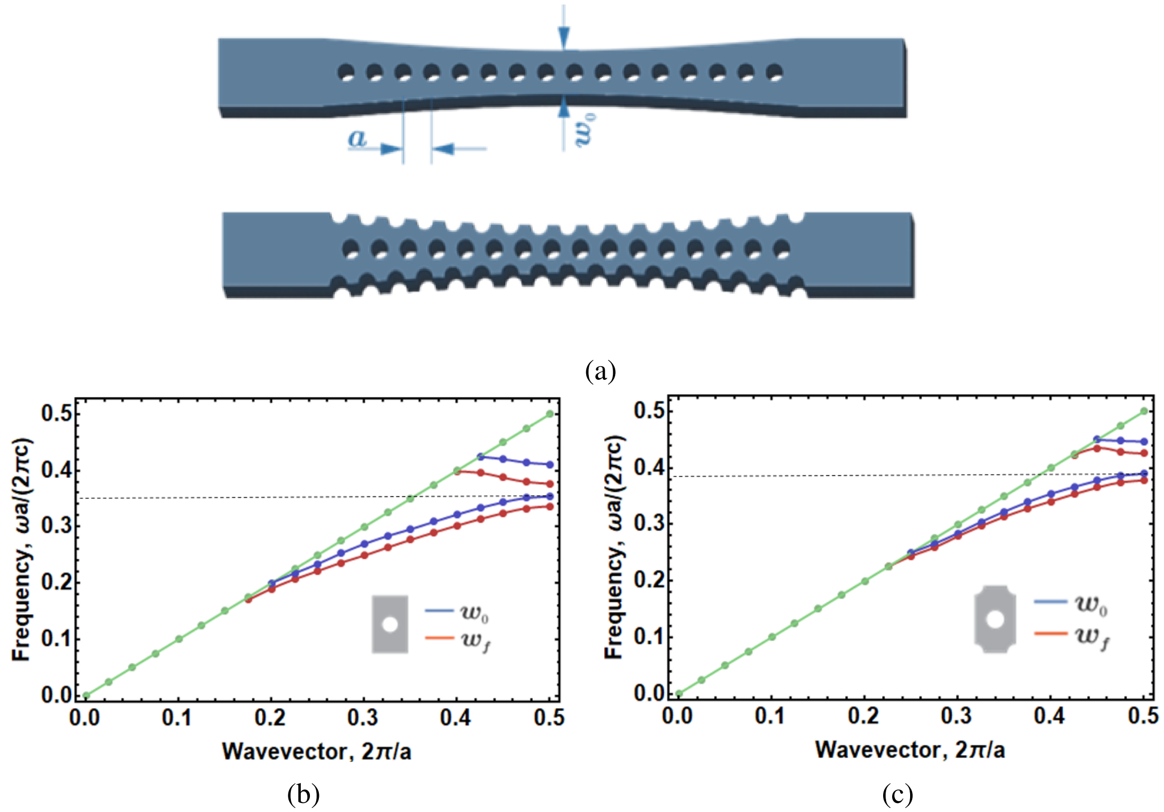

Figure 3.1: (a) Sketch of Si_3N_4 nanobeam cavity for the central holes design (top) and for semicircular holes (bottom). (b) & (c) The corresponding TE band structure calculated by FDTD simulations. The dashed line marks the resonant frequency. The thickness for the central holes design is d/a = 0.9, and for semicircular holes is d/a = 0.85.

The design of Si_3N_4 nanobeam cavities is based on the quadratic tapering method which generates a Gaussian-like field profile inside the cavity, as discussed thoroughly in Chapter 1. In this chapter, we consider two designs depicted in Fig.3.1 (a). The most useful plot of any photonic crystals is the band structure which gives a general idea about the designed device. The band structure corresponding to each design is shown in Fig. 3.1 (b) and (c). Since the refractive index of Si_3N_4 is relatively low (n = 2), the cavity resonance naturally shifts to higher frequencies towards the light line. Introducing semicircular holes shifts the resonant frequency even higher. The most important

implication of this shift is that it would essentially increase the probability of the coupling between the resonant mode and the radiated mode in air, leading to a huge radiative loss. Therefore, we expect the radiative loss, which is characterized by Q_r to be much less than Q_r calculated for GaP nanobeam cavities. By comparing the bandgap of each design, it can be seen that semicircular holes design has a broader bandgap than the first design. This gain in the band gap size indicates better mode confinement and higher cavity quality factor. In contrast, the bandgap of 2D-photonic crystals Si_3N_4 is much narrower than 1D structure due to the additional dimension in the Brillouin zone [65].

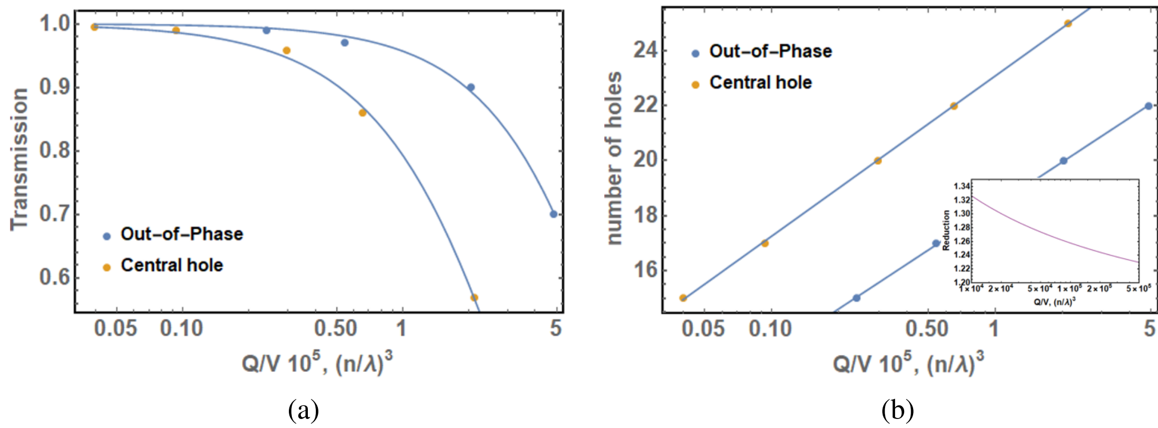

Figure 3.2: (a) Transmission dependence on Q/V value for the central holes design and the semicircular holes design. The initial width is $W_i/a = 1.5$, and the final width is $W_f/a = 2$. (b) Number of holes dependence on Q/V value for both designs. (inset) Reduction factor in number of holes as a function of Q/V value gained by adding the semicircular holes.

The width of the nanobeam cavity was optimized by examining the band structure for different nanobeam widths. Because of the low index of refraction, the difference between the initial and final width in this case has to be larger than that in GaP films. Otherwise, the bandgap size would be very small and the cavity resonance would leak fast to the surrounding air. On the other hand, increasing the contrast between the initial and final width suppresses the cavity transmission as a result of the non-adiabatic tapering profile, as proven in Chapter 2 (Fig.2.6). Examining the band

structure for different nanobeam widths, we found that $W_{\mathrm{i}}/a = 1.5$ and $W_{\mathrm{f}} = 2$ is the optimal width. Here, the choice of the nanobeam width is somewhat more flexible than GaP.

A comparison between cavity transmission dependence and the Q/V value in both designs is shown in Fig.3.3b (a). It is clear that the cavity Q/V for the semicircular holes design surpasses the other design because of the increase in the corresponding bandgap. In fact, the simulation results reveals that the quality factor limited by the the radiation loss Q_r has increased by almost one order of magnitude for the first design. The exact Q_r value for the semicircular holes design and for the second design is 7×10^6 and 6×10^5, respectively. However, Q_r for GaP nanobeam cavities has similar value in both designs though the band gap has increased for the first design. We note that the MeeP simulations may not be precise enough to make distinction between two closed ultrahigh Q/V values.

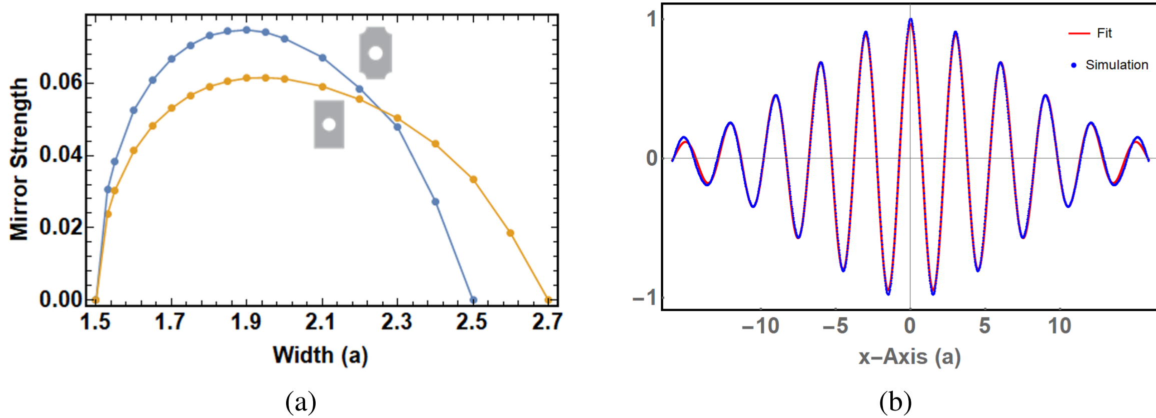

Figure 3.3: (a) Mirror strength as a function of nanobeam final width for two configurations: only central holes (orange) and out-of-phase semicircular holes (blue). (b) E_{y} field distribution for the TE fundamental mode of the central hole design obtained from FDTD simulations (blue dots) and from an analytic formula (red line): $E_{\mathrm{y}} = \cos\left((x - x_0)\frac{\pi}{a}\right)\exp\left(-\sigma^2(x - x_0)\right)$.

Because of the low index of refraction, it might seem to be intuitive that the number of holes is required to obtain a high quality factors in the Si_3N_4 material is larger than in GaP. However, one has to keep in mind that the Q_r in this case is lower that in GaP nanobeam cavities by at least 2 order of magnitude. Therefore, the maximum number of holes one can add would correspond

to that when Q_{tot} reaches the same order of magnitude as Q_r, or equivalently, when the cavity transmission drops below 70%. Figure 3.2 (b) shows the number of holes and Q/V dependence. It can be seen that the maximum number of holes in Si_3N_4 nanobeam cavities and GaP nanobeam cavities is approximately similar though each design has a different maximum number of holes. The reduction in the cavity footprint is ~ 1.25, which is lower than that for GaP nanobeam cavities. This can be explained by the mirror strength corresponding to both designs, see Fig.3.3 (a). The difference between the mirror strength of each design is quite small compared to GaP nanobeam cavities due to the decrease in the overall mirror strength. Nevertheless, the fundamental mode of Si_3N_4 nanobeam cavities has a Gaussian-like field profile. Fig.3.3 (b) shows E_y field distribution across the cavity axis is fitted with a Gaussian function. Such profile is necessary for cavities with ultrahigh quality factor, as explained in chapter 2.

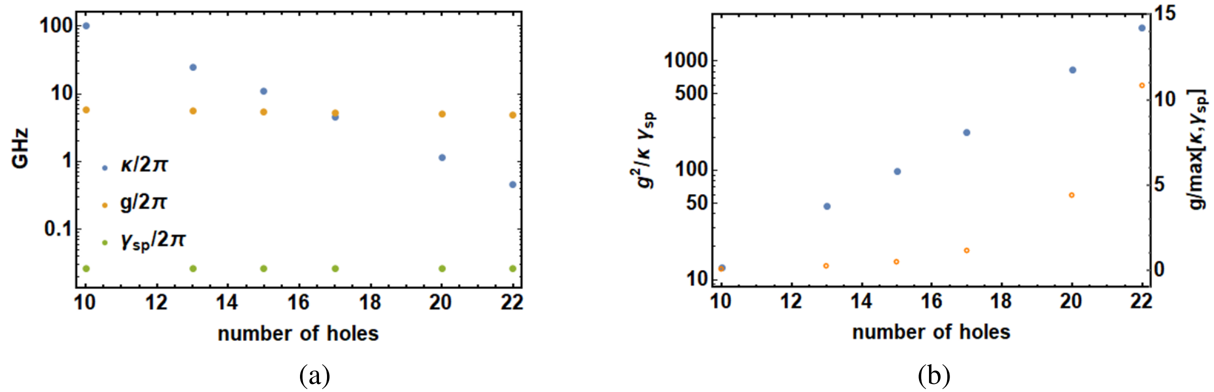

(a) (b)

Figure 3.4: (a) Relevant cavity QED rates as a function of number of holes for Si_3N_4 nanobeam cavities. $\kappa/2\pi$ is the cavity decay rate, $\gamma_{sp}/2\pi$ is the atomic decay rate of the GeV center, and $g/2\pi$ is the single photon coupling rate. (b) Cooperativity (dots) and weak/strong coupling index (open circles) as a function of number of holes. Results shown in (a) and (b) are related to the semicircular holes design.

3.3 Cavity QED analysis

Since the quality factor of Si_3N_4 nanobeam cavities could reach to a high limit ($\sim 10^6$), we can consider a scheme where a single DNC embedding GeV center is placed on top of the cavity

surface, as we did with GaP nanobeam cavities in Chapter 2. Using FDTD simulations, we found that the ratio of the maximum energy density in the nanobeam cavity to the maximum energy density at the DNC position (α^2) has decreased by a factor of 1.7 compared to the GaP case. Cavity QED figures of merit are plotted in Fig. 3.5. As before, the cavity field decay rate κ is the only parameter that depends heavily on the number of holes. By stretching the cavity footprint, the cavity field decay rate can be suppressed below the vacuum Rabi frequency g, allowing the atom-photon interaction to be in the strong coupling regime. This condition is satisfied for nanobeam cavities with at least 17 holes in each side of the cavity, which corresponds to Q/V of 5×10^4. The cooperativity in this regime ranges from 10^2 up to 10^3, as shown in Fig. 3.5 (b). Though the strong coupling regime seems to be challenging with Si_3N_4 nanobeam cavities, some applications such as quantum information processing and quantum repeaters can operate efficiently even if the atom-light interaction lies in the weak coupling regime [66, 67].

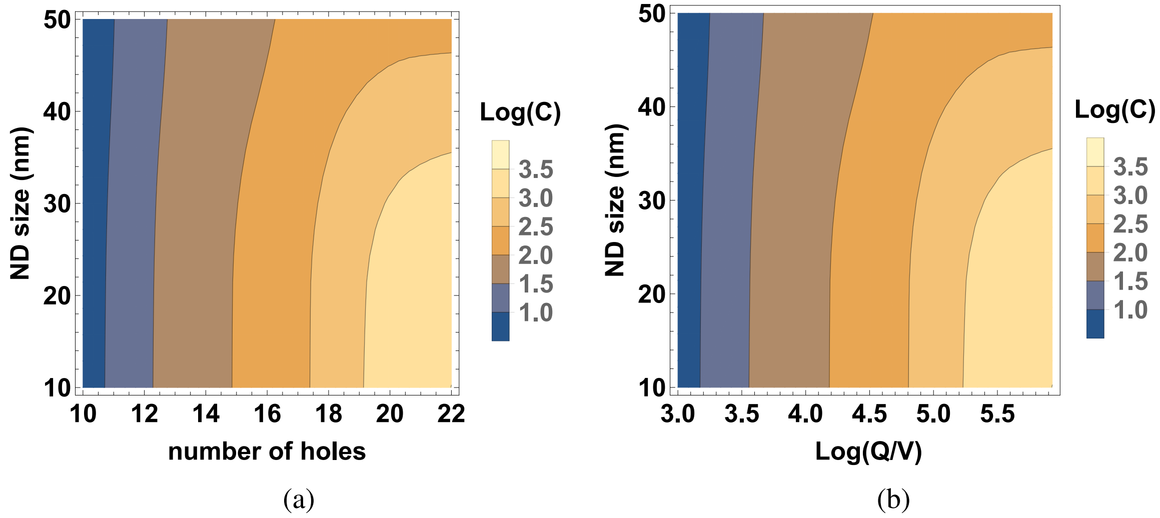

(a) (b)

Figure 3.5: (a) & (b) Cooperativity as a function of number of holes and cavity Q/V value for different DNC sizes placed on top of Si_3N_4 nanobeam cavity, respectively.

Figure 3.5 shows the cooperativity for different DNC sizes. The impact of the large DNC on the cavity Q/V value has caused the cooperativity to drop at least by one order of multitude for

high Q/V cavities. On the contrary, DNCs with sizes > 30 nm have a negligible effect on the cavity Q/V value, in agreement with the previous results of GaP cavities. We note that all Cavity QED calculations have been performed particularly on semicircular holes design. Nevertheless, we expect the results of the second design to be qualitatively consistent with the first design, since these two designs have close Q/V values.

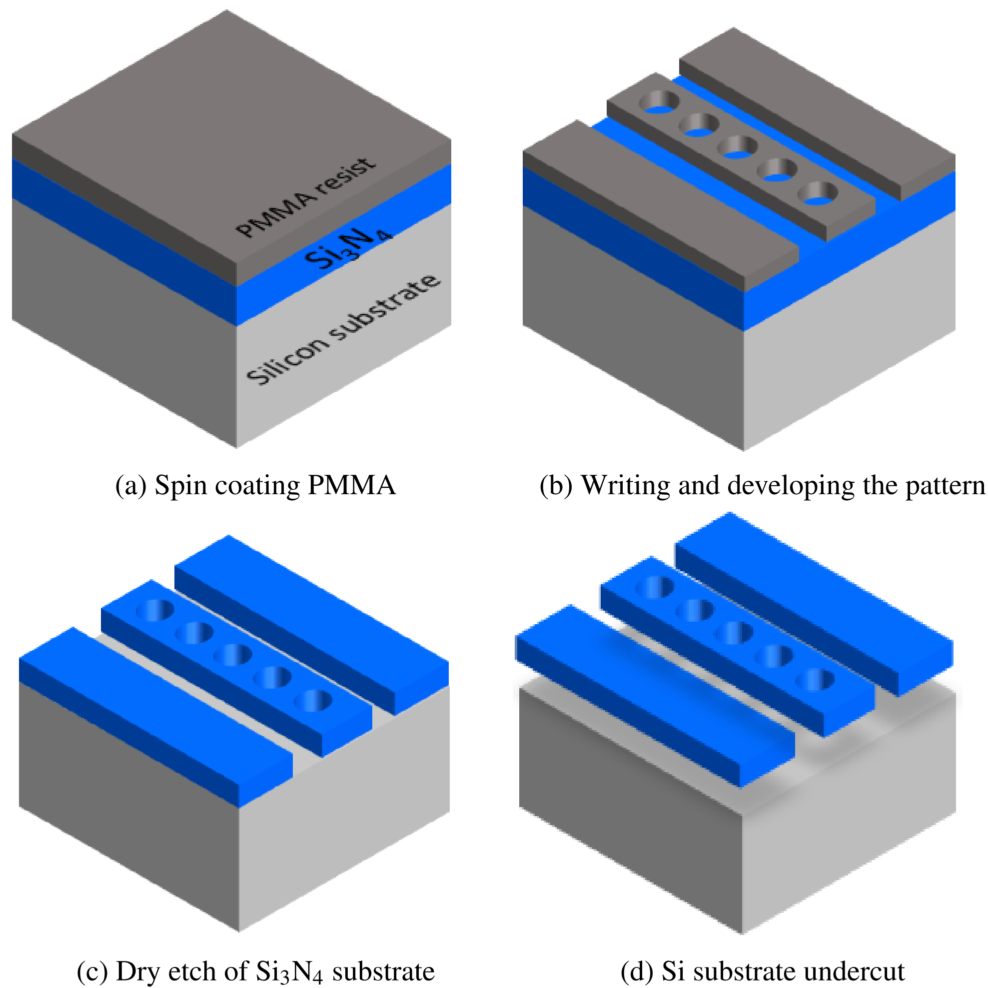

(a) Spin coating PMMA

(b) Writing and developing the pattern

(c) Dry etch of Si_3N_4 substrate

(d) Si substrate undercut

Figure 3.6: Fabrication steps of Si_3N_4 nanobeam cavities.

3.4 Fabrication of Si_3N_4 nanobeam cavities

In this section, we explain the fabrication procedure for Si_3N_4 nanobeam cavities suspended in air. Initial devices were fabricated locally from Si wafers with 180 nm thick Si_3N_4 layer gown by plasma enhanced chemical vapor deposition (PECVD), Oxford Plasmalab tool. In general, PECVD method is based on creating plasma from Silane (SiH_4) and ammonia (NH_3) molecules by using two parallel plates and radio frequency [68]. This method allows to grow silicon nitride at a relatively low temperature (< 400°C). However, PECVD nitride suffers from a high hydrogen impurities density in the form of N-H and Si-H bonds. These impurities act as absorption centers responsible for the propagation losses at visible and telecommunications wavelengths [69]. However, a subsequent thermal annealing at a high temperature might eliminate or perhaps lower the hydrogen impurities density, and therefore improves the properties of Si_3N_4 film to a great extent [70, 71].

The other deposition technique used to deposit the silicon nitride films is low pressure chemical vapor deposition (LPCVD). These films are deposited by the gas phase chemical reaction of dichlorosilane (SiH_2Cl_2) and ammonia (NH_3) at a high temperature (> 700°C) [72, 73]. The first advantage is that the hydrogen concentration for LPCVD nitride films is too low ($\sim$ 3%) compared to the PECVD films ($\sim$ 40%) [74]. The low hydrogen concentration is very crucial for enhancing the film quality and reducing optical losses. This can be verified by measuring two similar devices grown differently, as we will show in the next section. Another advantage of LPCVD film is that it has higher intrinsic stress and therefore is more robust and resistance to KOH etching. Our LPCVD nitride films were bought commercially from Rogue Valley Microdevices. This film has $\sim$800 MPa Tensile Stress, compared to $\sim$250 MPa Tensile Stress for PECVD nitride films. Nevertheless, we were able to fabricate structures from PECVD nitride films and release the suspended cavities without the use of any critical point drying.

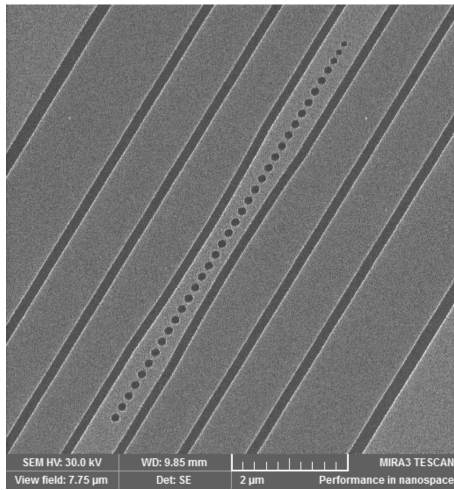

(a)

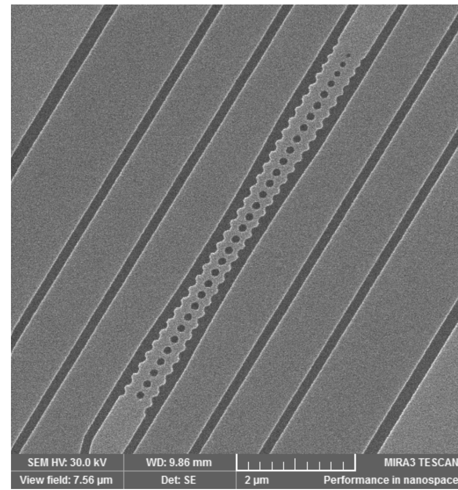

(b)

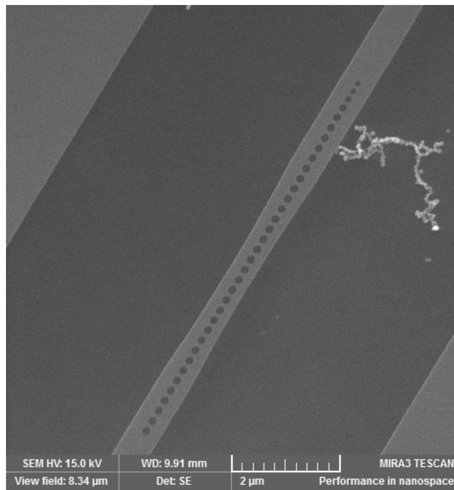

(c)

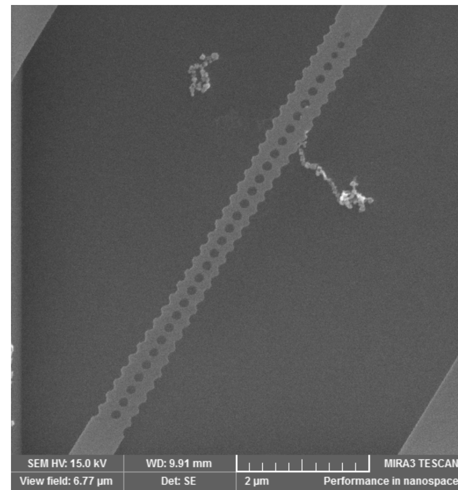

(d)

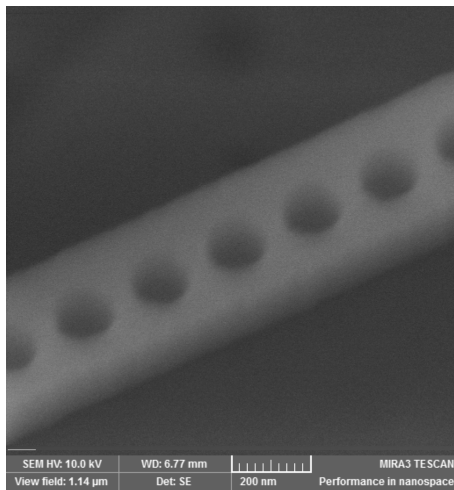

(e)

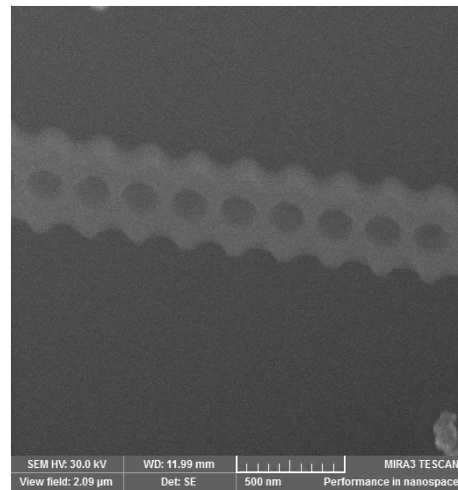

(f)

Figure 3.7: (a) & (b) SEM image of two different designs explained in the text of Si_3N_4 nanobeam cavities after the dry etch. (c) & (d) SEM image of the same devices after the undercutting procedure of the underlying Si layer. (e) & (f) high resolution SEM images of the same devices taken at a 35° stage tilt.

Fabrication of the Si_3N_4 nanobeam cavities follows a similar process flow as the GaP devices in the previous chapter. As shown in Fig. 3.7, 950 PMMA A4 resist in Anisole was spin coated on top of the nitride layer at 3000 rpm for 40 seconds, which yields a thickness of $\sim$240 nm. Then, prebaking was performed on a hotplate at 180 °C for 90 seconds. Though the thinner resist (950 PMMA A2) provides higher resolution, it cannot withstand until the end of the dry etching process. After writing the pattern via the same EBL equipment used for GaP devices, the unexposed resist remains and the exposed resist is removed in Methyl isobutyl ketone (MIBK) developer mixed with Isopropyl solution 1:3. Following the EBL process, the pattern is transferred to the Si_3N_4 via dry etching (ICP-RIE, Oxford Instruments). The etching recipe is provided in Chapter 2 (table **??**). After stripping the resist in acetone, 30% KOH solution was used to etch the exposed silicon at 100 °C for 10 minutes. Potassium hydroxide (KOH) is known to etch silicon preferentially in the (100) plane resulting in an anisotropic etch, with sidewalls that form $\sim 55°$ angle with surface [75]. The etch rate for Si layer is $\sim$ 0.5 nm per minute. Optimizations for the fabrication process are mentioned in the appendix B. Figure 3.7 shows SEM images at different stages of the fabrication process.

Because of PMMA inferior performance in the dry etching process, we also have tried CSAR 62 positive resist (AR-P 6200.09, allresist) that offers better etching resistance. First, CSAR 62 resist was spin coated on top of the substrate at 4000 rpm for 60 seconds, which yields a thickness of $\sim$ 200 nm. Then, prebaking was performed on a hotplate at 150 °C for 60 seconds. After writing the pattern via the same EBL system mentioned above, the unexposed resist remains and the exposed resist is removed in amyl acetate developer. The sensitivity of CSAR 62 resist is much higher than that of PMMA, and as a result, the exposure dose optimization is quite challenging. The rest of the fabrication process follows the same procedure as in PMMA resist. The major issue in CSAR 62 resist is the corresponding edge roughness. Figure 3.8 shows a comparison between two devices fabricated from CSAR 62 resist and PMMA resist. SEM images show that the overall roughness of the latter devices has enhanced drastically. This is confirmed by calculating the corresponding standard deviation for nanobeam holes (Fig.3.8).

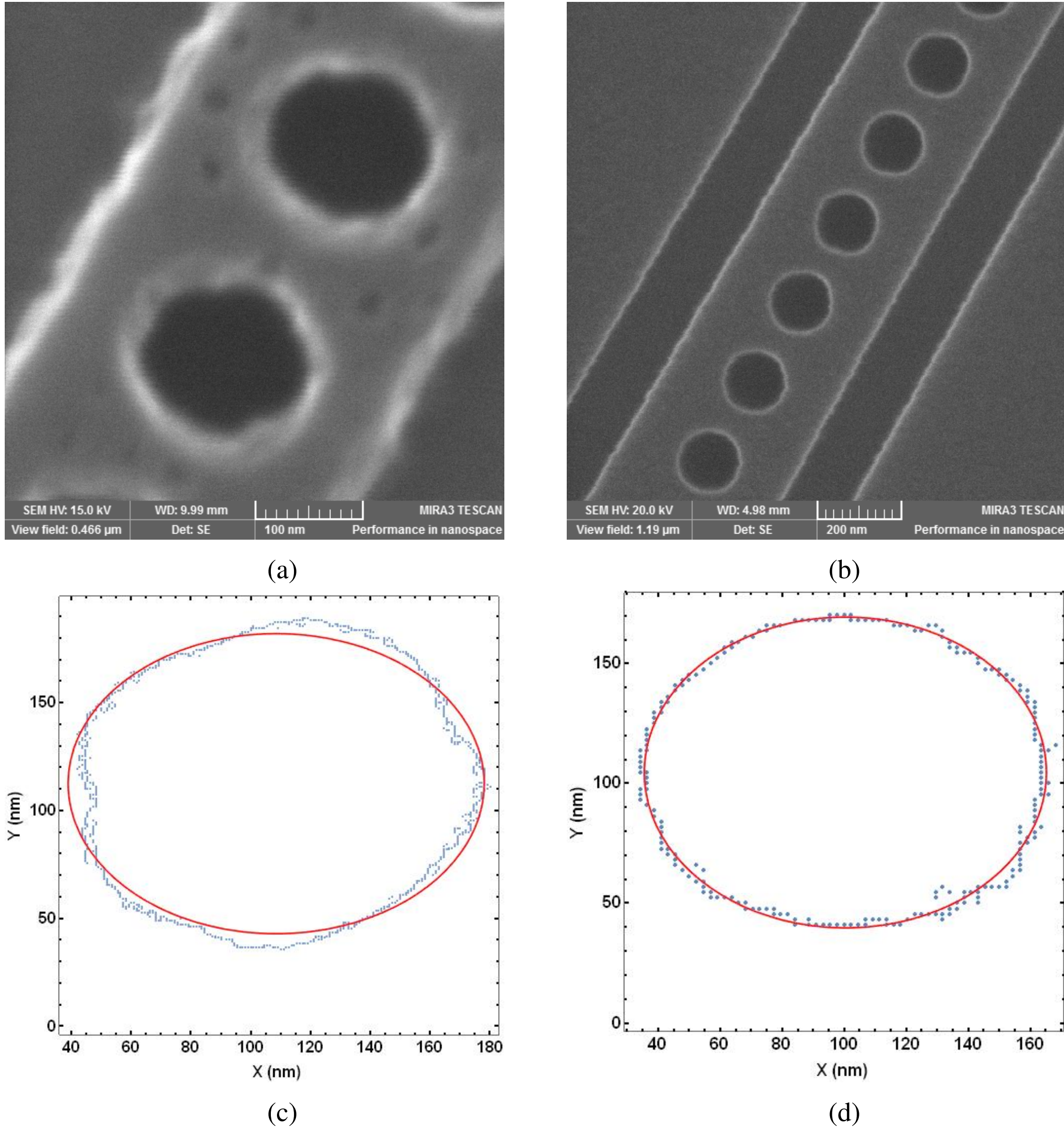

Figure 3.8: (a) & (b) High resolution SEM images of the device fabricated from CSAR 62 resist and 950 PMMA A4 resist, respectively. (c) & (d) Hole profiles extracted with a Gaussian filter to measure the hole roughness for CSAR 62 resist and 950 PMMA A4 resist, respectively. The corresponding standard deviation is σ = 22 nm and σ = 14 nm. The dark spots appear in (a) refer to CSAR 62 resist residues left after the dry etching process and cannot be removed by a resist remover or O_2 plasma ashing.

The width-edge roughness is also calculated. The corresponding corresponding standard deviation is σ = 5.5 nm and σ = 1.6 nm for CSAR 62 resist and PMMA resist, respectively. We note that the standard deviation for nanobeam holes is much higher than that for nanobeam width

mainly because of less number of points per area.

Another problem in CSAR 62 resist is the development process which has to be done in a low temperature condition in order to achieve better edge roughness, similar to development process for ZEP-520A resist [76]. In addition, CSAR 62 resist is hard to remove with the specified remover (AR 600-71) and even with O_2 plasma ashing. Nevertheless, piranha cleaning or O_2 plasma cleaning with inductively coupled plasma (ICP) might be useful for cleaning the surface from any polymer residues. We note that preforming O_2 plasma cleaning with the ICP power is detrimental to nano-structures in most cases especially if the ICP power is high (> 200 W).

3.5 Characterization and quality factor measurement

In order to characterize the cavity resonances around the ZPL transition of GeV center, light from a supercontinuum laser source (SuperK EVo, NKT Photonics) was coupled into the Si_3N_4 nanobeam cavity via an optical fiber tip, then the reflection spectra were collected and sent to a commercial spectrometer (SP-2150, Princeton instruments). Thee experimental setup is shown in Fig.3.9 (a). The coupling efficiency between the cavity and the optical fiber tip is addressed in the chapter 4.

Figure 3.9 (c) shows the reflection spectrum collected from Si_3N_4 nanobeam cavity which has 20 central holes in each side. quality factors > 3000 were routinely observe for devices fabricated from LPCVD nitride films. The best device we characterized shows a total quality factor of $\sim$ 9,300, which is limited by the resolution of the spectrometer. The quality factor calculated in FDTD simulations for this specific design is $Q_{total} \sim 20,000$. After measuring multiple cavities, we found that almost 1/3 of the fabricated devices possess a quality factors of $\sim$ 9,000, which is quite common in photonic devices characterization due to the fabrication imperfections [77, 78]. On the other hand, the separation between the fundamental and high order modes is $\sim$ 10 nm in most devices. It is worth noting that the separation between modes depends heavily on the number of holes in the cavity, and it becomes wider as we shrink the cavity footprint, which is the advantage of the semicircular holes design.

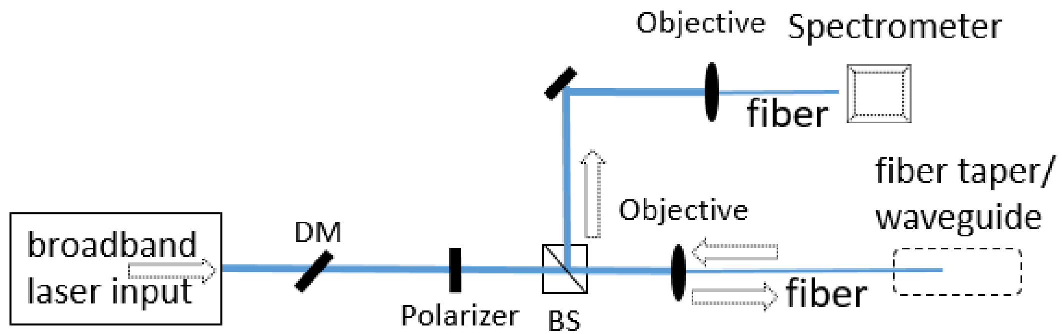

(a)

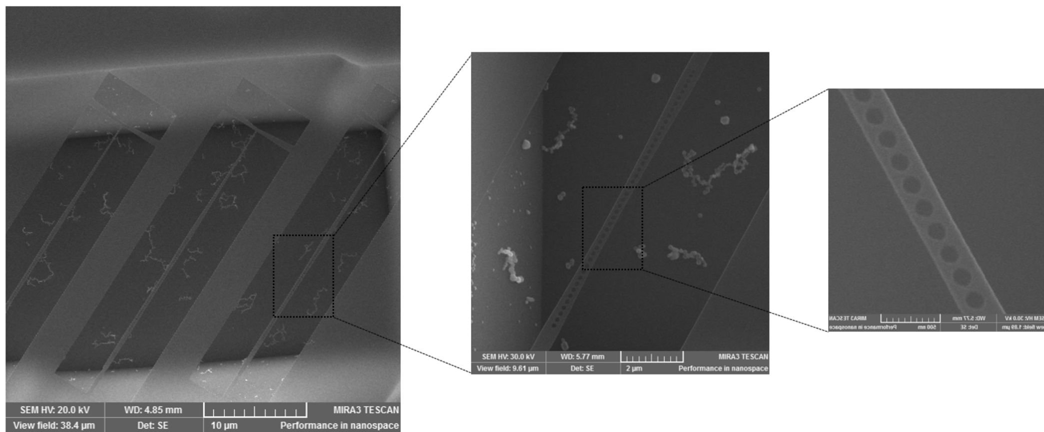

(b)

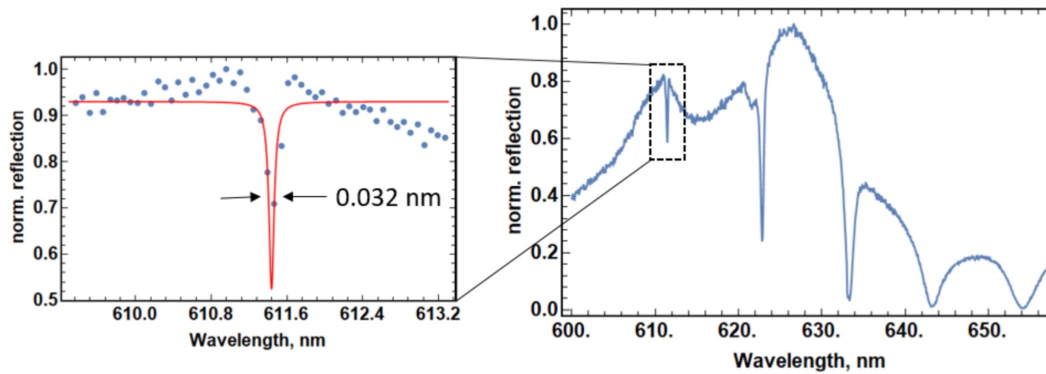

(c)

Figure 3.9: (a) Schematic of the optical characterization of Si_3N_4 nanobeam cavities. DC and BS are the abbreviation of dichroic mirror (which is used as a band pass filter) and beam splitter, respectively. (b) SEM images of the typical device with a zoomed image of the nanobeam cavity with the central holes design. (c) Normalized reflection spectrum of the cavity TE modes centered at wavelength $\lambda = 630$ nm. The Lorentzian fit yields a total quality factor of $Q_{total} \sim 9{,}300$.

Similar measurement was also conducted for the semicircular holes design. Figure 3.10 (b) shows the corresponding reflection spectrum collected from Si_3N_4 nanobeam cavity with 16 holes in each side. we routinely observe quality factors > 3000 for devices, qualitatively similar to the cavities with central hole design. The maximum quality factor measured for devices with this design was $\sim$ 5,100, which is limited by the resolution of the spectrometer. However, the calculated quality factor was $\sim$ 7,000 for this design. We note that this simulated quality factor is lower than that in central holes design since this cavity includes only 10 holes in the nanobeam taper. The simulated cavity quality factor for the device with 15 holes is $\sim$ 20,000, which is equivalent to the central design with 20 holes.

Now, we compare the simulated and calculated quality factor for both designs. In principle, quality factor should be be limited by the simulated radiation loss characterized by Q_r ($> 10^6$ in Si_3N_4 nanobeam cavity). However, the real radiation loss is much higher than the simulated case due to the fabrication imperfections including imperfect shapes, edge/side-wall roughness, and material absorption. Figure 3.11 (b) shows a comparison between measured and calculated quality factors for different set of cavities. Devices with quality factor up to 2,000 show a good agreement between the simulation results and the experimental measurement.

Away from the quality factor measurement, the separation between the fundamental and high order modes has increased compared to the central hole design. Examining different devices with the same design, e.g. in the semicircular holes design, we found that the separation between the fundamental and high order modes are not constant and depends on the symmetry of the nanobeam cavity. Sometimes the symmetry can be broken when the central holes are not aligned exactly in the middle plane of the nanobeam as a result of the origin deflection of the electron beam writer.

Since optical fibers exhibit linear and circular birefringence as a result of the fiber core deformation and external stress applied on the fiber (such as twisting and bending) [79], we use a polarization controller to converts the polarization to the desired state. In our experiment, we initially used a 3-paddle polarization controller (FPC030, Thorlabs): one functions as a half-wave and two as a quarter-wave plate. However, the resulting bending loss of the fiber we used (S405-XP,

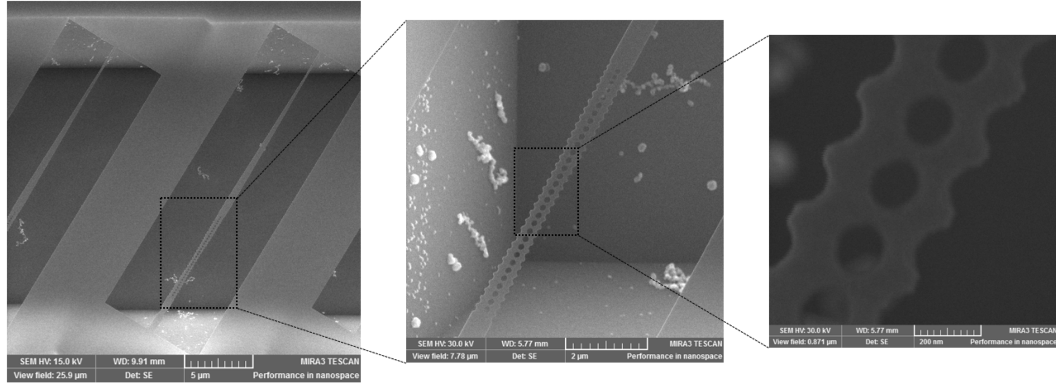

(a)

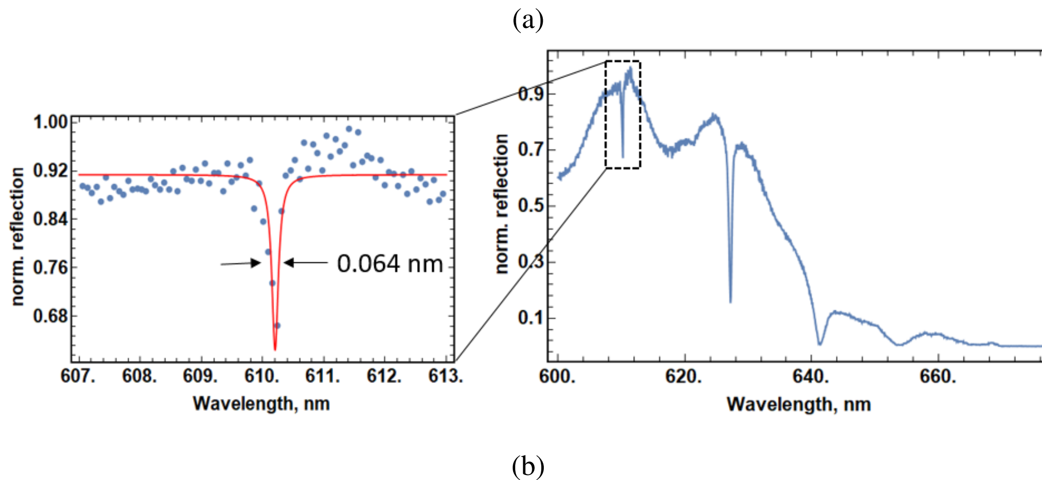

(b)

Figure 3.10: (a) SEM images of the typical device with a zoomed image of the nanobeam cavity with the semicircular holes design. The cavity includes 10 holes in the nanobeam taper, and 6 additional holes in the waveguide region. (b) Normalized reflection spectrum of the cavity TE modes centered at wavelength λ = 630 nm.v The Lorentzian fits yields a total quality factor of $Q_{total} \sim 5{,}100$.

Thorlabs) was huge so that the controller had very weak performance. In fact, the linear polarizer used for the laser beam controls the linear polarization very well despite the birefringence existing in the fiber. By changing the angle of the polarization, the spectrum around the cavity resonance can be optimized or suppressed, as shown in Fig.3.11 (a). However, the linear polarizer does not compensate for circular birefringence which affects the coupling efficiency to the waveguide mode but does not affect the collected spectrum.

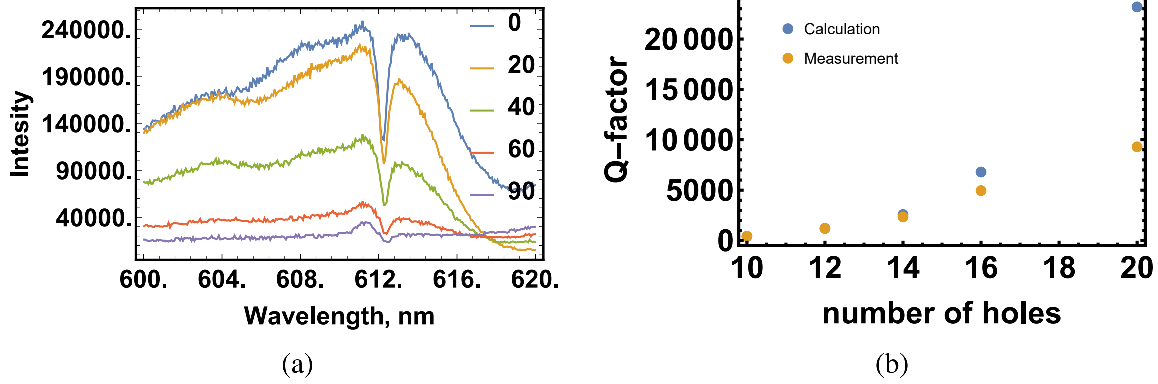

(a) (b)

Figure 3.11: (a) Cavity resonance taken at different input polarizations. The cavity was fabricated from a PECVD nitride film. (b) Comparison between the cavity quality factor obtained from the experimental measurement and numerical calculation as a function of number of holes.

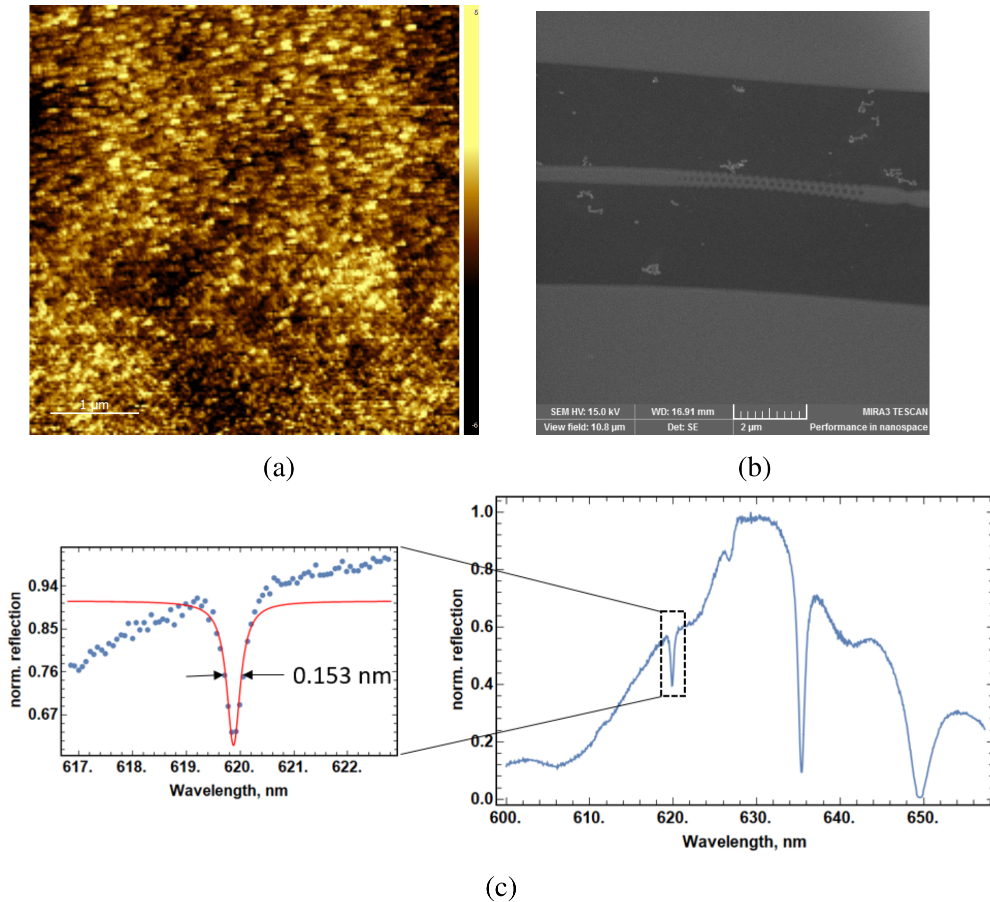

(a) (b)

(c)

Figure 3.12: (a) AFM scan of the top PECVD Si_3N_4 membrane. The corresponding root mean square is 2 nm. (b) SEM image of the cavity fabricated from PECVD film. (c) Normalized reflection spectrum of the cavity TE modes centered at wavelength $\lambda = 630$ nm. The Lorentzian fits yields a total quality factor of $Q_{total} \sim 2{,}000$.

As mentioned above, PECVD nitride films contain high hydrogen impurities, and therefore have a low tensile stress. SEM images of devices fabricated from PECVD always show structures bending and deflecting downwards, as displayed in Fig.3.12 (b). This indicates that the fabrication of long suspended devices would be challenging as the capillary force increases the pressure and affects the device stability [80]. The best nanobeam cavity fabricated from PECVD nitride possesses $Q_{total} \sim 2{,}000$ (Fig.3.12), limited by the scattering loss due to the material absorption. On the other hand, the scattering loss due surface roughness plays a minor role in our devices. The corresponding AFM scan reveals a smooth profile with RMS roughness of ~ 2 nm.

3.6 Conclusion

In summary, we have developed a design of a high Q/V nanobeam cavity based on silicon nitride material for the purpose of strong coupling between the cavity mode and a single GeV center. We have shown that the semicircular holes increases the photonic band gap size, and therefore improves the cavity quality factor. We have also provided a detailed analysis of the cavity QED for different DNC sizes embedding single GeV center. Our results reveal the cooperativity could reach up to 10^3 in the strong-coupling regime, representing nearly an order of magnitude improvement compared to the previous

4. EFFICIENT FIBER-WAVEGUIDE COUPLING

4.1 Introduction

The utility of photonic devices lies in efficiently coupling photons from nanoscale optical systems to conventional optical components such as lenses and fibers. Unlike micropost [81] and Fabry-Perot [82] cavities, nanobeam cavities are not inherently suited to coupling with conventional free-space or fiber optics due to their ultra-small mode volume and their external radiation pattern. The coupling becomes more complicated as refractive index and frequency of photonic devices increases get higher due to the huge difference in the mode-size and mode effective index between the fiber the nanobeam cavities, as shown in Fig. 4.1. Such mismatch causes an excessive propagation loss additional to other sources such the surface roughness and material absorption.

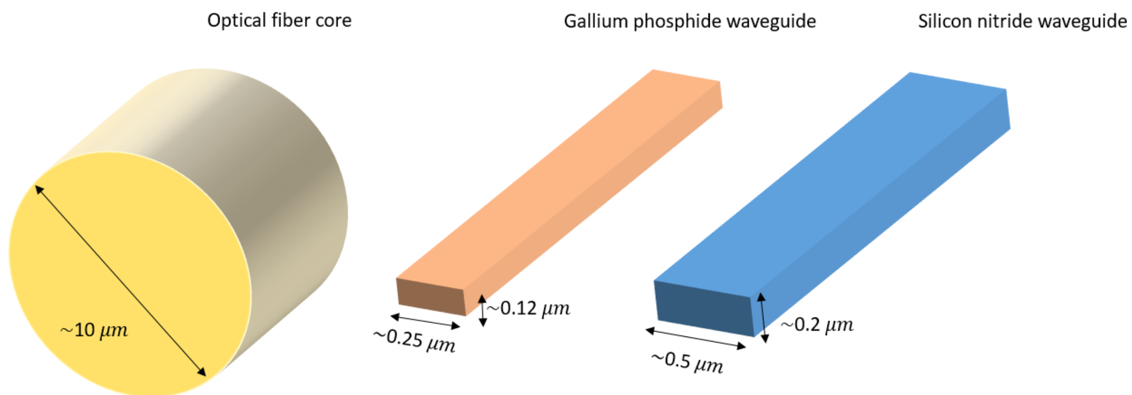

Figure 4.1: Typical dimension of optical single-mode fibre core and photonic waveguide for high-index material (GaP) and low-index material (Si_3N_4) operating at the visible regime.

A wide range of methods have been developed to mitigate the loss in fiber-to-chip light coupling. Figure 4.2 summarizes the most well known techniques used for this purpose. Perhaps the

most popular approach is to use diffractive grating couplers. In this scheme, the waveguide mode is expanded over the lateral direction using an adiabatic taper into a waveguide of about 12 μm width, which matches the mode size of an optical fiber, see Fig. 4.2 (a). The beam is then coupled into the optical fiber by the diffraction from the gratings. Often, the optical fiber is slightly tilted with an angle of about 10° to suppress the second-order Bragg back reflection which would reflect up to half of optical power back into the waveguide [83]. Precise alignment of the angle between the grating and optical fiber would add more complexity into the alignment process, making this method undesirable to many applications. The number of grating teeth is calculated from the phase match condition to ensure the unidirectional coupling. Although various designs have been demonstrated using this method, including multi-layered gratings [84], apodized gratings [85], and metallic gratings [86], the highest coupling efficiency have been demonstrated so far is 81% [87].

Another coupling method that is well developed and studied is called edge coupling where the fiber facet is held against the facet of the chip, as shown in Fig. 4.2 (b). In order to achieve efficient coupling, a mode converter is attached to the end of the waveguide which helps to minimize the mismatch between the fiber mode and the waveguide mode. Inverse taper coupler is one of the several techniques have been proposed for designing such mode converters [88]. In this scheme, waveguides are tapered down, on the contrary of gratings, to increase the mode size which increases the overlap with the the fiber mode. The highest coupling efficiency have been demonstrated so far is 85% when the waveguide taper is separated by 2 μm SiO_2 gap from the chip facet [89]. Typically, in edge coupling method, the light is collected from the waveguide by lensed fibers.

More recently, on-chip dielectric waveguides have been directly coupled to the optical fiber. The coupling scheme heavily relies on overlapping the tapered optical fiber and the waveguide which would yield near unity coupling efficiency via adiabatic mode transfer (Fig. 4.2 (c)). This method reducing complexity of the previous methods in which the phase-matching and mode-matching are not required to achieve highly efficient coupling between the waveguide and the fiber. In addition, the misalignment tolerance is relatively high compared to the previous methods.

The initial work shows 95% coupling efficiency using a biconical fiber taper [90]. Similar coupling efficiency has been demonstrated for conical tapered fiber tip [91].

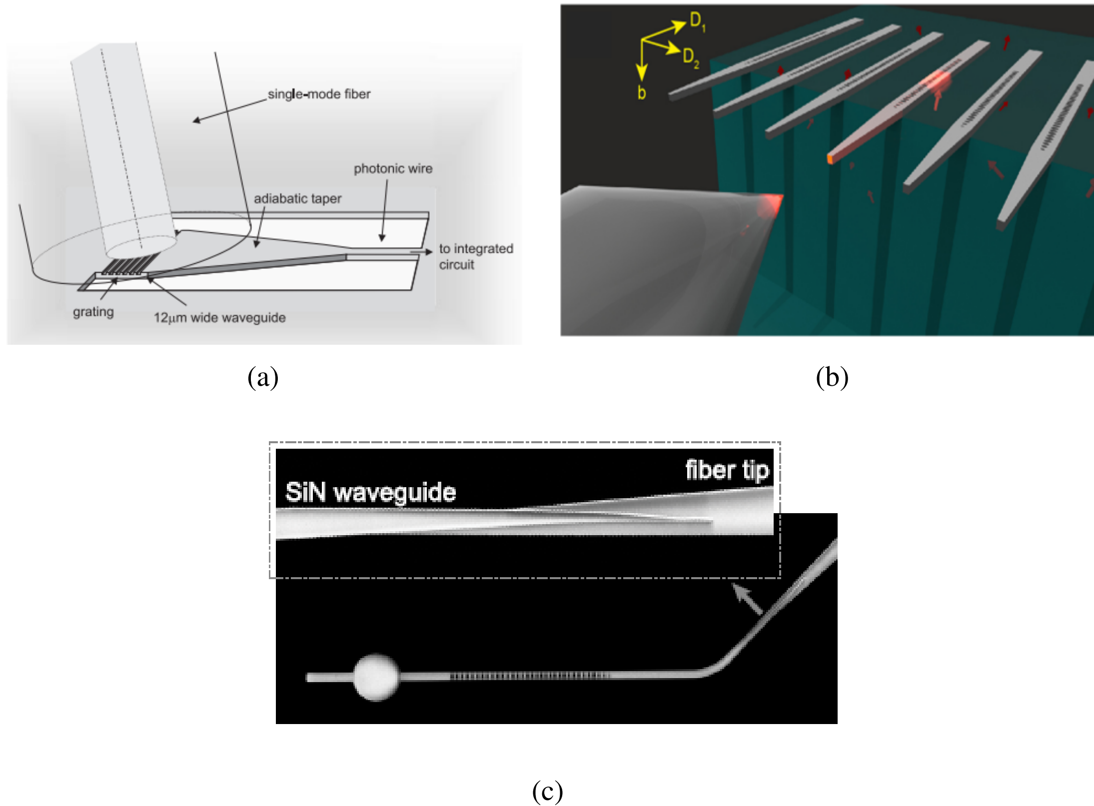

Figure 4.2: (a) Schematic representation of fiber-to-chip light coupling through grating couplers reprinted from ref. [83]. (b) Schematic representation of edge coupling the fiber to Si waveguide using lensed fibers reprinted from ref. [92]. (c) SEM image of conical tapered fiber tip coupled to Si_3N_4 waveguide taper reprinted from ref. [91].

In this chapter, I will explain a new design for high efficient coupling between on-chip Si_3N_4 waveguide and a single-mode optical fiber. First I will address the adiabatic criterion which should be fulfilled to achieve high coupling efficiency. Then, I will discuss the design and fabrication of the tapered fiber tips. Finally, I will discuss the characterization and optimization of the waveguide taper.

4.2 Adiabatic mode transfer

It is a well known in quantum mechanics that if the Hamiltonian of a system is time dependent, the Schrodinger equation of motion has no stationary solution. However, if the Hamiltonian changes slowly, the system would pass through stationary states for all time [93]. Therefore, an eigenmode at a specific moment is adiabatically transformed into a new pure eigenmode at later time. Likewise, if the waveguide cross section is slowly modified along the propagation direction, the optical mode can be adiabatically transferred into another mode with new characteristics.

The question is that how slow the fiber or the waveguide should be changed in order to achieve an adiabatic mode transfer? i.e., what is the upper limit on the taper angle in which the adiabatic propagation can be ensured throughout the taper? To address this question, let us suppose a waveguide with the first two corresponding eigenmodes characterized by their effective indices n_1 and n_2. The length over which these two modes would couple is defined as :

$$z_{\mathrm{b}} = \frac{2\pi}{\beta_1 - \beta_2} = \frac{\lambda}{n_1 - n_2} \tag{4.1}$$

This characteristic length scale is called beating length. Wave numbers n_1 and n_2 can be calculated from the dispersion relation (Fig. 4.3 (b)). If we taper the waveguide over a length-scale z_t, the taper angle will be $\theta = dW/dz$, as illustrated in Fig. 4.3 (a), where w is the half width of the waveguide and z is the distance along the taper. Since we are interested only in $\theta \ll 1$, the length-scale z_t can be expressed as:

$$z_{\mathrm{t}} \approx \frac{W}{\theta} \tag{4.2}$$

The characteristics of mode transformation depend the ratio between these length scales. The first case where $z_{\mathrm{t}}/z_{\mathrm{b}} > 1$ along the taper results in adiabatic mode transformation. Contrariwise, if $z_{\mathrm{t}}/z_{\mathrm{b}} < 1$ the eigenmodes will strongly couple to each other, and so the fundamental mode will have a significant power loss. In between these two conditions, i.e., $z_{\mathrm{t}}/z_{\mathrm{b}} = 1$, indicates the case in which the power is divided equally between the two eigenmodes. The angle in this case can be expressed as:

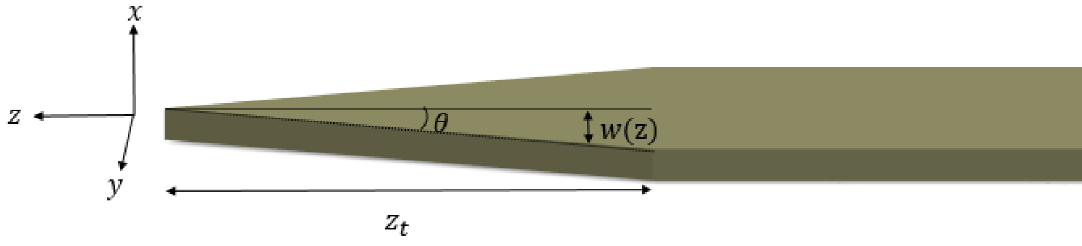

(a)

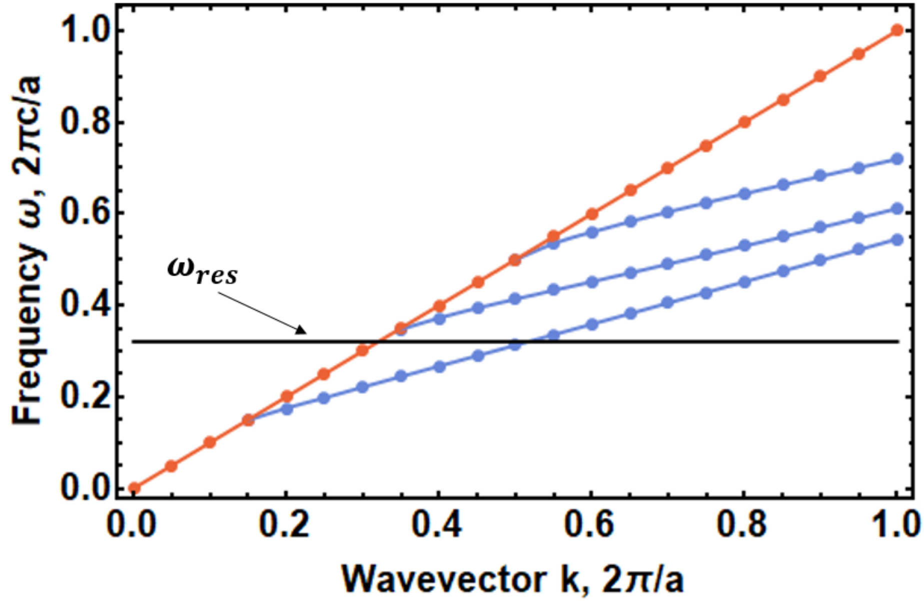

(b)

Figure 4.3: (a) Schematic diagram of a tapered slab semiconductor waveguide. Adiabatic mode transformation can be achieved only for a small taper angle, as explained in the text. (b) Harmonic mode frequencies of Si_3N_4 slab from Fig.4.1 for TE polarization. Blue lines correspond to modes that are localized in the slab. The red line is the light line $\omega = ck$. The black line marks the frequency we are interested in or the cavity resonance.

$$\theta = \frac{W(n_1 - n_2)}{\lambda} \tag{4.3}$$

While this method is based on the wave propagation, another method based on the stationary field distributions can also be used [94]. However, the latter method does not provide a delineation criterion for taper angles which ensures the adiabatic propagation, and those which have significant

power loss.

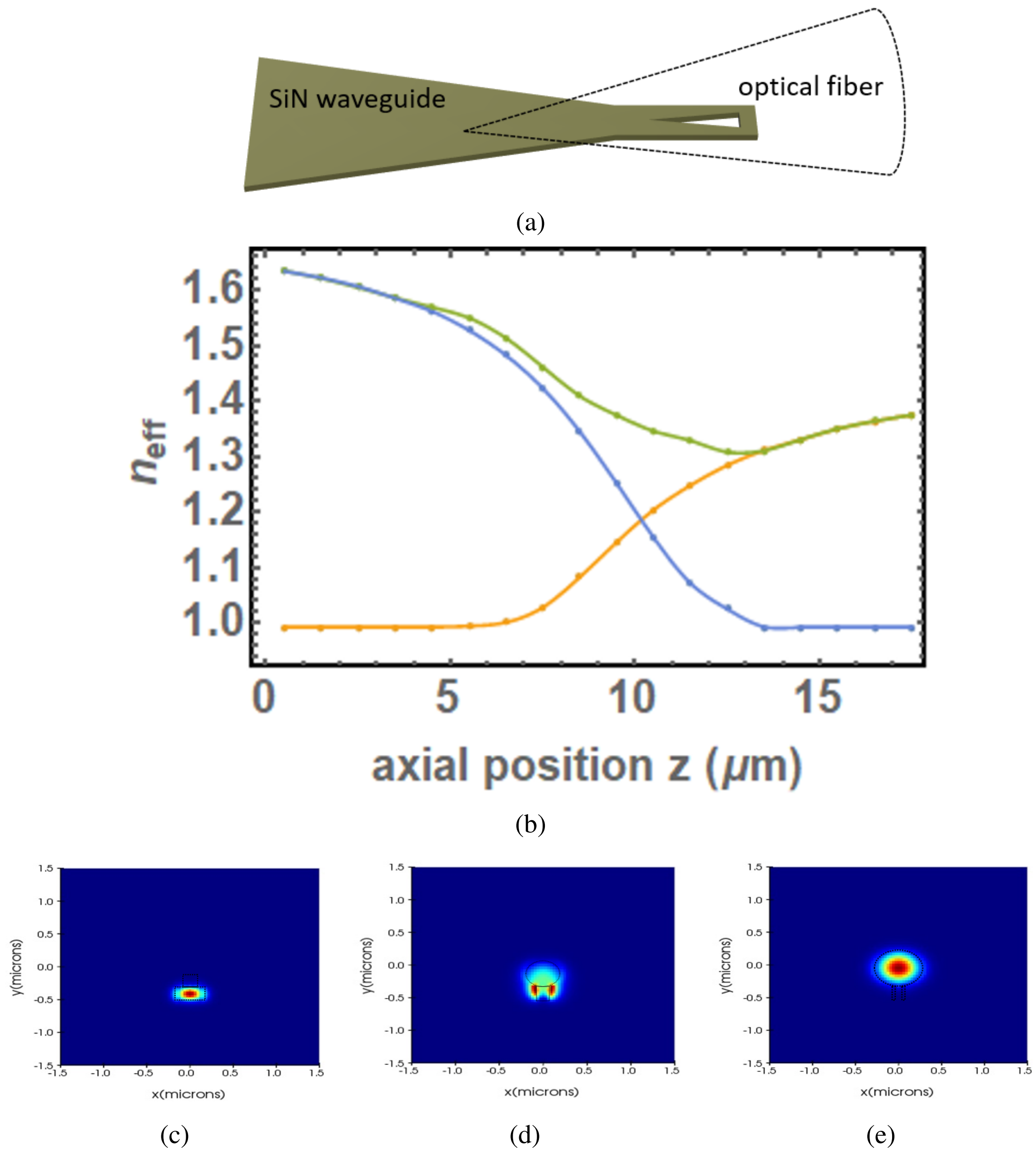

Figure 4.4: (a) Schematic of fiber-waveguide taper adiabatic coupling. The waveguide has a rectangular hole designed to decrease the effective index of the supermode slowly to ensure the adiabatic mode transformation. (b) Effective index n_{eff} of the waveguide mode (blue), fiber mode (orange), and supermode of the combined structure (green). The opening angle of the fiber (waveguide) is of $3.5°$ ($2.2°$). (c) - (e) Cross sections of $|E|^2$ obtained from the FDTD simulation at different normal planes of the combined structure.

4.3 Design and fabrication of waveguide tapers

Since the coupling efficiency between the fiber and waveguide depends on the spatial mode profiles, Our design is based on FDTD simulations to ensure the adiabatic mode transformation. Figure 4.4 (a) shows the schematic of a typical device. A conical tip at the end of an optical fiber is attached to 12 μm $Si_3 N_4$ waveguide. The waveguide taper is designed to evolve from the standard width (560 nm in our case) to sub 150 nm point to allow for mechanical support at the end of the taper. According to dispersion relation (Fig.4.3 (b)) $Si_3 N_4$ slab has two modes at the resonant frequency ω_{res}: the fundamental mode and the radiation mode (light line). The effective index for the waveguide fundamental mode is 1.6, as shown in Fig. 4.4 (b). Therefore, the beating length z_b would be in this particular waveguide is 1 μm. The adiabatic condition can be fulfilled by choosing $z_t > 1$ μm. However, Since we need to couple the optical fiber to the waveguide, we should not rely on the adiabatic condition in the waveguide, but we need to consider the optical fiber taper as well as the region where the waveguide and optical fiber overlap.

The beating length in the combined structure can be determined by the coupling of the lowest effective index of the fundamental mode ($n_{\text{eff}} = 1.3$) and radiation mode (air). The corresponding beating length is 2 μm. Though a long taper length (a small taper angle) is recommended, suspended devices with long tapers might be mechanically unstable. On the other side, small taper length would make the fiber tip unstable when coupled to the waveguide. Based on numerical simulations, we found that the taper length $14 > z_t > 8$ μm, which corresponds to $2° > \theta > 1°$, is a good compromise.

The fabrication of the waveguide taper has been done using e-beam lithography tools and etching process discussed in the previous section. Figure 4.5 displays SEM images of the typical device. The nanobeam cavity and the tapered waveguide are integrated seamlessly in the device layer of the chip which makes the nanobeam cavity optically interfaced with the light transmitted through the waveguide.

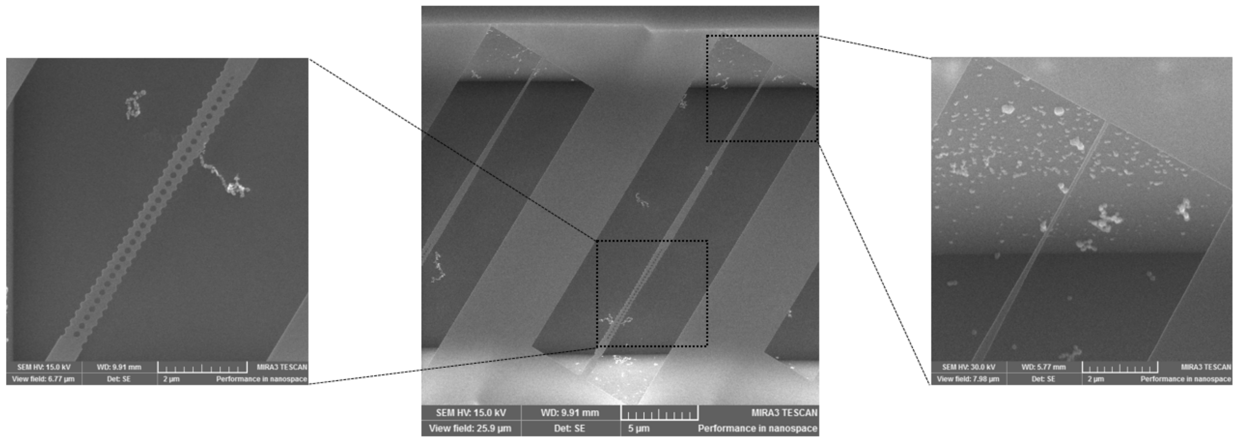

(a)

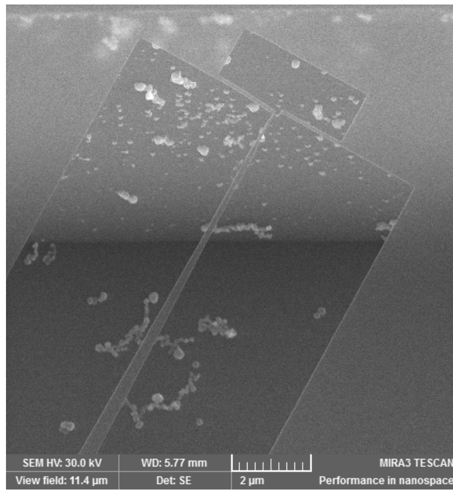

(b)

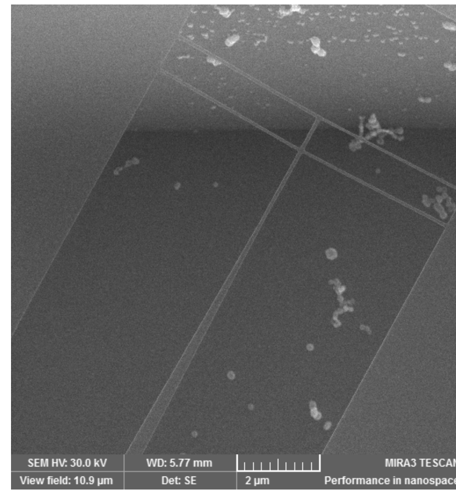

(c)

Figure 4.5: (a) SEM images of the Si_3N_4 nanophotonic device which combines a nanobeam cavity and a feeding waveguide tapered at one end, offering efficient coupling to the optical fiber. (b) & (c) SEM image of the waveguide taper supported by the horizontal rods.

Though the fiber can couple to the waveguide taper on the chip, the coupling might not be stable and huge reflection might be collected from the chip near the waveguide. Several techniques have been proposed to overcome the chip reflection including detaching cavities from the chip using a tungsten tip [63] and vertical waveguide support structures using angled-etching nanofabrication [78]. While the detaching cavities from the chip adds more complexity to the setup in addition to the cost, it is not practical for integrated on-chip nanophotonic networks. As for the latter

technique, the angled-etching requires to change the original design and fabrication method used for nanobeam cavities. In our work, we employ horizontal rods which have a width of ~ 100 nm at the end of the waveguide taper (Fig. 4.5), similar to the supporting tethers implemented for zipper nanobeam cavities [95]. The purpose of the horizontal rods is not only to remove the effects of the chip reflections, but also to ensure robust mechanical performance.

4.4 Design and fabrication of optical fiber tips

Tapering a single-mode optical fibre rapidly can result in a great power loss of the fundamental mode which is localized at the fiber core. This loss is associated with the phase change due to the coupling between the fundamental mode and higher order modes in the fiber cladding. In such case, as wave propagates along the taper, the field cannot change its distribution rapidly enough to keep up with the fundamental mode variance. The idea of adiabatic mode transformation explained previously can also be applied to the optical fiber case, where the fiber taper cross-section is tapered slowly enough such that all power of the fundamental mode remains intact while the coupling to high order modes is negligible [96].

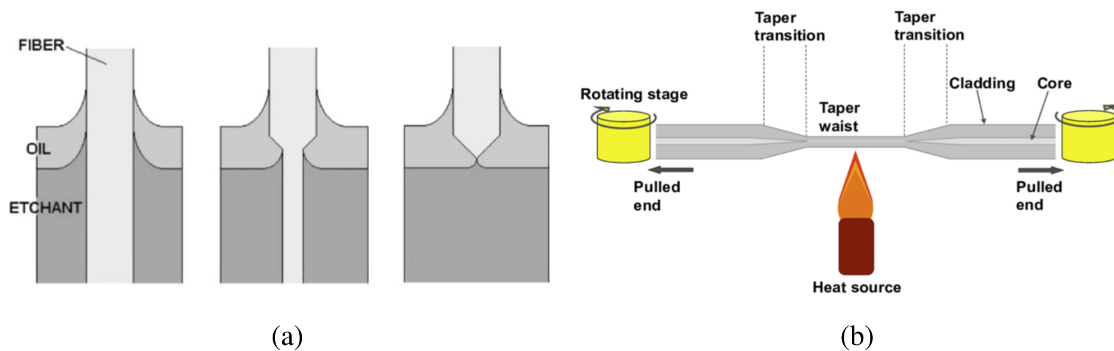

Figure 4.6: (a) Schematic of illustration of the chemical wet etching approach for fabricating tapered fiber tips reprinted from ref. [97]. (b) Schematic of illustration of the heating and pulling approach for fabricating tapered nanofibers reprinted from ref. [98].

Optical fibers can be tapered by two common approaches: chemical wet etching or heating followed by pulling the two fiber ends, as depicted in Fig.4.6. The first approach is based on

etching glass fibers at the meniscus formed at the etchant-oil interface. [97, 99]. Here, the key component is the thin overlayer of an organic solvent which controls the height of the meniscus of the etchant (e.g. hydrofluoric acid). The meniscus height decreases as the fiber diameter shrinks during the etching, forming a smooth taper tip at the end of the process. Another advantage of using the thin overlayer of an organic solvent is to prevent any potential contamination caused by the dangerous etchant vapors.

The other approach to produce tapered optical fibers is based on heating of an optical fiber and subsequently pulling it apart [100]. Typically, the fiber is heated by a heat source, such as an isobutane torch, heating foil, and CO2 lasers, over a variable length. Then, a fast pull is applied to the stage holding the fiber, resulting in a long fiber taper with a conical shape tip. Since the fibre diameter is tapered down to a subwavelength size, the core turns to be too small to guide the light effectively. The fundamental mode therefore has become guided in the cladding region. The incoming light must pass through a taper transition to propagate between the untapered and tapered region. Such a transition must be gradual enough to prevent light to be coupled to higher-order cladding modes, thereby leading to the power loss of the fundamental mode, as mentioned above.

In this work, we employ the chemical wet etching method as we already have access to the main tools and equipment needed in the fabrication process. Another advantage of this method is that the fundamental mode (HE11) does not couple to the cladding mode, as apposed to the heating and pulling method. Therefore the beating length is determined by the coupling between the HE11 core mode at the lowest tapering point and the radiation instead of the cladding modes. The resulting beating length in the fiber taper is comparable to that of the combined structure, and therefore the taper angle is not restricted to $\theta < 5°$, as in the case of the previous method [91].

We confirm the adiabatic mode transformation in our design by FDTD simulations, where a propagating mode of TE-like polarization is launched from the top of the waveguide. We then monitor the power output at the other end of the fiber far from the waveguide. The power transfer is near unity in the optical fiber, indicating that our design satisfies the adiabatic criterion. Figures 4.4 (c) to (e) show the cross-sectional field profiles at various locations along the overlapping

region.

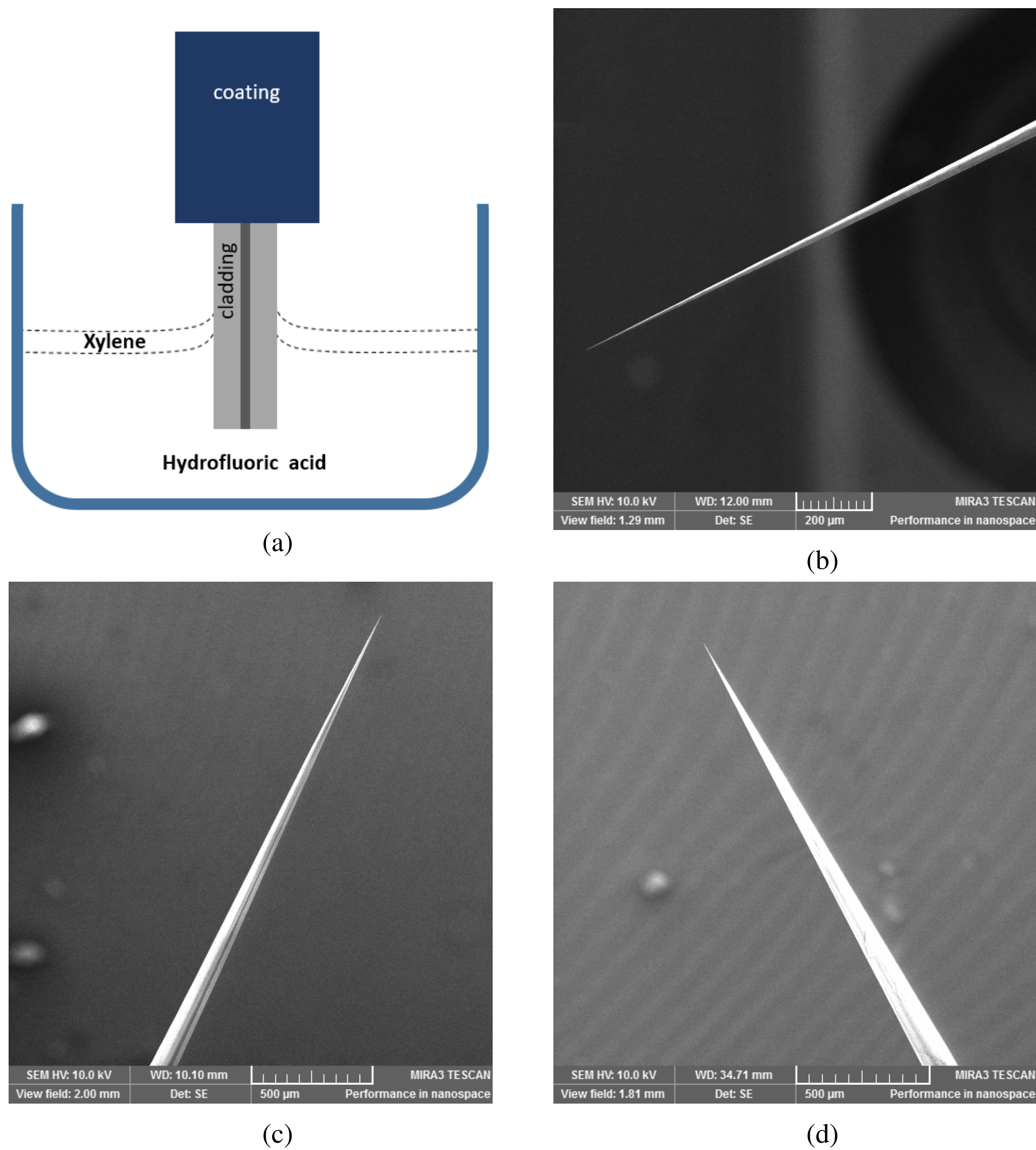

(a)

(b)

(c)

(d)

Figure 4.7: (a) Schematic of fabrication of conical fiber tapers. (b), (d) and (C) SEM images of the final tapered fiber for different speeds resulting in different angles: 2°, 3°, and 4°, respectively.

single-mode fiber (S405-XP, Thorlabs) is tapered as explained in the following recipe. First, the single-mode optical fiber is cleaned in piranha solution to remove any polymer residues left after stripping the coating layer. The cleaned fiber is mounted on a fiber clamp precisely in the

vertical direction to avoid any anisotropic etching. The clamp is mounted on a motorized stage (MT1-Z8, Thorlabs) which is connected to the motor controller (KDC101, Thorlabs). Then, the fiber is submerged in hydrofluoric acid (HF) and pulled slowly in a constant acceleration to form a tapering profile, as depicted in Fig. 4.7 (a). A thin layer of an organic solvent (i.e., o-xylene) on top of HF offers an additional etching via oil-water interface meniscus which promotes a conical shape formation at the end of the fiber. The meniscus height depends on several parameters including the original fiber diameter and the surface tension difference between the acid and the organic solvent [97, 99]. When the HF etches through the whole fiber diameter, the formation of the fiber taper tip has finished and the process self-terminates. Finally, the fiber is cleaned in DI water to clean any acid or oil residues left at the fiber tip.

A key parameter that enables full control over the final taper is the drawing speed of the motorized stage which holds the fiber. This speed can be optimized by trying different speed values while making sure that the fiber is completely etched. Figure 4.7 (b), (c), and (d) shows SEM images for different fibers corresponding to different drawing speed values: 2 μm/s, 1 μm/s, and 0.75 μm/s, respectively. Though all fibers show a tapering angle less than what is required for the adiabatic mode transformation as discussed above, the fiber of the slowest speed and relatively large tapering angle ($\theta \sim 4°$) has a far better performance. The fibers with small tapering angles are unstable and very sensitive to the environment.

4.5 Characterization and optimization

This section describes several measurements used to characterize the fabricated devices. In the first measurement, we measure the power transmission of the fiber tip using a custom setup, where an objective with 0.6 numerical aperture (NA) is used to collect the power from the end of the fiber tip. The fiber is placed onto a fiber holder (HFV002, Thorlabs) which is mounted on a manual stage to offer a precise control of the fiber position to enable the beam collimation. The collected power is then normalized to the power obtained from the same optical fiber with a clean surface. All fibers fabricated in different speed show a high power transmission ($\sim 99\%$), confirming that all three different fiber taper angles (2°, 3°, and 4°), in agreement with the simulation results. The

far-field profile is Gaussian for all three fibers which indicates that most of the power remains in the fundamental mode (HE11), as shown in Fig.4.8 (c).

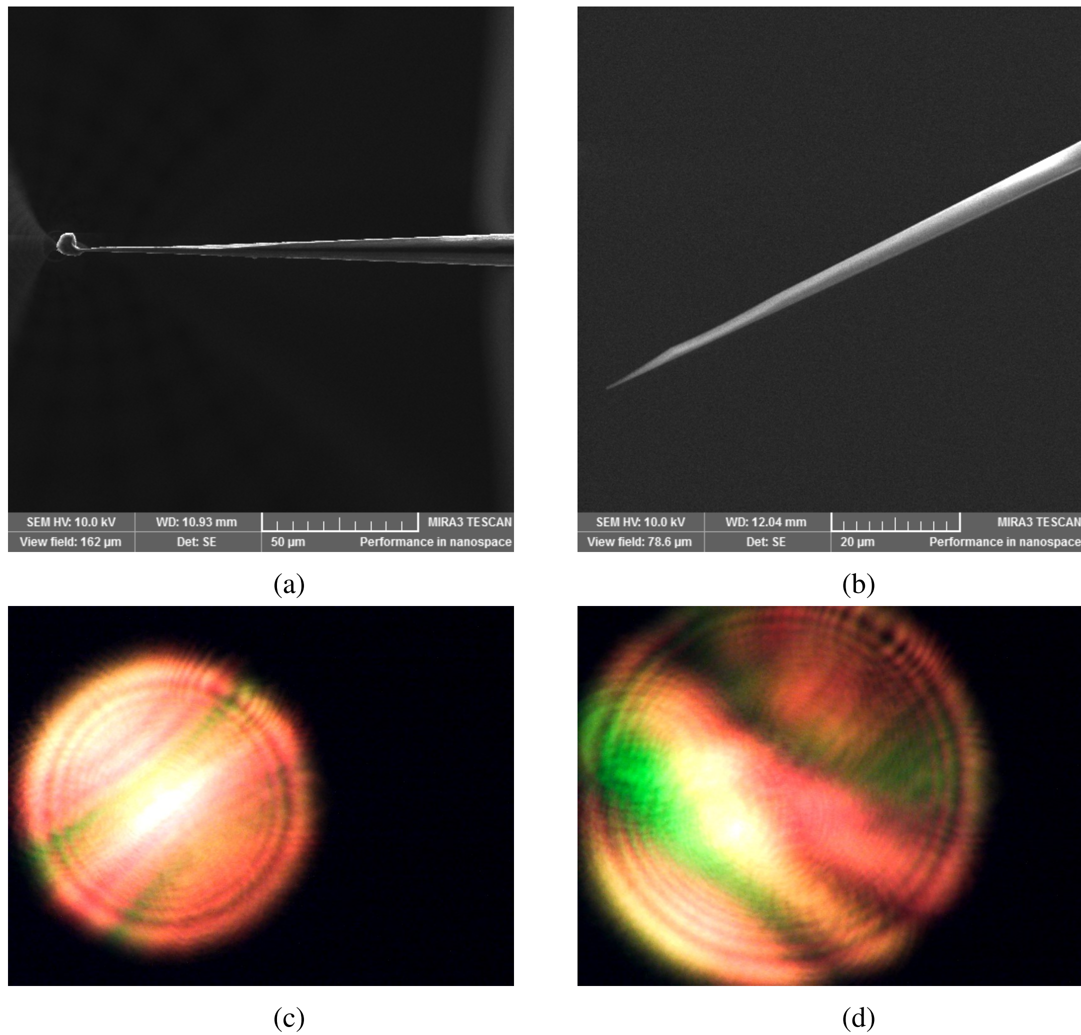

Figure 4.8: SEM images of optical fiber tips fabricated with non-optimized parameters. (a) A small portion of silica remaining at the end of the fiber tip attributed to insufficient acid etching. (b) Asymmetrical conical fiber tip as a result of inaccurate adjustment of the fiber direction. The fiber should be oriented perpendicular to the surface during the etching process. (c) & (d) Far-field mode profile of a rough and smooth fiber tip, respectively.

We note that low power transmission was observed for some fibers due to the fabrication imperfections such as insufficient acid etching, inaccurate adjustment of the fiber direction, and improper

piranha cleaning. SEM image of such imperfect fibers is shown Fig.4.8 (a) and (b). The far field for these fiber always show imperfect Gaussian field profiles due to the huge loss in the fundamental mode (Fig. 4.8 (d)). In fact, analyzing the far-field profiles of the fiber mode is very effective method to check if the fiber tip is single-mode or multi-modes, and it is faster than measuring the power transmission [91]. However, it requires a high resolution camera in order to obtain an accurate far-field profile.

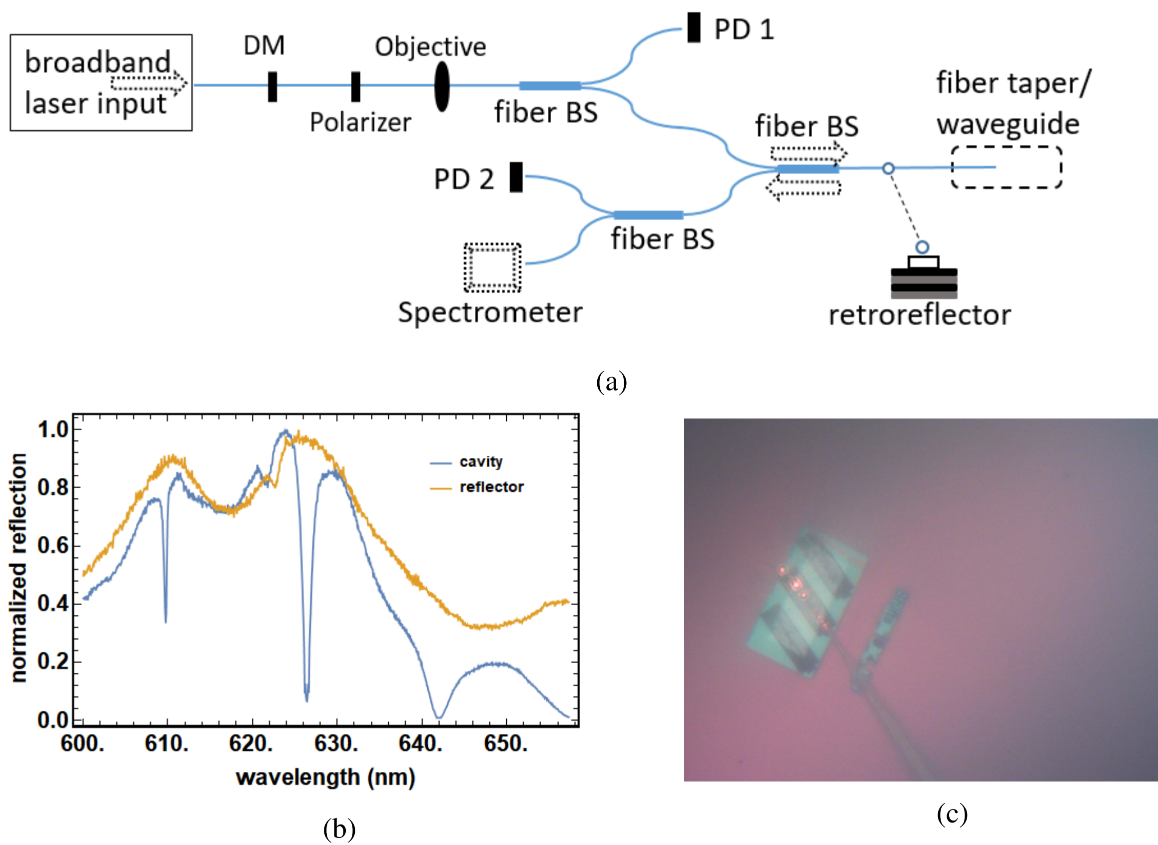

Figure 4.9: (a) Schematic of the coupling efficiency characterization setup. Fibers are connected by splicing two optical fibers end-to-end using fusion splicer tool (FITEL S179). We routinely achieve less than 0.2dB loss. (b) Normalized reflection spectrum of the cavity TE modes centered at wavelength λ = 630 nm. (c) Optical micrograph of a waveguide coupled to an optical fiber obtained from CCD camera.

After confirming that all the power in our fiber tips are attributed to the fundamental mode

(HE11), we bring the fiber tip into close proximity of the waveguide taper to measure the coupling efficiency (μ_c). The fiber tip is mounted on a fiber clamp and then controlled precisely by 3-axis stage which is connected to a piezo controller (MDT693B, Thorlabs). The stage is tilted down around the vertical axis by 10° to offset the fiber tip angle and therefore avoid coupling to the chip surface. The generalized optical-fiber coupling system is shown in Fig. 4.9 (a). A supercontinuum laser (SuperK EVo, NKT Photonics) is launched into a dichroic mirror, which filters unwanted wavelength range, and a polarizer before coupled into the fiber network. Then, 50:50 fiber coupler splits the incoming beam into two paths: one goes to a photodetector to measure the incoming beam intensity, and the other one goes to the fiber tip. After coupling to the waveguide taper, the photonic crystal cavity reflects back all frequencies within its bandgap, except for the cavity resonant modes. Finally, the reflected light splits into paths: one goes to an optical spectrometer to record reflection spectra, and the other path goes to a photodiode to measure the reflected beam intensity. The reflected spectrum is normalized by the reflection collected from a fiber-coupled retroreflector (P1-630R-P01-1, Thorlabs).

Though the retroreflector is suppose to reflect $\sim 98\%$ of the incoming beam, the actual reflection might vary depending on wavelength range designed for each retroreflector. Since our devices are operating slightly lower than the designed wavelength range, we found that the actual reflection of the retroreflector in our case is only $\sim 60\%$. The method for measuring the retroreflector reflection is explained in Appendix C. Figure 4.9 (b) shows the reflection spectra obtained from the nanobeam cavity and retroreflector after taking the reflection loss into account. Interestingly, the ratio of the maximum signal in both spectra approaches unity, indicating that the coupling efficiency between the fiber tip and the waveguide is very high. However, this method can be used only as a qualitative measure of the coupling efficiency.

For an accurate measurement of the coupling efficiency, we used two photodetectors PD1 and PD2 to record the incoming and reflected beam intensity. We first connect the retroreflector and measure the ratio between the value of PD1 and PD2:

(a) (b)

Figure 4.10: (a) Optical micrograph of an optical fiber coupled to a waveguide taper that is not appropriately rotated to the same angle of the optical fiber. (b) Optical micrograph of an optical fiber coupled to the chip behind the waveguide taper indicated by the huge scattering at the end of the taper.

$$\zeta = \frac{PD2}{\beta PD1} \tag{4.4}$$

where β is the measured reflection of the retroreflector. Now, we measure the same ratio between the value of PD1 and PD2 but after the fiber tip is connected and coupled to the waveguide taper. The coupling efficiency is given by:

$$\mu_{\mathrm{c}}{}^{2} = \frac{PD2}{\zeta \mu_{\mathrm{Bragg}} PD1} \tag{4.5}$$

where μ_{Bragg} is the reflection of the the nanobeam cavity Bragg mirror which is assumed to be approximately 1. The maximum coupling efficiency we have achieved is $\mu_{\mathrm{c}} = 0.96 \pm 0.02$. The error bar reflects the fluctuations in the data collected by photodetectors which is averaged over a long period. However, sometimes we noticed a degradation in the coupling efficiency after after some period of time due to the instability of fiber during the coupling to the waveguide. Such instability can be attributed to mismatching between the fiber and waveguide angle, unexpected coupling to the chip nearby, or ruined fiber tip as a result of hard pushing to the fiber (Fig. 4.10). The fiber stability can be enhanced by grooving the chip nearby the waveguide taper and adding

nano-rods to support the suspended device. The loss in the coupling efficiency of due to supporting rods is negligible and can be suppressed by shrinking the rod size and adding extra rods, see Fig.4.5 (b) and (c).

We verify our measurements by performing FDTD simulations on some width dependence parameters. Figure (a) 4.11 reveals the relation between the coupling efficiency and length of the physical contact region between the fiber and the waveguide. The width of the waveguide was kept constant dx = 150 nm while extending the contact region. The results show that the coupling efficiency changes exponentially as the contact region is prolonged. Interestingly, the the saturation starts at a short distance ($\sim 7\ \mu$m), in agreement with the experimental observations. In comparison, waveguides fabricated by the angled etching method require much longer overlapping contact region, increasing the footprint by at least a factor of 2 [78]. On the other hand, the coupling efficiency depends heavily on the width of the waveguide taper. Figure 4.11 (b) shows that coupling efficiency is inverse proportional to the waveguide width, and as the nanobeam widens the efficiency starts to saturate at a small fraction.

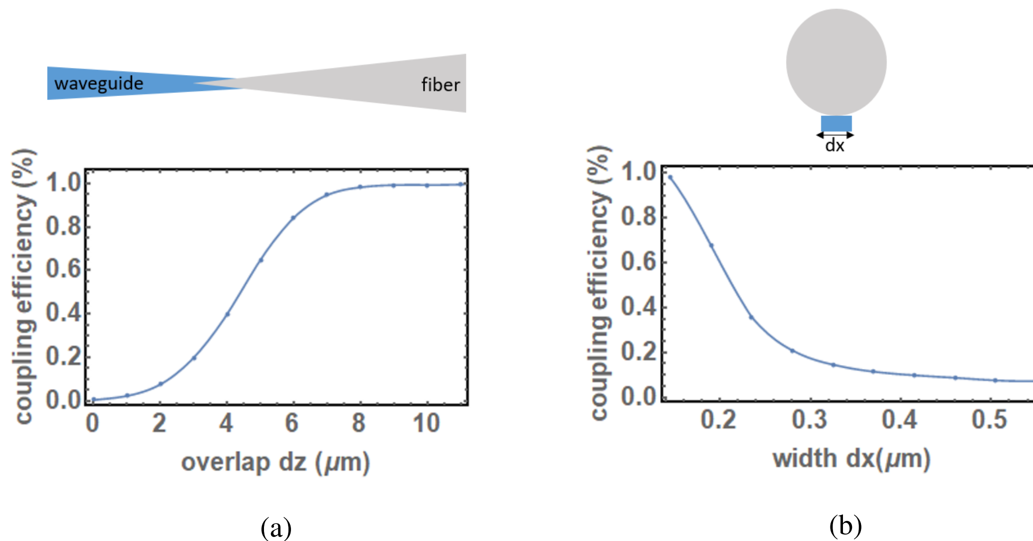

(a) (b)

Figure 4.11: (a) & (b) The coupling efficiency of TE-polarized waveguide mode to the optical-fiber HE11 mode as a function of fiber-waveguide overlap and waveguide width, respectively, obtained from FDTD simulations.

4.6 Conclusion

We have studied the fiber-waveguide optical coupling which is very essential in integrated quantum photonics. The coupling can be enhanced by tapering the waveguide and optical fiber down to small sizes while the opening angle is kept below the critical angle required for the adiabatic mode transformation. The optical fibers were fabricated by chemical wet etching technique, which is very reliable and flexible compared to the heating and pulling technique. Our measurements indicate coupling efficiencies above 90% for a range of devices. The maximum coupling efficiency we have demonstrated is $\mu_c = 0.96 \pm 0.02$. Our photonic networks utilize suspended waveguide tapers, which renders a low optical loss despite being supported through horizontal nano-rods connected to the chip. This work is expected to find an advantageous application for characterizing on-chip optical devices in quantum non-linear optics [101] and optomechanics systems [102] where the highly efficient collection and detection of photons is very crucial.

5. SUMMARY

In this dissertation, we have developed nanobeam cavities to increase the light-matter interaction which is very essential to many applications such as chemical sensing, nonlinear optics, quantum information processing and cavity optomechanics.

We have focused on designing and fabricating nanobeam cavities based on different dielectric materials. The first device is made of gallium phosphide material which feature unique optical properties including the high index of refraction. We have developed so-called "semicircular holes" design for nanobeam cavities that combines an ultrahigh Q/V value and high transmission. This design is not limited only to GaP material, but it can be implemented in various dielectric materials as well. The key feature of this design manifested in the corresponding gain in the cavity mirror strength. Such cavities are suitable to host single photon emitters and establish strong coupling with the confined light. We have studied a cavity QED system that involves a single germanium vacancy center incorporated in a diamond nanocrystal that is placed on top of the nanobeam cavity. Our numerical results show that a strong coupling regime can be achieved for the first time using a solid-state single photon emitter.

Since GaP material is hard to grow and fabricate, we have considered an alternative material, namely, silicon nitride which is more feasible than the previous one. Simulations show that Q/V value of Si_3N_4 nanobeam cavities is lower than those based on GaP by almost two orders of magnitude. However, we were able to study the cavity QED analysis of a system that involves Si_3N_4 nanobeam cavities and diamond nanocrystal placed on top of it. Numerical results demonstrate a strong coupling regime for nanobeam cavities with $Q/V > 10^4$, which is close to the maximum Q/V value. The fabrication method was discussed thoroughly in this work for both GaP and Si_3N_4 devices along with necessary optimizations needed for the EBL system. We have experimentally measured and characterized nanobeam cavities for Si_3N_4 grown by different growing methods, namely PECVD and LPCVD. The maximum measured quality factor was $\sim 10^4$, which is attributed to devices grown by the LPCVD method.

The light was coupled to the nanobeam devices via fiber-waveguide interface. Engineering the tapering profile in both structures allows for efficient fiber-waveguide coupling by means of adiabatic mode transfer. We have illustrated the fabrication process of the fiber taper which is based on chemical wet etching method. The maximum coupling efficiency we have demonstrated is 96%. This work will facilitate the design and fabrication of photonic devices used in a wide range of quantum applications.

REFERENCES

[1] `https://enacademic.com/dic.nsf/enwiki/914112`.

[2] `https://enacademic.com/dic.nsf/enwiki/914112`.

[3] J. Meijer, B. Burchard, M. Domhan, C. Wittmann, T. Gaebel, I. Popa, F. Jelezko, J. Wrachtrup, *Applied Physics Letters* **2005**, *87*.

[4] H. Bernien, B. Hensen, W. Pfaff, G. Koolstra, M. S. Blok, L. Robledo, T. H. Taminiau, M. Markham, D. J. Twitchen, L. Childress, R. Hanson, *Nature* **2013**, *497*, 86–90.

[5] P. Neumann, N. Mizuochi, F. Rempp, P. Hemmer, H. Watanabe, S. Yamasaki, V. Jacques, T. Gaebel, F. Jelezko, J. Wrachtrup, *Science* **2008**, *320*, 1326–9.

[6] M. G. Dutt, L. Childress, L. Jiang, E. Togan, J. Maze, F. Jelezko, A. Zibrov, P. Hemmer, M. Lukin, *Science* **2007**, *316*, 1312–1316.

[7] J. R. Maze, P. L. Stanwix, J. S. Hodges, S. Hong, J. M. Taylor, P. Cappellaro, L. Jiang, M. V. Dutt, E. Togan, A. S. Zibrov, A. Yacoby, R. L. Walsworth, M. D. Lukin, *Nature* **2008**, *455*, 644–7.

[8] M. S. Grinolds, S. Hong, P. Maletinsky, L. Luan, M. D. Lukin, R. L. Walsworth, A. Yacoby, *Nature Physics* **2013**, *9*, 215.

[9] G. Kucsko, P. C. Maurer, N. Y. Yao, M. Kubo, H. J. Noh, P. K. Lo, H. Park, M. D. Lukin, *Nature* **2013**, *500*, 54.

[10] T. Muller, C. Hepp, B. Pingault, E. Neu, S. Gsell, M. Schreck, H. Sternschulte, D. Steinmuller-Nethl, C. Becher, M. Atature, *Nature Communications* **2014**, *5*.

[11] A. Gali, J. R. Maze, *Physical Review B* **2013**, *88*.

[12] M. Leifgen, T. Schroder, F. Gadeke, R. Riemann, V. Metillon, E. Neu, C. Hepp, C. Arend, C. Becher, K. Lauritsen, O. Benson, *New Journal of Physics* **2014**, *16*.

[13] M. H. Metsch, K. Senkalla, B. Tratzmiller, J. Scheuer, M. Kern, J. Achard, A. Tallaire, M. B. Plenio, P. Siyushev, F. Jelezko, *Physical Review Letters* **2019**, *122*.

[14] T. D. Merson, S. Castelletto, I. Aharonovich, A. Turbic, T. J. Kilpatrick, A. M. Turnley, *Optics Letters* **2013**, *38*, 4170–4173.

[15] E. Neu, M. Agio, C. Becher, *Optics Express* **2012**, *20*, 19956–19971.

[16] M. K. Bhaskar, D. D. Sukachev, A. Sipahigil, R. E. Evans, M. J. Burek, C. T. Nguyen, L. J. Rogers, P. Siyushev, M. H. Metsch, H. Park, F. Jelezko, M. Loncar, M. D. Lukin, *Physical Review Letters* **2017**, *118*.

[17] G. Hasnain, K. Tai, L. Yang, Y. H. Wang, R. J. Fischer, J. D. Wynn, B. Weir, N. K. Dutta, A. Y. Cho, *Ieee Journal of Quantum Electronics* **1991**, *27*, 1377–1385.

[18] E. Yablonovitch, *Physical Review Letters* **1987**, *58*, 2059–2062.

[19] S. John, *Physical Review Letters* **1987**, *58*, 2486–2489.

[20] J. D. Joannopoulos, *Photonic crystals : molding the flow of light*, 2nd, Princeton University Press, Princeton, **2008**.

[21] P. R. Villeneuve, S. H. Fan, J. D. Joannopoulos, *Physical Review B* **1996**, *54*, 7837–7842.

[22] E. Yablonovitch, T. J. Gmitter, K. M. Leung, *Physical Review Letters* **1991**, *67*, 2295–2298.

[23] P. T. Kristensen, C. Van Vlack, S. Hughes, *Optics Letters* **2012**, *37*, 1649–1651.

[24] Q. M. Quan, I. B. Burgess, S. K. Y. Tang, D. L. Floyd, M. Loncar, *Optics Express* **2011**, *19*, 22191–22197.

[25] S. R. Hu, S. M. Weiss, *Acs Photonics* **2016**, *3*, 1647–1653.

[26] M. Eichenfield, R. Camacho, J. Chan, K. J. Vahala, O. Painter, *Nature* **2009**, *459*, 550–U79.

[27] B.-H. Ahn, J.-H. Kang, M.-K. Kim, J.-H. Song, B. Min, K.-S. Kim, Y.-H. Lee, *Optics Express* **2010**, *18*, 5654–5660.

[28] A. Alajlan, V. Cojocaru, A. V. Akimov, *Optical Materials Express* **2019**, *9*, 1678–1688.

[29] D. Englund, I. Fushman, J. Vuckovic, *Optics Express* **2005**, *13*, 5961–5975.

[30] K. Sakoda, *Optical properties of photonic crystals*, 2nd, Springer, Berlin ; New York, **2005**.

[31] Y. Akahane, T. Asano, B.-S. Song, S. Noda, *Nature* **2003**, *425*, 944–947.

[32] Q. Quan, P. B. Deotare, M. Loncar, *Applied Physics Letters* **2010**, *96*, 203102.

[33] Q. Quan, M. Loncar, *Optics Express* **2011**, *19*, 18529–18542.

[34] M. Notomi, E. Kuramochi, H. Taniyama, *Optics Express* **2008**, *16*, 11095–11102.

[35] B. W. Shore, P. L. Knight, *Journal of Modern Optics* **1993**, *40*, 1195–1238.

[36] A. Yariv, *Quantum Electronics*, 3rd, John Wiley, New York, **1989**.

[37] Y. N. Palyanov, I. N. Kupriyanov, Y. M. Borzdov, N. V. Surovtsev, *Scientific Reports* **2015**, *5*.

[38] E. Neu, M. Agio, C. Becher, *Optics Express* **2012**, *20*, 19956–19971.

[39] M. W. McCutcheon, M. Loncar, *Optics Express* **2008**, *16*, 19136–19145.

[40] E. M. Purcell, *Physical Review* **1946**, *69*, 681–681.

[41] P. E. Barclay, K. M. Fu, C. Santori, R. G. Beausoleil, *Optics Express* **2009**, *17*, 9588–9601.

[42] I. I. Vlasov, A. A. Shiryaev, T. Rendler, S. Steinert, S. Y. Lee, D. Antonov, M. Voros, F. Jelezko, A. V. Fisenko, L. F. Semjonova, J. Biskupek, U. Kaiser, O. I. Lebedev, I. Sildos, P. R. Hemmer, V. I. Konov, A. Gali, J. Wrachtrup, *Nature Nanotechnology* **2014**, *9*, 54–58.

[43] S. V. Bolshedvorskii, A. I. Zeleneev, V. V. Vorobyov, V. V. Soshenko, O. R. Rubinas, L. A. Zhulikov, P. A. Pivovarov, V. N. Sorokin, A. N. Smolyaninov, L. F. Kulikova, A. S. Garanina, S. G. Lyapin, V. N. Agafonov, R. E. Uzbekov, V. A. Davydov, A. V. Akimov, *ACS Applied Nano Materials* **2019**.

[44] S. D. Gupta, B. Jatothu, *Plant Biotechnology Reports* **2013**, *7*, 211–220.

[45] X. S. Lu, S. Huang, M. B. Diaz, N. Kotulak, R. Y. Hao, R. Opila, A. Barnett, *Ieee Journal of Photovoltaics* **2012**, *2*, 214–220.

[46] A. C. Lin, R. Bassiri, S. Omar, A. S. Markosyan, B. Lantz, R. Route, R. L. Byer, J. S. Harris, M. M. Fejer, *Optical Materials Express* **2015**, *5*, 1890–1897.

[47] K. Rivoire, Z. L. Lin, F. Hatami, W. T. Masselink, J. Vuckovic, *Optics Express* **2009**, *17*, 22609–22615.

[48] J. K. W. Yang, B. Cord, H. G. Duan, K. K. Berggren, J. Klingfus, S. W. Nam, K. B. Kim, M. J. Rooks, *Journal of Vacuum Science Technology B* **2009**, *27*, 2622–2627.

[49] K. Schneider, P. Welter, Y. Baumgartner, H. Hahn, L. Czornomaz, P. Seidler, *Journal of Lightwave Technology* **2018**, *36*, 2994–3002.

[50] Y. F. Chen, *Microelectronic Engineering* **2015**, *135*, 57–72.

[51] H. W. Ro, C. L. Soles, *Materials Today* **2011**, *14*, 20–33.

[52] K. Rivoire, A. Faraon, J. Vuckovic, *Applied Physics Letters* **2008**, *93*.

[53] R. E. Evans, M. K. Bhaskar, D. D. Sukachev, C. T. Nguyen, A. Sipahigil, M. J. Burek, B. Machielse, G. H. Zhang, A. S. Zibrov, E. Bielejec, H. Park, M. Loncar, M. D. Lukin, *Science* **2018**, *362*, 662–+.

[54] J. Riedrich-Moller, L. Kipfstuhl, C. Hepp, E. Neu, C. Pauly, F. Mucklich, A. Baur, M. Wandt, S. Wolff, M. Fischer, S. Gsell, M. Schreck, C. Becher, *Nature Nanotechnology* **2012**, *7*, 69–74.

[55] M. J. Burek, Y. W. Chu, M. S. Z. Liddy, P. Patel, J. Rochman, S. Meesala, W. Hong, Q. M. Quan, M. D. Lukin, M. Loncar, *Nature Communications* **2014**, *5*.

[56] Y. Xuan, Y. Liu, L. T. Varghese, A. J. Metcalf, X. X. Xue, P. H. Wang, K. Han, J. A. Jaramillo-Villegas, A. Al Noman, C. Wang, S. Kim, M. Teng, Y. J. Lee, B. Niu, L. Fan, J. Wang, D. E. Leaird, A. M. Weiner, M. H. Qi, *Optica* **2016**, *3*, 1171–1180.

[57] D. J. Moss, R. Morandotti, A. L. Gaeta, M. Lipson, *Nature Photonics* **2013**, *7*, 597–607.

[58] Y. X. Liu, M. Davanco, V. Aksyuk, K. Srinivasan, *Physical Review Letters* **2013**, *110*.

[59] E. D. Palik, G. Ghosh, *Handbook of optical constants of solids*, Academic Press, **1999**.

[60] M. Barth, J. Kouba, J. Stingl, B. Lochel, O. Bensona, *Optics Express* **2007**, *15*, 17231–17240.

[61] M. Barth, N. Nusse, J. Stingl, B. Lochel, O. Benson, *Applied Physics Letters* **2008**, *93*.

[62] J. Chan, M. Eichenfield, R. Camacho, O. Painter, *Optics Express* **2009**, *17*, 3802–3817.

[63] T. G. Tiecke, J. D. Thompson, N. P. de Leon, L. R. Liu, V. Vuletic, M. D. Lukin, *Nature* **2014**, *508*, 241–244.

[64] M. Khan, T. Babinec, M. W. McCutcheon, P. Deotare, M. Loncar, *Optics Letters* **2011**, *36*, 421–423.

[65] M. Barth, J. Kouba, J. Stingl, B. Lochel, O. Benson, *Opt Express* **2007**, *15*, 17231–40.

[66] F. Mei, M. Feng, Y. F. Yu, Z. M. Zhang, *Physical Review A* **2009**, *80*.

[67] P. van Loock, T. D. Ladd, K. Sanaka, F. Yamaguchi, K. Nemoto, W. J. Munro, Y. Yamamoto, *Physical Review Letters* **2006**, *96*.

[68] B. C. Joshi, G. Eranna, D. P. Runthala, B. B. Dixit, O. P. Wadhawan, P. D. Vyas, *Indian Journal of Engineering and Materials Sciences* **2000**, *7*, 303–309.

[69] J. Gumpher, W. Bather, N. Mehta, D. Wedel, *Journal of the Electrochemical Society* **2004**, *151*, G353–G359.

[70] M. Gupta, V. K. Rathi, R. Thangaraj, O. P. Agnihotri, K. S. Chari, *Thin Solid Films* **1991**, *204*, 77–106.

[71] H. J. Schliwinski, U. Schnakenberg, W. Windbracke, H. Neff, P. Lange, *Journal of the Electrochemical Society* **1992**, *139*, 1730–1735.

[72] A. Stoffel, A. Kovacs, W. Kronast, B. Muller, *Journal of Micromechanics and Microengineering* **1996**, *6*, 1–13.

[73] J. G. E. Gardeniers, H. A. C. Tilmans, C. C. G. Visser, *Journal of Vacuum Science Technology A* **1996**, *14*, 2879–2892.

[74] A. Stoffel, A. Kovacs, W. Kronast, B. Muller, *Journal of Micromechanics and Microengineering* **1996**, *6*, 1–13.

[75] K. R. Williams, K. Gupta, M. Wasilik, *Journal of Microelectromechanical Systems* **2003**, *12*, 761–778.

[76] H. Wang, G. M. Laws, S. Milicic, P. Boland, A. Handugan, M. Pratt, T. Eschrich, S. Myhajlenko, J. A. Allgair, B. Bunday, *Journal of Vacuum Science Technology B* **2007**, *25*, 102–105.

[77] L. Z. Li, T. Schroeder, E. H. Chen, M. Walsh, I. Bayn, J. Goldstein, O. Gaathon, M. E. Trusheim, M. Lu, J. Mower, M. Cotlet, M. L. Markham, D. J. Twitchen, D. Englund, *Nature Communications* **2015**, *6*.

[78] M. J. Burek, C. Meuwly, R. E. Evans, M. K. Bhaskar, A. Sipahigil, S. Meesala, B. Machielse, D. D. Sukachev, C. T. Nguyen, J. L. Pacheco, E. Bielejec, M. D. Lukin, M. Loncar, *Physical Review Applied* **2017**, *8*.

[79] R. Ulrich, A. Simon, *Applied Optics* **1979**, *18*, 2241–2251.

[80] N. Tas, T. Sonnenberg, H. Jansen, R. Legtenberg, M. Elwenspoek, *Journal of Micromechanics and Microengineering* **1996**, *6*, 385–397.

[81] M. Pelton, C. Santori, J. Vuckovic, B. Y. Zhang, G. S. Solomon, J. Plant, Y. Yamamoto, *Physical Review Letters* **2002**, *89*.

[82] J. McKeever, A. Boca, A. D. Boozer, R. Miller, J. R. Buck, A. Kuzmich, H. J. Kimble, *Science* **2004**, *303*, 1992–1994.

[83] D. Taillaert, F. Van Laere, M. Ayre, W. Bogaerts, D. Van Thourhout, P. Bienstman, R. Baets, *Japanese Journal of Applied Physics* **2006**, *45*, 6071–6077.

[84] D. Vermeulen, S. Selvaraja, P. Verheyen, G. Lepage, W. Bogaerts, P. Absil, D. Van Thourhout, G. Roelkens, *Optics Express* **2010**, *18*, 18278–18283.

[85] Y. B. Tang, Z. Wang, L. Wosinski, U. Westergren, S. L. He, *Optics Letters* **2010**, *35*, 1290–1292.

[86] S. Scheerlinck, J. Schrauwen, F. Van Laere, D. Taillaert, D. Van Thourhout, R. Baets, *Optics Express* **2007**, *15*, 9625–9630.

[87] R. Marchetti, C. Lacava, A. Khokhar, X. Chen, I. Cristiani, D. J. Richardson, G. T. Reed, P. Petropoulos, P. Minzioni, *Scientific Reports* **2017**, *7*.

[88] V. R. Almeida, R. R. Panepucci, M. Lipson, *Optics Letters* **2003**, *28*, 1302–1304.

[89] J. Cardenas, C. B. Poitras, K. Luke, L. W. Luo, P. A. Morton, M. Lipson, *Ieee Photonics Technology Letters* **2014**, *26*, 2380–2382.

[90] S. Groblacher, J. T. Hill, A. H. Safavi-Naeini, J. Chan, O. Painter, *Applied Physics Letters* **2013**, *103*.

[91] T. G. Tiecke, K. P. Nayak, J. D. Thompson, T. Peyronel, N. P. de Leon, V. Vuletic, M. D. Lukin, *Optica* **2015**, *2*, 70–75.

[92] M. Dibos, M. Raha, C. M. Phenicie, J. D. Thompson, *Physical Review Letters* **2018**, *120*.

[93] E. Merzbacher, *Quantum mechanics*, 3nd, John Wiley, New York, **1998**.

[94] S. R. Park, B. H. O, *Ieee Photonics Technology Letters* **2001**, *13*, 675–677.

[95] J. D. Cohen, S. M. Meenehan, O. Painter, *Optics Express* **2013**, *21*, 11227–11236.

[96] J. D. Love, W. M. Henry, W. J. Stewart, R. J. Black, S. Lacroix, F. Gonthier, *Iee Proceedings-J Optoelectronics* **1991**, *138*, 343–354.

[97] H. Muramatsu, K. Homma, N. Chiba, N. Yamamoto, A. Egawa, *Journal of Microscopy-Oxford* **1999**, *194*, 383–387.

[98] S. Korposh, S. W. James, S. W. Lee, R. P. Tatam, *Sensors* **2019**, *19*.

[99] P. Hoffmann, B. Dutoit, R. P. Salathe, *Ultramicroscopy* **1995**, *61*, 165–170.

[100] L. M. Tong, R. R. Gattass, J. B. Ashcom, S. L. He, J. Y. Lou, M. Y. Shen, I. Maxwell, E. Mazur, *Nature* **2003**, *426*, 816–819.

[101] D. E. Chang, V. Vuletic, M. D. Lukin, *Nature Photonics* **2014**, *8*, 685–694.

[102] M. Aspelmeyer, T. J. Kippenberg, F. Marquardt, *Reviews of Modern Physics* **2014**, *86*, 1391–1452.

[103] D. Logan, *A first course in the finite element method cengage learning*, Mason, **2007**.

[104] A. F. Oskooi, D. Roundy, M. Ibanescu, P. Bermel, J. D. Joannopoulos, S. G. Johnson, *Computer Physics Communications* **2010**, *181*, 687–702.

APPENDIX A

MEEP SOFTWARE FOR FDTD SIMULATIONS

Though nanobeam cavities used in this work are designed and modeled using FDTD numerical simulations, the initial numerical optimizations were based on FEM simulations (COMSOL) which divides the system into small nonuniform grids and then combines all element equations into a global set of equations [103]. COMSOL has many advantages for plasmonic structures in which relatively large wavelengths are divided with nano-scale skin depths. However, this flexibility has negative consequences (such as spurious modes and mesh roughness) in dielectric devices where the refractive index varies slightly between dielectric materials. FDTD has the advantages of robustness and simplicity as it provides versatile modeling technique to solve time-dependent Maxwell equations for any arbitrary materials (including nonlinear, dispersive, and anisotropic materials) in single simulation run.

Despite the fact that many commercial FDTD software packages are available for purchase, scientific research often demands the flexibility to access and play with the source code. Meep is a free software package that implements FDTD method for computational electromagnetics. It is mainly designed to solve eigenfrequencies of photonic devices and calculate the associated figure of merits such quality factors, mode volume, band gaps, and transmission [104]. Here, we provide detailed discussions for implementing MEEP software in our geometries along with the manuscripts.

A.1 Photonic band structure

Universal crystals of molecules and atoms are not continuous, and therefore do not possess continuous translational symmetry. Instead, they have possess discrete translational symmetry which makes them invariant under translations of a fixed distance. Likewise, photonic crystals have discrete symmetry which creates a periodic dielectric function $\epsilon(\boldsymbol{x}) = \epsilon(\boldsymbol{x} + \boldsymbol{R})$ for some vector $\boldsymbol{R}$ which is an integral multiple of primitive lattice vector $\boldsymbol{a}$ (i.e., $\boldsymbol{R}$ = m$\boldsymbol{a}$, where m is an

integer).

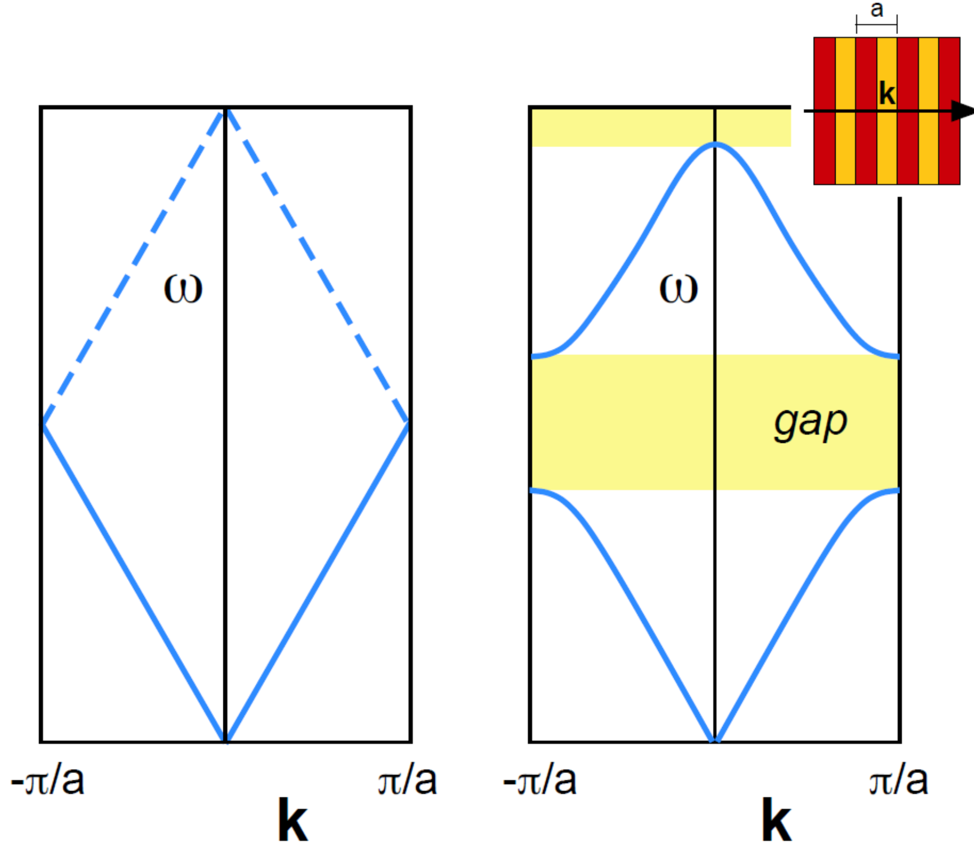

Figure A.1: Left: Band diagram of a uniform one-dimensional medium. Right: Band diagram of a multilayer film that is periodic in one direction (inset). The gap arises at the edge of the Brillouin zone due to the difference in field energy location between the first and second band. Both figures are reprinted from [20].

For simplicity, we consider a photonic crystals that is periodic in only one direction as shown in Fig. A.1. In this case, the solution of the master equation Eq. (1.1) is given by Bloch's theorem:

$$\boldsymbol{H}(\boldsymbol{x}) = e^{i\boldsymbol{k}\cdot\boldsymbol{x}}\boldsymbol{H}_{\mathrm{n},\boldsymbol{k}}(\boldsymbol{x}) \tag{A.1}$$

where $\boldsymbol{H}_{\mathrm{n},\boldsymbol{k}}(\boldsymbol{x})$ is periodic function in x. Therefore, the master's equation can be written as:

$$(\nabla + i\boldsymbol{k}) \times \frac{1}{\epsilon}(\nabla + i\boldsymbol{k}) \times \boldsymbol{H}_{\mathrm{n},\boldsymbol{k}}(\boldsymbol{x}) = \left(\frac{\omega_{\mathrm{n}}(\boldsymbol{k})}{c}\right)^2 \boldsymbol{H}_{\mathrm{n},\boldsymbol{k}}(\boldsymbol{x}) \tag{A.2}$$

where each value of $\boldsymbol{k}$ yields a different eigenvalue $\omega(\boldsymbol{k})$ over the primitive lattice vector $\boldsymbol{a}$. These eigenvalues $\omega_{\mathrm{n}}(\boldsymbol{k})$ form discrete bands, labelled n = 1,2,..., in band structure shown in Fig. 1.3.

One important fact is that the eigenvalue ω with the wavevector $\boldsymbol{k}$ and the eigenvalue ω with the wavevector $\boldsymbol{k} + m\boldsymbol{G}$ are identical, where $\boldsymbol{G}$ is the primitive reciprocal lattice vector defined by $\boldsymbol{R} \cdot \boldsymbol{G} = 2\pi$. Therefore, one needs only to compute the eigenvalues for $\boldsymbol{k}$ within the primitive reciprocal lattice vector which is conventionally known as the first Brillouin zone. This region spans from $-\pi/a$ to π/a in the reciprocal lattice since we consider only 1D photonic crystals. Moreover, the first Brillouin zone itself is redundant under further symmetries such as mirror planes. By omitting these redundant regions, one obtains the irreducible Brillouin zone. since most 1D photonic crystals systems will have time-reversal ($k \rightarrow -k$), the irreducible Brillouin zone spans from 0 to π/a.

Since photonic crystals, especially 2D and 3D are complex system, numerical computations are very essential in theoretical analyse. Here, we give a general theme how to write and run the script of Meep software to find the band structure for the nanobeam design mentioned in the chapter 2 and chapter 3. First, the computational cell is constructed such that the component in the periodic direction (x) has the same dimension as the unit cell a. Since the dielectric function and the field obey Bloch-periodic boundary conditions, the field would be redundant in the region out of the unit cell. Then, Gaussian pulses or any time-dependent source is placed in the dielectric area. The frequency can be any arbitrary user-specified in units of c/a. After that, the resolution is specified, e.g. to 16 pixels per one unit (16 pixels/a). After the source is turned off, we wait enough time, e.g. 300 in units of a/c, before finally analyze the response via Harminv software at a point in dielectric region.

Meep script for the band structure is shown in the following code:

```
(define-param n2 3.4) ; refractive index of waveguide
```

```
(define-param w 1) ; specified waveguide width
(define-param l 1) ; specified waveguide length
(define-param h 0.667) ; specified waveguide height
(define-param r 0.3); specified cylinder radius
(define-param dpml 1) ; perfectly matched layers
(define-param pad 0.5) ; padding between waveguide and PML
(define-param k 0.2) ;  specified point in k-space
(define sy (+ w (* 2 (+ pad  dpml)))) ; Y cell size
(define sz (+ h (* 2 (+ pad dpml)))) ; Z cell size
(set! geometry-lattice (make lattice (size l sy sz)))
(set! pml-layers (list (make pml (direction Y) (thickness dpml))
(make pml (direction Z) (thickness dpml))
                         )
)
(set! geometry (list
    (make block (center 0 0 0) (size l w h)
    (material (make dielectric (index n2)))
        )
        (make cylinder
    (center 0 0 0) (radius r) (height h)
        (material air)
        )
        (make cylinder
    (center -0.5 (/ w 2) 0) (radius r) (height h)
        (material air)
        )
        (make cylinder
```

```
   (center -0.5 (/ w -2) 0) (radius r) (height h)
   (material air)
        )
        (make cylinder
    (center 0.5 (/ w 2) 0) (radius r) (height h)
        (material air)
        )
        (make cylinder
        (center 0.5 (/ w -2) 0) (radius r) (height h)
        (material air)
    )
            )
)
(set-param! resolution 16); increase from default value of 10
(define-param fcen 0.23) ; pulse center frequency
(define-param df 0.08) ; pulse frequency width
(set! sources (list
(make source (src (make gaussian-src (frequency fcen) (fwidth df)))
(component Ey)
 (center 0.4 0 0)
)
             )
)
(set! symmetries (list (make mirror-sym (direction Y) (phase -1))))
;(set-param! k-point (vector3 k 0))
(use-output-directory)
(run-sources+ 300
```

```
        (at-beginning output-epsilon)
        (after-sources (harminv Hz (vector3 0.4) fcen df)))
(define-param k-interp 19)
(run-k-points 500 (interpolate k-interp (list
                        (vector3 0 0) (vector3 0.5 0)
                                             )
                   )
)
```

Computing band structure with Meep involves several subtleties. For instance, Harminv accuracy goes down for large frequency bandwidths, as the increased number of bands makes the signal-processing more complicated. Sometimes, spurious modes appear as isolated dots on the band structure plot due to small number of pixels per unit cell. Therefore, it is recommended to increase the resolution from the default value as shown in the script. Also, it is recommended to exploit mirror symmetries to reduce the amount of computation and storage required for the simulation. Though the structure has mirror symmetry planes through the x and y axes, the source breaks the mirror symmetry through the y axis. In the script, the mirror symmetry through the x axis is exploited. More technical issues can be found in the Meep website.

A.2 Cavities resonant modes

Frequencies exist within the photonic bandgap are not allowed to propagate inside photonic crystals. However, one can introduce some modes to the bandgap by creating a defect in the crystal. The defect can be formed by modifying the photonic crystals geometry. Since these modes are confined in the bandgap, they either decay in the uniform waveguide that lies on either side of the holes (characterized by $1/Q_w$) or decay in the surrounding air (characterized by $1/Q_r$). Now, we explain how to calculate quality factors of long lifetime resonant modes. First, the computational cell is constructed such that padding and perfectly matched layers are added at the end of all axes. After that, we specify the geometry of the nanobeam cavity as well as the attached waveguide using

loops and predefined functions such as "geometric-object-duplicates". Next, a Gaussian pulse or any time-dependent source is placed at the canter of the cavity. As before, we wait enough time after the source is turned off and then analyze the response via Harminv at the cavity center. The resulting quality factor is the the total quality factor Q_{tot} given by the Eq. 2.3.

In order to calculate the cavity transmission one can place the source in one end of the cell and compute the transmission (or the flux spectrum) at the other end. Since the cavity bounces the beam back and forth, one has to collect the spectrum until the field decays by at least 1/1000 at the flux plane. However, the time it takes to run this simulation is very long for high quality factor cavities, and sometimes it goes beyond the limit we have in the cluster computer. Another way to calculate the cavity transmission is to compute first Q_r by adding 10 holes in each side of the cavity where $Q_{\text{tot}} \sim Q_{\text{r}}$. Then, we extract Q_w using the Eq. 2.3 and substitute it in Eq. 2.4 to estimate the cavity transmission.

Cavity mode volume defined in Eq. 2.1 can also be calculated in Meep using the predefined function "meep-fields-modal-volume-in-box fields". The resulting volume is in unit of a^3 which is different from the conventional unit $(\lambda/n)^3$. To convert the mode volume to the conventional unit, multiply the default volume by $(\omega_{\text{norm}} \cdot n)^3$.

Meep script for the quality factor and mode volume calculation is shown in the following code:

```
(define-param n 3.4) ; specified waveguide refractive index
(define-param wf 1.8) ; specified final width
(define-param wi 1.5) ; specified initial width
(define-param len 32) ; length of waveguide
(define-param rf 0.3); radius of the holes
(define-param pad 3) ; padding between the waveguide and PML
(define-param rw 853.4) ; curvature of the waist
(define-param dpml 1) ; thickness of PML
(define-param nh 16); No. of holes
(define-param h 1); waveguide height
```

```
(define-param addtime 1000); running additional time
(define sx (* 2 (+ nh pad dpml))) ; X cell size
(define sy (+ wf (* 2 pad dpml))) ; Y cell size
(define sz (+ h (* 2 pad dpml))) ; Z cell size
(set! geometry-lattice (make lattice (size sx sy sz)))
(set! geometry
        (append
        (geometric-object-duplicates
        (vector3 1 0) 0 (+ (- nh (/ len 2)) pad dpml)
         (make block (center (+ (* len 0.5) 1) 0) (size 1 wf h)
         (material (make dielectric (index n)))
         )
         )
         (geometric-object-duplicates
         (vector3 -1 0) 0 (+ (- nh (/ len 2)) pad dpml)
         (make block (center (- (* len -0.5) 1) 0) (size 1 wf h)
         (material (make dielectric (index n)))
         )
         )
         )
)
(define (copy x x-max dx)
        (if (<= x x-max)
                (begin  (set! geometry (append geometry (list
             (make block        (center x 0 0)
(size 1 (+ wi (* +2 rw) (* -2 rw (sqrt (- 1 (expt (/ x rw) 2))))) h)
                (material (make dielectric (index n)))
```

```
            )
          )
                                  )
                  )
                                (copy (+ x dx) x-max dx)
      )
    )
)
(copy (* (/ len 2) -1) (* (/ len 2) 1) 1)
(define (addright x x-max dx)
          (if (<= x x-max)
              (begin  (set! geometry ( append geometry (list
                  (make cylinder (center (+ x 0) (/ wf 2))
                  (radius rf) (height h) (material air)
                  )
                  (make cylinder (center (+ x 0) (/ wf -2))
                  (radius rf) (height h) (material air)
                  )
                                                            )
                                        )
                      )
                          (addright (+ x dx) x-max dx)
                              )
                      )
)
(define-param addside? true)
(if addside?
```

```
        (begin
(addright (+ (/ len 2) 0) (* 1 nh) 1)
        )
)
(define (addlift x x-max dx)
            (if (<= x x-max)
                (begin (set! geometry ( append geometry (list
                        (make cylinder (center (- x 0) (/ wf 2))
                        (radius rf) (height h) (material air)
                        )
                        (make cylinder (center (- x 0) (/ wf -2))
                        (radius rf) (height h) (material air)
                        )
                                                        )
                                    )
                        )
                    (addlift (+ x dx) x-max dx)
                )
            )
)
(define-param addside? true)
(if addside?
        (begin
(addlift (* -1 nh) (* (/ len 2) -1) 1)
        )
)
(define (fill x x-max dx)
```

```
            (if (<= x x-max)
                (begin (set! geometry ( append geometry (list
                (make cylinder  (center x 0 0)
                                (radius rf)
                                (height h)
                                (material air)
                )
                                                        )
                                        )
                                )
                    (fill (+ x dx) x-max dx)
                )
            )
)
(define-param holes? true)
(if holes?
        (begin
(fill (+ (* -1 nh) 0.5) (- (* 1 nh) 0.5) 1)
        )
)
(define (side x x-max dx)
                (if (<= x x-max)
                (begin (set! geometry ( append geometry (list
                (make cylinder
                (center (+ x 0) (/ (+ wi (* +2 rw)
                (* -2 rw (sqrt (- 1 (expt (/ x rw) 2)))) 0) 2)  0)
                (radius rf)
```

```
                    (height h)
                    (material air)
                    )
                    (make cylinder
                    (center (+ x 0) (/ (+ wi (* +2 rw)
                    (* -2 rw (sqrt (- 1 (expt (/ x rw) 2)))) 0) -2)  0)
                    (radius rf)
                    (height h)
                    (material air)
                    )
                                                            )
                                        )
                              )
                          (side (+ x dx) x-max dx)
                    )
                    )
)
(define-param holeside? true)
(if holeside?
          (begin
(side 0 (* 1 (/ len 2)) 1)
          )
)
(define (side x x-max dx)
                    (if (<= x x-max)
                    (begin  (set! geometry ( append geometry (list
                    (make cylinder
```

```
(center (- x 0) (/ (+ wi (* +2 rw)
(* -2 rw (sqrt (- 1 (expt (/ x rw) 2)))) 0) 2)  0)
(radius rf)
(height h)
(material air)
)
(make cylinder
(center (- x 0) (/ (+ wi (* +2 rw)
(* -2 rw (sqrt (- 1 (expt (/ x rw) 2)))) 0) -2)  0)
(radius rf)
(height h)
(material air)
)
                                                 )
                                  )
                 )
    (side (+ x dx) x-max dx)
)
)
)
(define-param holeside? true)
(if holeside?
        (begin
(side (* -1 (/ len 2)) 0 1)
        )
)
(set! pml-layers (list (make pml (thickness dpml))))
```

```
(set-param! resolution 24); increase from default value of 10
(define-param fcen 0.226) ; pulse center frequency
(define-param df 0.004)  ; pulse width (in frequency)
(set! sources (list
                  (make source
          (src (make gaussian-src (frequency fcen) (fwidth df)))
          (component Ey)
                  (center 0 0 0)
                  )
                )
)
(set! symmetries
        (list   (make mirror-sym (direction Y) (phase -1))
                (make mirror-sym (direction X) (phase +1))
                (make mirror-sym (direction Z) (phase +1))
        )
)
(define (print-mode-volume) (print
"mode_volume: " (meep-time)
", " (electric-energy-in-box
     (meep-fields-total-volume fields))
", " (meep-fields-electric-energy-max-in-box fields
     (meep-fields-total-volume fields))
", " (meep-fields-modal-volume-in-box fields
     (meep-fields-total-volume fields))
"\n")
)
```

```
(use-output-directory)
(run-sources+ addtime
    (at-beginning output-epsilon)
    (after-sources (harminv Ey (vector3 0 0 0) fcen df))
    (after-sources+ (- addtime (/ .05 fcen)) print-mode-volume)
)
(run-until (/ 1 fcen) (at-every (/ 1 fcen 10) output-efield-y))
```

Calculating quality factors with Meep involves several subtleties. Sometimes, modes are not showing up at the end of the simulation. This happens mostly because of mismatching between the field component or the polarization of the source and the cavity resonance we are looking for. Since we are interested in TE modes localized in the bandgap, the source should have one of these components: H_z, E_y, and E_x. For a technical reason, we usually choose E_y for the Gaussian source. In addition, the structure has mirror symmetry planes through all axes, and therefore we can exploit the mirror symmetries while the ensuring the correct phase of even and odd symmetries. This helps not only to reduce the amount of the computation but also to decrease the error in quality factor calculations. Moreover, specifying the central frequency and the bandwidth is quite elusive. We often try different frequencies and bandwidths with close values and check the corresponding error and the modal value.

APPENDIX B

OPTIMIZATION OF ELECTRON BEAM LITHOGRAPHY

The fabrication procedure for both GaP devices and Si_3N_4 devices involves many challenges. In this section, we explain the most fundamental issues we have encountered specifically during the EBL process. First of all, one has to optimize the basic variables of EBL procedure. The most crucial variable is the electron beam dose, in essence, how many electrons per unit area of exposure. This value changes depending on the dimension of the pattern, the resist type, and the beam power. For example, the optimal dose for 950 PMMA A4 resist is around 300 μC/cm^2. For HSQ negative resist, the the optimal dose is not stable but mostly is found around 800 μC/cm^2.

The first obscured problem concerns the shape and smoothness of nanobeam tapering arcs. SEM images for different rotational angles are displayed in Figure B.1 (a) and (b). It is clear that straight and right angle have imperfectly rounded arcs, whereas the angled structures exhibit smooth and fine arcs. However, this problem only appears for curves and rounded structures. The shape of the circular holes is another challenge, especially for relatively big feature sizes. SEM image of a typical Si_3N_4 nanobeam cavity is displayed in Fig. B.1 (c). It can be seen that the holes size and shape is not uniform and disordered. In addition, the sidewalls roughness is too poor. In general, sidewalls roughness is a combination of the resist-edge roughness and etched surface roughness. We notice that such problems arise when the e-beam is exposed to big and small features simultaneously. To circumvent these issues, we divide big areas into separate zones by writing only around their boundaries, as shown in Fig. B.1 (d). The resulting large rectangles will be gone after the Si undercut. The key advantage of this method is that we keep the exposed areas approximately in the same size to avoid any consequences for combining big and small features at the same time.

While most of the EBL problems can be resolved by adjusting universal parameters and variables governing EBL procedure, some issues are linked not to the EBL system itself but to the layer

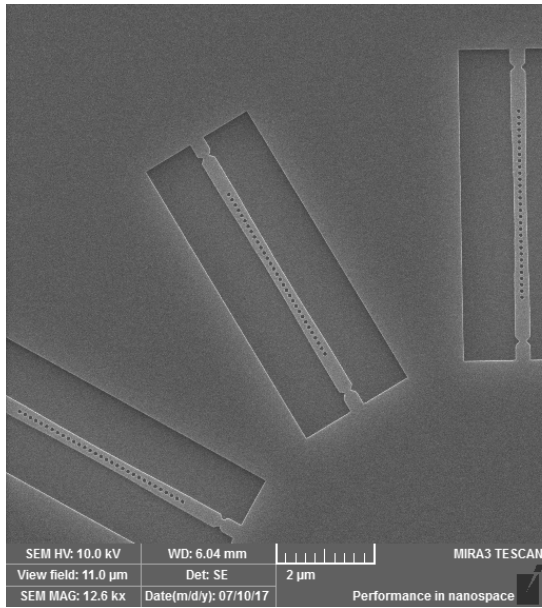

(a)

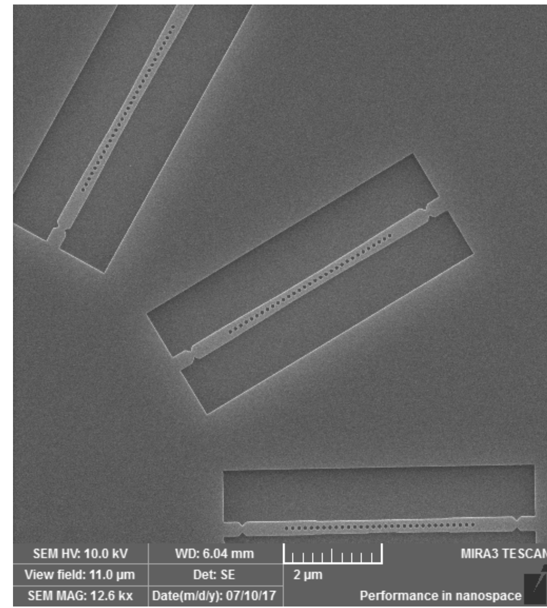

(b)

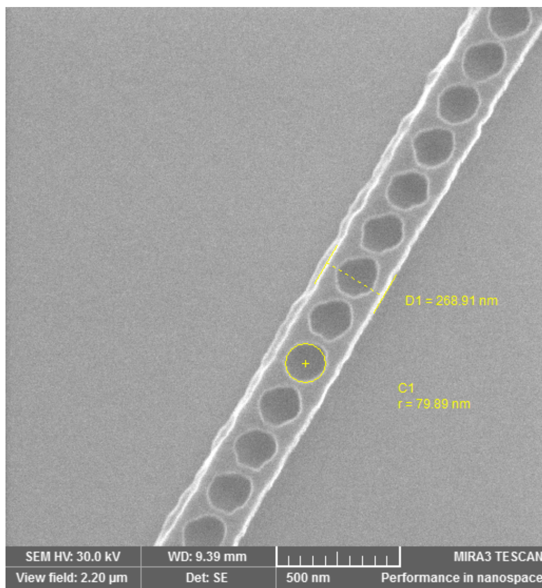

(c)

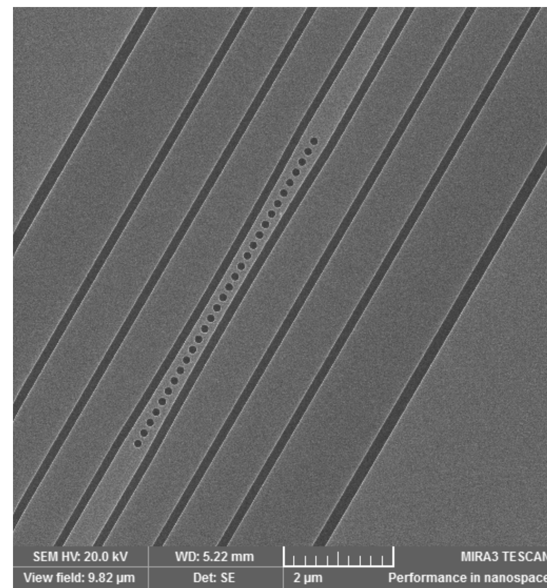

(d)

Figure B.1: SEM images of a nanobeam cavities fabricated via EBL process with various optimization parameters. (a) & (b) Structures fabricated on different rotational angles. These devices were initially fabricated with notches for free space-waveguide coupling instead of the waveguide taper. (c) Imperfect circular holes and rough sidewalls are observed as a result of combining big and small features. (d) Relatively big structures are marked around the device to keep the size of the exposed areas relatively close. These structures will be eradicated during the undercutting procedure.

in which the pattern is transferred. For instance, Si_3N_4 films has a relatively large bandgap (5 eV) making the e-beam focusing at the resist surface burdensome. Moreover, PMMA resist is known to have a bad selectivity in Si_3N_4 dry etch process, especially PECVD films according to Table 2.3 in Chapter 1. We deposit $\sim$ 20 nm of tungsten as a hard mask using DC sputtering tool which enables us to overcome these limitations. The pattern is transferred to the tungsten layer via RIE etching. The recipe is summarized in Table B.1. The selectivity of Si_3N_4 to tungsten during the dry etching is relatively high (5:1). After the etching process, the remaining tungsten is removed via a high temperature wet etching which uses Hydrogen peroxide (H_2O_2). Figure B.2 and shows SEM images of devices fabricated with tungsten hard mask and without it. The roughness of the lines is slightly enhanced with tungsten hard mask. However, the overall shape does not improve significantly.

SF_6 flow	20 sccm
RF power	200 W
DC bias	330 V
ICP power	0 W
Chamber pressure	10 mTorr
Temperature	20°C
Etch rate	0.85 nm/s
selectivity (Tungsten:PMMA)	1:5

Table B.1: Dry etching recipe of tungsten hard mask.

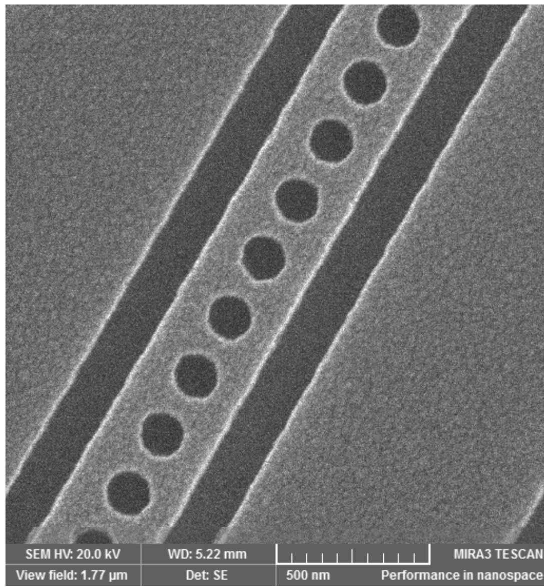

(a)

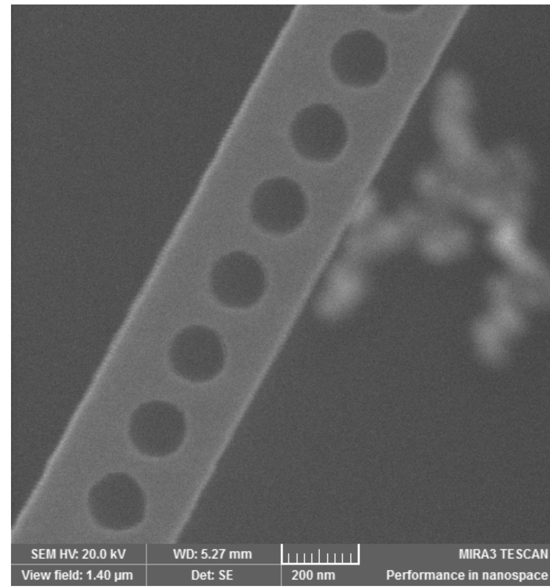

(b)

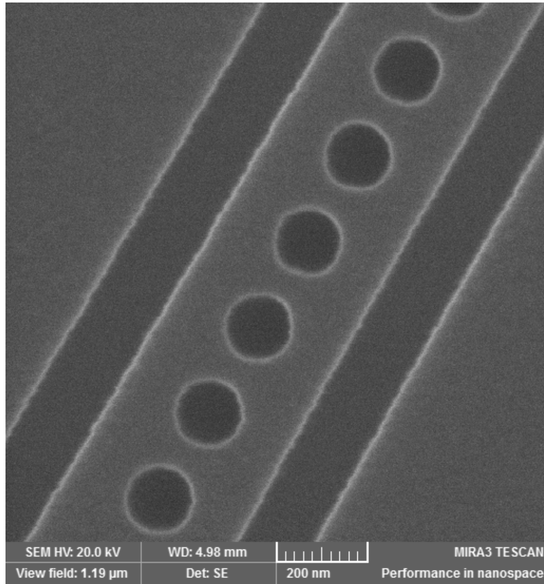

(c)

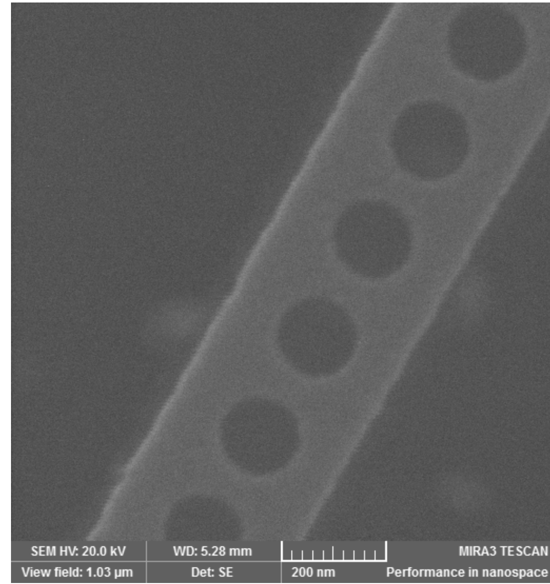

(d)

Figure B.2: (a) & (b) SEM images of a nanobeam cavity fabricated on tungsten hard mask before transferred to Si_3N_4 layer. (c) & (d) SEM images of a nanobeam cavity fabricated on Si_3N_4 layer without a tungsten hard mask. Left images are taken after the dry etching process, and right images are taken after the undercutting process.

APPENDIX C

REFLECTION OF THE FIBER RETROREFLECTOR

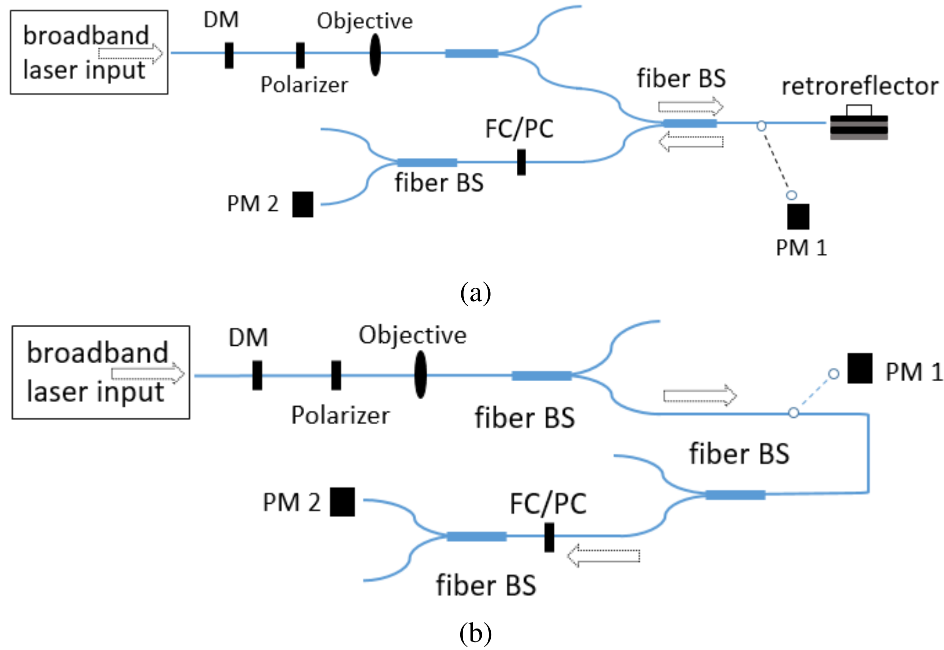

Figure C.1: (a) Schematic of the setup used to measure the reflection of the fiber retroreflector. (b) Schematic of the setup used to measure the power transmission between the point PM1 to the point PM2.

In chapter 4, we address the fiber-waveguide coupling efficiency which can be calculated by different schemes. The easiest scheme involves two photo diodes: one to calculated the power before the fiber and one after the fiber [91]. Then, the coupling efficiency would be simply the ratio of these two power values, after compensating for the power loss in the bath between the two points. Though this method seems to be straightforward, photo diodes are not always identical and this might lead to a huge error bar. The other alternative method is to use the fiber retroreflectors, which reflects all incident the beam, to calculate the normalization constant (ζ) in Eq. 4.5.

In principle, the average reflection from the fiber retroreflectors should be higher than 97.5% for the wavelength larger than 450 nm, based on the data sheet provided from Thorlabs. According to this estimate, the coupling efficiency we get is larger than 100%. This indicates that something is either missing or overestimated. To investigate this issue, we measure the actual reflection of the retroreflector using the scheme shown in Fig. C.1 (a). We send the light from the same source we used for calculating the coupling efficiency (SuperK EVo, NKT Photonics) and then measure the power that is coming in/out from the fiber retroreflector. Therefore, the reflection of the fiber retroreflector will be given by:

$$\beta = \frac{PM2}{\alpha PM1} \tag{C.1}$$

where α is the power transmitted through the optics locate between the two points where the power is measured, namely, PM1 and PM2. The measured transmission is $\alpha = 0.037\%$ using the scheme shown in Fig. C.1 (b) where the incoming beam is connected to the same point where the fiber retroreflector used to be connected. Finally, we found that the reflection of the retroreflector is only $\beta = 60\%$.